isoSTED microscopy for live cell imaging

Dissertation

zur Erlangung des mathematisch-naturwissenschaftlichen Doktorgrades

„Doctor rerum naturalium“

der Georg-August-Universität Göttingen

im Promotionsprogramm ProPhys

der Georg-August University School of Science (GAUSS)

vorgelegt von

René Siegmund

aus Eisenach

Göttingen, 2019

Betreuungsausschuss

apl. Prof. Dr. Alexander Egner
Optische Nanoskopie
Laser-Laboratorium Göttingen e.V.

Prof. Dr. Tim Salditt
Institut für Röntgenphysik
Georg-August-Universität Göttingen

Mitglieder der Prüfungskommission

Referent: **apl. Prof. Dr. Alexander Egner**
Korreferent: **Prof. Dr. Tim Salditt**

Weitere Mitglieder der Prüfungskommission

Prof. Dr. Sarah Köster
Institut für Röntgenphysik
Georg-August-Universität Göttingen

Prof. Dr. Stefan Jakobs
Struktur und Dynamik von Mitochondrien
Max-Planck-Institut für biophysikalische Chemie

Prof. Dr. Thorsten Hohage
Institut für Numerische und Angewandte Mathematik
Georg-August-Universität Göttingen

Dr. Florian Rehfeldt
III. Physikalisches Institut
Georg-August-Universität Göttingen

Tag der mündlichen Prüfung: 22.02.2019

Abstract

Far-field fluorescence microscopy is a versatile tool for the non-invasive investigation of intracellular structures and thus for live cell imaging. This is a major advantage over other microscopy methods such as electron microscopy or atomic force microscopy. Since the advent of super-resolution techniques such as stimulated emission depletion (STED) microscopy, protein structures within cells can be imaged with in principle unlimited resolution. In order to retrieve the maximum of available information by a measurement, it is beneficial if the microscope exhibits an isotropic resolution in all spatial dimensions. This can be achieved by applying the STED principle in a 4Pi microscope, which is termed isoSTED microscopy. Until now, only oil-immersion objective lenses were used for this technology, which limited isoSTED microscopy to the examination of fixed samples.

In this thesis, for the first time, we present an isoSTED microscope utilizing water-immersion objective lenses and demonstrate an isotropic resolution better than 56 nm. This resolution is measured on fluorescent beads and also confirmed on recordings of antibody labeled cells. In this context a problem of isoSTED microscopy utilizing water-immersion objective lenses becomes apparent. In extended sample regions signal from planes above and below the focal plane is also detected and deteriorates the image quality significantly. A method to specifically measure these out-of-focus signals is presented. This allows to correct the recorded data, which is demonstrated for live cell imaging.

Exemplary for the versatile usability of the here presented isoSTED microscope, the microtubule, vimentin and actin network in different cell lines is imaged with an isotropic resolution better than 60 nm. The actin network is measured in cells grown on a collagen-coated polyacrylamide gels. This mimics the elasticity of the extracellular matrix surrounding the cell in tissue and therefore demonstrates the feasibility of isoSTED microscopy under physiological conditions. Furthermore, isoSTED time lapse recordings reveal the reorganization of microtubule and actin networks.

Zusammenfassung

Weitfeld-Fluoreszenzmikroskopie ist ein wichtiges Werkzeug für die Erforschung lebender Zellen, da sie intrazelluläre Strukturen nicht-invasiv abbilden kann. Dies stellt einen großen Vorteil gegenüber anderen Mikroskopieverfahren wie Elektronen- oder Rasterkraftmikroskopie dar. Die Verwendung neuer, hochauflösender Mikroskopietechniken wie der STED-Mikroskopie (engl. Stimulated Emission Depletion, Fluoreszenzlöschung durch stimulierte Emission) erlaubt es, Strukturen in Zellen mit theoretisch unbegrenzter Auflösung zu untersuchen. Um ein Maximum an verfügbaren Informationen aus einer Messung zu erhalten, ist es von Vorteil, wenn das Mikroskop eine isotrope Auflösung in allen Raumrichtungen aufweist. Dies kann durch die Anwendung des STED-Prinzips in einem 4Pi-Mikroskop erreicht werden. Bisher wurde diese sogenannte isoSTED-Mikroskopie nur unter Verwendung von Ölimmersionsobjektiven durchgeführt, was die Anwendung auf die Untersuchung fixierter Proben beschränkte.

In dieser Arbeit präsentieren wir zum ersten Mal ein isoSTED-Mikroskop, welches mit Wasserimmersionsobjektiven arbeitet, und zeigen, dass hiermit eine isotrope Auflösung besser als 56 nm erzielt werden kann. Diese Auflösung wurde an fluoreszierenden Kügelchen bestimmt und anhand von Aufnahmen von mit Antikörperfärbung markierten Strukturen in Zellen verifiziert. Dabei zeigt sich ein Problem der isoSTED-Mikroskopie bei Verwendung von Wasserimmersionsobjektiven. In ausgedehnten Regionen der Probe wird zusätzliches Signal aus Ebenen oberhalb und unterhalb der Fokalebene detektiert, wodurch sich die Bildqualität signifikant verschlechtert. Wir zeigen eine Methode diese ungewollten Signalanteile separat zu detektieren, wodurch die gemessenen Daten korrigiert werden können. Dies erhöht die Bildqualität signifikant, was anhand von Aufnahmen von Strukturen innerhalb lebender Zellen demonstriert wird.

Exemplarisch für die vielseitige Einsetzbarkeit des hier vorgestellten isoSTED-Mikroskops werden Messungen des Mikrotubuli-, Vimentin- und Aktinnetzwerks in verschiedenen Zelllinien mit einer isotropen Auflösung besser als 60 nm gezeigt. Dass die isoSTED-Mikroskopie prinzipiell geeignet ist physiologische Proben zu untersuchen, wird durch Aufnahmen des Aktinnetzwerks von Zellen, die auf kollagenbeschichteten Polyacrylamidgelen gezüchtet wurden, demonstriert. Hierbei wird durch das Gel die Elastizität der extrazellulären Matrix, welche Zellen üblicherweise im Gewebe umgibt, nachgebildet. Darüber hinaus zeigen wiederholte isoSTED-Aufnahmen über einen längeren Zeitraum, wie sich das Mikrotubuli- und Aktinnetzwerk innerhalb von lebenden Zellen umstrukturiert.

Abbreviations

3D	three-dimensional
AOM	acousto-optic modulator
CO_2	carbon dioxide
EMCCD	electron multiplying charge-coupled device
FCS	fluorescence correlation spectroscopy
FHWM	full width at half maximum
HDFn	neonatal human dermal fibroblast
hMSC	human mesenchymal stem cell
HWP	half-wave-plate
IC	internal conversion
isoSTED	isotropic STED
NA	numerical aperture
NIR	near-infrared
OOFC	out-of-focus contributions
OPD	optical path legth difference
PAA	polyacrylamide
PBS	phosphate buffered saline
PMT	photo-multiplier tube
pol-BS	polarizing beam splitter
PSF	point spread function
RESOFLT	reversible saturable optical fluorescence transition
RL	Richardson-Lucy
ROI	region of interest
SiR	silicon rhodamine
STED	stimulated emission depletion
TDE	2'2-Thiodiethanol

Contents

List of Figures

1. Introduction

Microscopes have been used to discover several fundamental principles in biology. In 1625 Francesco Stelluti published drawings of bees that showed features that were not observable by the human eye before [1]. Those drawings are considered to be the oldest drawings made with the help of a microscope. In the book Micrographia, published in 1660, Robert Hooke [2] described the structure of fly eyes and coined the term cell, because the walled plant cells in cork reminded him of the cells in a honeycomb. Since then, improvements in optics, microscopes and microscopy techniques have enabled light microscopy to become a versatile tool e.g. in the life sciences, as it allows to non-invasively investigate the interior of translucent specimens. Moreover, far-field fluorescence microscopy offers the possibility to specifically detect otherwise transparent structures within the sample, e.g. proteins within the cell, that are tagged with fluorescent markers.

However, for a long time, the resolution of a microscope was considered to be limited by diffraction. Due to the wave nature of light any point-like object imaged by a microscope is not imaged to a point, but to an extended intensity distribution. This blurring of a point-like object is described by the point spread function (**PSF**) of the microscope. In 1873 Ernst Abbe discovered that the resolution of a microscope depends only on the wavelength of the light and the numerical aperture of the objective lens used [3]. Abbe's considerations, however, did not allow any conclusions on light emitting objects or the axial resolution. According to the Rayleigh criterion, the images of two point emitters can still be discerned when the maximum of the diffraction pattern of one point emitter coincides with the minimum of the diffraction pattern of the other [4]. This distance can also be used to define the resolution of the microscope and can also be calculated for the axial direction. For a microscope utilizing objective lenses with a high numerical aperture, the lateral and the axial resolution are accordingly limited to approximately half the wavelength and twice the wavelength of the light used.

For the reasons set out above, the resolution of the light microscope cannot be increased arbitrarily: First, the semi aperture angle of the objective lens is limited due to technical reasons to about 79°. Second, the refractive index cannot be increased at will as refractive index differences between the immersion medium and the sample introduce spherical aberrations [5, 6], and third, decreasing the wavelength of the

light used down to the ultraviolet range is not compatible with live cell imaging as biological samples show autofluoresence when exposed to light in this regime.

A fundamental breakthrough in the achievable resolution of light microscopes was realized when fluorescent markers were not only considered as contrast agents, but the molecular transitions of the markers were additionally used to specifically switch on and off the ability to fluoresce of a subset of markers. The first method to use this concept was stimulated emission depletion (**STED**) microscopy. It was proposed by Hell and Wichmann in 1994 [7] and demonstrated by Klar and Hell in 1999 [8]. In STED microscopy, excited fluorescent markers in their fluorescent singlet state (bright state) are driven into the non-fluorescent ground state (dark state) by stimulated emission. A helical phase pattern is imprinted onto the depletion beam such that a doughnut-shaped de-excitation pattern featuring a zero-intensity in its center is formed in the focus of the objective lens. By overlapping the excitation and the STED beam, excited fluorophores are transferred back into their dark state wherever the STED intensity is sufficiently high and therefore, the region from which fluorescence can still be emitted after depletion is reduced. Theoretically, the resolution achievable with a STED microscope is unlimited [7]. The generalized principle behind STED microscopy can be applied to any type of molecule that can be reversibly switched between two distinguishable states A and B and is termed reversible saturable optical fluorescence transition (**RESOLFT**) [9, 10].

The doughnut-shaped de-excitation pattern in standard STED microscopy increases the resolution only in the lateral direction. In order to also increase the axial resolution, high intensities of the de-excitation light must also be generated above and below the focal plane. This can be done by imprinting a phase shift of π to the central region of a Gaussian STED beam [11, 12]. However, due to the discrepancy between the lateral and axial extent of the focus generated by an objective lens, the axial resolution in 3D-STED microscopy is still worse than the lateral resolution by a factor of 3 - 5 when identical STED intensities are used for the axial and lateral STED beams. This discrepancy can be circumvented when two opposing objective lenses are used to e.g. coherently illuminate the sample. This principle is called 4Pi microscopy and is able to decrease the axial extent of the common focus of both objective lenses [13, 14]. By applying the STED concept in a 4Pi microscope an isotropic depletion intensity around the geometric focus of both objective lenses can be generated and thus the volume from which fluorescence can still be emitted after depletion can be reduced to an isotropic sphere. This technique is called isoSTED microscopy and has for example been used to investigate mitochondrial proteins in fixed cells [15, 16] or the nanoscale morphology in block copolymers [17, 18]. To our knowledge it has to date not been used for imaging within living cells. What has been shown so far is 4Pi-RESOLFT nanoscopy [19] with an isotropic resolution

better than 40 nm in living cells. However, due to the switching characteristics of the fluorescent proteins used and the thus required activation and deactivation scheme, the voxel dwell time is here in the range of some hundred microseconds to a few milliseconds resulting in quite long base acquisition time of 7 - 21 s μm^{-3} [19]. Contrary, in STED microscopy the fluorescence depletion occurs within the life time of the fluorophore (a few nanoseconds) and thus the voxel dwell time is limited only by the need to collect a sufficient number of fluorescence photons in order to distinguish the signal from the background. Therefore, isoSTED microscopy in living cells offers the possibility to achieve a comparable resolution within a fundamentally shorter recording time.

In this thesis, an isoSTED microscope is built up, characterized and adapted to the conditions needed for imaging within living cells. In particular, water-immersion objective lenses are utilized for the first time for isoSTED imaging in order to minimize the refractive index difference between the immersion medium and the sample. The influence of the water-immersion objective lenses on the performance of the microscope is discussed and a method that improves the image quality by removing signal contributions from above and below the focal plane, which substantially affect the image quality negatively, is presented. Thereafter, this correction method is applied to live cell imaging. Exemplary for the versatility of the isoSTED microscope utilizing water-immersion objective lenses three proteins within three different cell types are labelled and analyzed: First, the microtubule network in human fibroblasts, second, the vimentin network in U-2 OS cells and third, the actin network in human mesenchymal stem cells. The latter are measured on aqueous gels that mimic a physiological environment for the cells. Additionally, isoSTED time lapse imaging on the microtubule and actin network is presented.

2. Theory

2.1. Image formation

When light emitted by a point-like light source is imaged with a lens, its resulting image is not a point, but a blurred three-dimensional (**3D**) intensity distribution around the geometrical focal point $\vec{r}(x = 0, y = 0, z = 0)$. This blurring is due to the wave nature of the light and is a consequence of the focusing of light that is diffracted at the circular aperture of the lens [3]. The electric field distribution at $\vec{r} = (x, y, z)$ is called the amplitude point spread function and can by calculated by 3D scalar diffraction theory as [20]:

$$h_A(\vec{r}) = A \int_0^\alpha \sqrt{\cos(\theta)} \sin(\theta)\ J_0\left(k\sqrt{x^2+y^2}\sin(\theta)\right) \exp\left(ikz\cos(\theta)\right)\ \mathrm{d}\theta, \quad (2.1)$$

with A being a normalization constant, J_0 the zero order Bessel function of the first kind and θ the polar aperture angle that ranges from 0 to the maximum opening angle α. The wave number $k = 2\pi n/\lambda_0$ depends on the refractive index n and the vacuum wavelength λ_0.
As detectors usually measure intensity and not the electric field, the intensity distribution or intensity point spread function PSF (**PSF**) has to be used for describing the imaging process. It is given by the square of the absolute value of the amplitude point spread function

$$h(\vec{r}) = \left|h_A(\vec{r})\right|^2. \quad (2.2)$$

In general the PSF of an imaging system describes the image of a point emitter. For such an emitter and a lens with a circular aperture the PSF is given by an Airy pattern and its bright central region in the focal plane is known as the Airy disk. According to the Rayleigh criterion, two point sources can still be discerned when the maximum of the diffraction pattern of one point emitter coincides with the minimum of the diffraction pattern of the other [4, 20]. Note that this only holds true for two point sources that radiate incoherently. The radius of the Airy disk can

therefore be used as a measure of the lateral ($x, y; r = \sqrt{x^2 + y^2}$) resolution

$$\Delta r = 0.61 \, \frac{\lambda_0}{\mathrm{NA}}, \tag{2.3}$$

with $\mathrm{NA} = n \cdot \sin(\alpha)$ being the numerical aperture (**NA**) and α denoting the semi-aperture angle of the lens. Analogous the resolution in the axial direction can be defined as the distance between the maximum and the first minimum in the axial (z) direction of the diffraction pattern

$$\Delta z = 2.00 \, \frac{n \, \lambda_0}{\mathrm{NA}^2}. \tag{2.4}$$

Often the central region of the Airy pattern is approximated by a Gaussian. Then the resolution can be described by its full width at half maximum (**FWHM**) as:

$$\begin{aligned} \Delta \tilde{r} &= 0.51 \, \frac{\lambda_0}{\mathrm{NA}} \text{ and} \\ \Delta \tilde{z} &= 1.77 \, \frac{n \, \lambda_0}{\mathrm{NA}^2}. \end{aligned} \tag{2.5}$$

If the PSF is space invariant, the image $I(\vec{r})$ of an object $O(\vec{r})$ is given by the convolution of the object with the PSF $h(\vec{r})$ [21]:

$$I(\vec{r}) = O(\vec{r}) * h(\vec{r}). \tag{2.6}$$

Therefore, during the imaging process, the object is blurred by the PSF of the microscope. In order to get a sharp image, the PSF must be as small as possible, thus the use of objective lenses with a high numerical aperture is essential. In the following the PSFs of two microscopes which are of major importance for this work are discussed in more detail.

Confocal microscope

In confocal microscopy a point source is imaged onto the sample plane [22]. As the spot size is limited by diffraction, a spatial intensity distribution emerges around the geometrical focal point and serves as illumination PSF $h_{ill}(\vec{r})$. Fluorescent markers within the focal spot can be excited and can therefore emit fluorescence. This fluorescence is collected by the same lens and imaged onto a single pixel detector (e.g. an avalanche photodiode). Placing a pinhole in the image plane at the position of the geometrical focal point ensures that only fluorescence from its direct vicinity is detected. As the light path is invertible this can be interpreted as imaging the pinhole into the focal plane. This image of the pinhole is called the detection PSF,

$h_{det}(\vec{r})$, and describes the probability to detect a photon emitted at position $\vec{r}$. The PSF of the confocal microscope is then given by:

$$h_{conf}(\vec{r}) = h_{ill}(\vec{r}) \cdot h_{det}(\vec{r}). \tag{2.7}$$

In the theoretical limit of an infinitesimally small detection pinhole and identical wavelengths for illumination λ_{ill} and detection λ_{det} a confocal microscope improves the resolution by a factor of $\sqrt{2}$ [23]. However, a finite pinhole is necessary to collect sufficient signal. If the pinhole is described by the pinhole function

$$p(\vec{r}) = p(x, y, z = 0) = \begin{cases} 1 & \text{for} \sqrt{x^2 + y^2} \leq p_0 \\ 0 & \text{otherwise} \end{cases}, \tag{2.8}$$

with p_0 being the radius of the pinhole, the real detection PSF $h_{det,real}(\vec{r})$ is defined as

$$h_{det,real}(\vec{r}) = h_{det}(\vec{r}) * p(\vec{r}), \tag{2.9}$$

and the real confocal PSF is given by the product of the illumination PSF and the real detection PSF

$$h_{conf,real}(\vec{r}) = h_{ill}(\vec{r}) \cdot h_{det,real}(\vec{r}). \tag{2.10}$$

In order to record an extended sample volume, the confocal PSF is scanned through the sample.

4Pi microscope

The resolution in light microscopy is limited by the numerical aperture (NA $= n \cdot \sin(\alpha)$) of the objective lenses (see eq. 2.3, 2.4 & 2.5). In order to increase the resolution, either the semi-aperture angle of the objective lenses α or the refractive index n has to be increased. The semi-aperture angle is limited to about 79° (*UAPON 100XO TIRF, Olympus, Japan*) due to mechanical restrictions. Increasing the refractive index will also increase the refractive index difference between the immersion medium and the embedding medium, which will introduce spherical aberrations at the interfaces [6, 24]. In 4Pi microscopy [13, 14] two opposing lenses are arranged such that their focal spots overlap at a common focal spot. By ensuring coherent illumination and/or detection from both sides, they can act as a single objective that in the theoretical limit is able to cover a solid angle which is close to 4π.

Depending on the illumination and detection scheme, three types of the 4Pi microscope are distinguished [14]. In a type A configuration the objectives lenses are used coherently for illumination and incoherently for detection. It is called type B when

the objectives lenses are used coherently for detection and incoherently for illumination and type C when they are used coherently for illumination and detection.

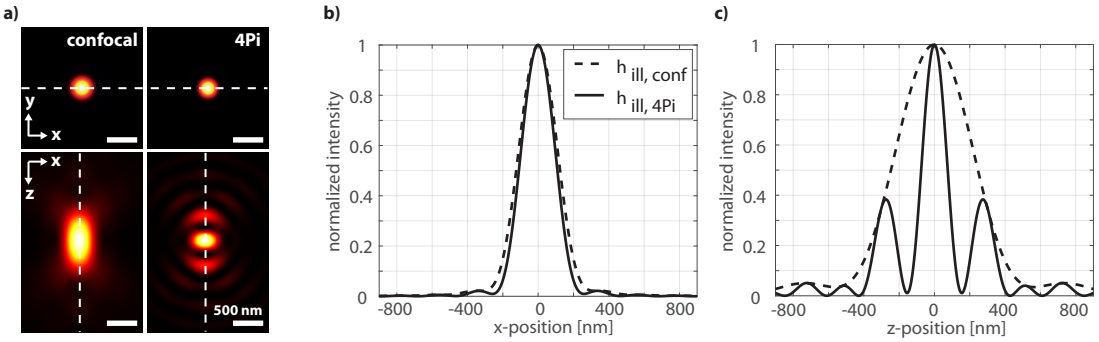

Figure 2.1.: Comparison of the illumination PSF for a confocal and a 4Pi microscope of type A: **(a)** The central x-y-section and x-z-section through the confocal and 4Pi illumination PSF and the intensity along the x-axis **(b)** and z-axis **(c)**, indicated by the dashed white lines, are shown. Parameters: $\lambda_{ill} = 640$ nm, NA = 1.49, n = 1.515. The scale bar represents 500 nm.

In a 4Pi microscope of type A the illumination PSF is given by:

$$h_{ill}^{\mathrm{4Pi}}\left(\vec{r}\right) = \left|\vec{E}_{ill,1}\left(\vec{r}\right) + \vec{E}_{ill,2}\left(\vec{r}\right)\right|^2, \tag{2.11}$$

with $\vec{E}_{ill,1}\left(\vec{r}\right)$ and $\vec{E}_{ill,2}\left(\vec{r}\right)$ being the electrical light field distributions generated by the respective objectives. As confocal detection is used, the 4Pi PSF is given by the multiplication of the illumination PSF with the detection PSF

$$h_{\mathrm{4Pi}}\left(\vec{r}\right) = h_{ill}^{\mathrm{4Pi}} \cdot h_{det,real}\left(\vec{r}\right). \tag{2.12}$$

The central x-y-section $(x, y, z = 0)$ and x-z-section $(x, y = 0, z)$ through the illumination PSFs of a confocal and a 4Pi microscope are shown in figure 2.1**a**. They are calculated for oil-immersion objective lenses (NA = 1.49, $n = 1.518$) and the illumination wavelength, $\lambda_{ill} = 640$ nm. The intensities along the dashed lines plotted against the position on the lines are shown for the lateral and axial direction in 2.1**b** **&** **c**. The intensity modulation along the optical axis (z) of the 4Pi illumination features a main lobe and primary side lobes. The FWHM of the main lobe is smaller than the FWHM of the confocal illumination (dashed curve) and therefore the axial resolution in 4Pi microscopy is improved. While imaging h_{4Pi} is scanned through a 3D sample and ghost images, generated by the side lobes will appear in the recorded data sets. They can be removed using linear three-point deconvolution [25] or non-linear Richardson-Lucy deconvolution [26, 27].

2.2. Super-resolution microscopy

Fluorescence

Fluorescence microscopy techniques utilize fluorescent molecules to label structures of interest within an otherwise transparent sample. Figure 2.2**a** illustrates the energy levels and possible excitation and de-excitation pathways of a fluorescecent molecule in a Jablonski diagram.

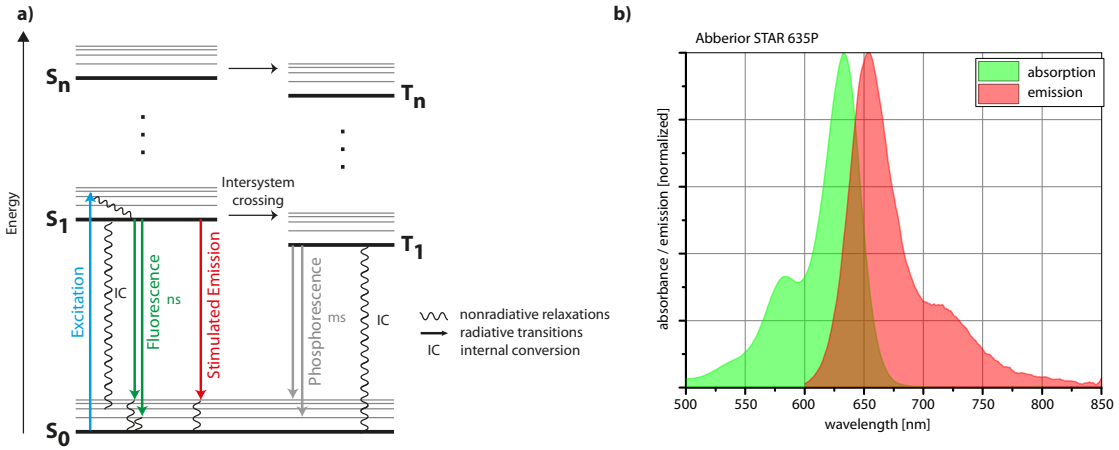

Figure 2.2.: (a) Jablonski diagram of a fluorescent molecule. Thick lines indicate the lowest vibrational energy level of the singlet states S_0, S_1 and S_n and the triplet states T_1 and T_n. Thin lines indicate higher vibrational energy levels. By absorption of a photon the molecule can be excited from the ground state, S_0, into any vibrational level of S_1. Fast nonradiative relaxation into the lowest level of S_1 takes place within picoseconds. The transition into the ground state can be due to nonradiative internal conversion (IC), emission of a photon either spontaneously (fluorescence) or driven by an external light field (stimulated emission), or intersystem crossing to T_1 followed by IC or emission of phosphorescence. Already excited molecules can reach higher-excited states, S_n and T_n with $n > 1$, by absorbing one or multiple photons. **(b)** Absorption and emission spectrum of Abberior STAR 635P (Abberior).

The five shown states are the ground singlet state, S_0, the first-excited singlet state, S_1, the lowest-excited triplet state, T_1, and higher-excited singlet and triplet states, S_n and T_n with $n > 1$, respectively [28]. The thick lines in each state indicate the lowest vibrational energy level, whereas the thin lines indicate levels with higher vibrational energy of this electronic state. Typically, at ambient temperatures the majority of molecules is in the lowest vibrational energy level of S_0. An excitation photon with a sufficient energy can be absorbed by the molecule and therefore excite it into any vibrational level of S_1. Thus, a fluorescent molecule can be excited by light from a rather broad spectral range.

Within some picoseconds after the excitation the molecule relaxes nonradiatively into the lowest vibrational level of S_1. From there it can transit into any vibrational level of S_0 by nonradiative internal conversion (**IC**) or by emission of a photon. The

latter can be due to spontaneous emission within the fluorescence lifetime (lifetime of S_1; $\tau_{fl} \approx 1 - 10$ ns) or can be driven by an external light field which is called stimulated emission. The wavelength of the emitted fluorescence is longer than the excitation wavelength due to the energy loss during the vibrational relaxation. The absorption and fluorescence spectrum of Abberior STAR 635P (*Abberior, Göttingen, Germany*), a common fluorophore, is presented in figure 2.2**b**.
Another possible transition is the intersystem crossing from S_1 to T_1. This transition is associated with a spin flip of the excited molecule due to a non-negligible spin-orbit coupling [28]. After relaxation to the lowest vibrational level of T_1, non-radiative IC and radiative phosphorescence into S_0 are possible. In the following, a non-fluorescent state is referred to as the dark state (or off-state), while a fluorescent state (here S_1) is called the bright state (or on-state).
Typically the photon energy of the excitation and stimulated emission light is not sufficient to directly excite a molecule from the ground state, S_0, into the higher-excited states S_n and T_n. But an already excited molecule can absorb one or multiple photons and transit into higher excitated states. These states S_n and T_n are associated with photobleaching in STED microscopy [29].

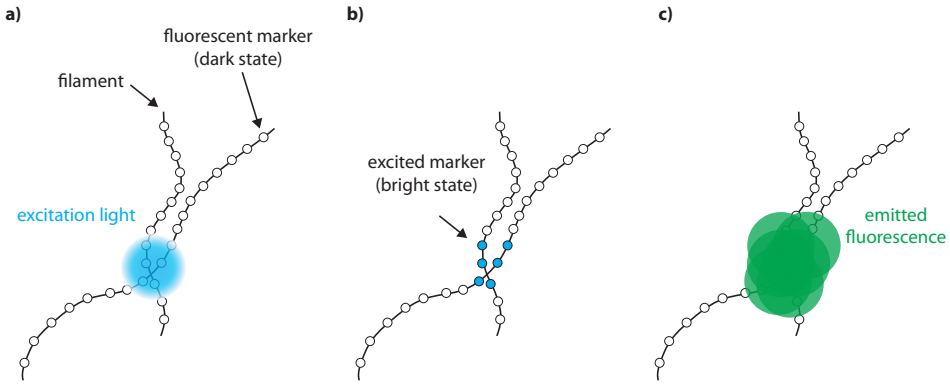

Figure 2.3.: **(a)** Illumination of fluorescently labeled filaments with a diffraction-limited spot. **(b)** Markers within the excitation spot can be excited and therefore emit fluorescence **(c)**, which is blurred by the detection PSF and structures within the excitation spot can not be resolved.

Figure 2.3 illustrates the excitation and emission processes in a fluorescently labeled sample imaged with a confocal microscope. For simplicity only one scan position is shown. A filamental structure, labeled with fluorescent markers is illuminated by a diffraction-limited spot (see fig. 2.3**a**). Fluorescent markers within this spot are possibly excited (see fig. 2.3**b**) and could therefore emit fluorescence. The emitted fluorescence from each marker is blurred by the detection PSF (see fig. 2.3**c**). Therefore, it is not possible to distinguish between signals from markers which are too close to each other and thus, fine structures can not be resolved.
During the last decades, new super-resolution fluorescence microscopy techniques

emerged. Even though the laws of diffraction are still valid, they can be circumvented by switching the ability of the fluorophore to fluoresce on and off. They can be separated into stochastic readout and targeted readout techniques.
Stochastic readout methods ensure that only fluorophores that are further apart than the diffraction limit are in the bright state at the same time. Then, in the recorded image all individual emitters can be identified, localized and mapped into a position histogram. Since only a few fluophores emit in one image, many individual images in which different subsets of fluorophores are in their bright state must be acquired, analyzed. When sufficient localizations are mapped into the position histogram, a super-resolved imaged can be obtained. Depending on e.g. the switching scheme and the fluorophores used these techniques are e.g. called STORM [30], dSTORM [31], PALM [32], fPALM [33], PALMIRA [34] or GSDIM [35].

In contrast to the stochastic readout mode, which is based on determining the unknown position of an emitter in the sample, in the targeted readout mode optical methods are used to actively define the area in the sample where the fluorophores are in their on- or off-states [36]. This can be achieved by overlapping the excitation spot with a spatial intensity distributions, $I(\vec{r}, t)$, featuring at least one zero-intensity region (e.g. a doughnut-shaped intensity distribution). Switching is only possible when $I(\vec{r}, t) > 0$ and absent at $I(\vec{r}, t) = 0$. In ground state depletion (GSD) microscopy [37] this is achieved by transitioning fluorophores into the non-fluorescent triplet state. Stimulated emission depletion (**STED**) microscopy [7] utilizes the process of stimulated emission to force excited molecules back to the ground state, S_0, without emitting a fluorescence photon.
In the following the STED principle is explained in more detail.

2.3. STED microscope

Stimulated emission as a tool to increase the resolution in light microscopy was proposed by Hell and Wichmann in 1994 [7] and demonstrated by Klar and Hell in 1999 [8].
Typically a doughnut-shaped intensity distribution $I_{STED}(\vec{r})$, featuring a central zero ($I_{STED}(\vec{r} = 0) = 0$), is superimposed with the excitation PSF and used for the de-excitation of excited fluorescent molecules. The wavelength of the STED beam is shifted to the red end of the fluorescence spectrum, e.g. $\lambda_{em}^{max} = 654$ nm and $\lambda_{STED} = 775$ nm for Abberior STAR 635P (see fig. 2.2**b**). Therefore, the STED photon have an almost negligible probability to re-excite the fluorescent molecules. The molecules de-excited by the STED beam are transitioned into higher vibrational

levels of S_0 and relax to the lowest vibrational level within a few picoseconds (see fig. 2.2**a**).
The rate of the transition by stimulated emission is given by:

$$k_{STED}\left(\vec{r}\right) = \sigma \cdot I_{STED}\left(\vec{r}\right), \tag{2.13}$$

with σ being the cross-section for stimulated emission. Typical values are $\sigma \approx 10^{-16} - 10^{-17}\text{cm}^2$. In order to switch the molecules off effectively, the rate for stimulated emission must exceed the rate for spontaneous emission $k_{STED} \gg k_{fl} = 1/\tau_{fl}$. Therefore, the required STED intensity must be much larger than the saturation intensity I_{sat} of the fluorophore

$$I_{STED}\left(\vec{r}\right) \gg 1/\left(\sigma\tau_{fl}\right) \equiv I_{sat}. \tag{2.14}$$

I_{sat} is defined as the STED intensity where the intial fluorescence has dropped to 1/2 [12]. It is usually in the range of 10^6 W/cm^2.
Pulsed lasers are usually used for STED microscopy as they allow to work with moderate average powers. The suppression factor $\eta\left(\vec{r}\right)$ is defined as the fraction of fluorescence still detected at position $\vec{r}$ in the presence of the inhibition light [12]. It can be well approximated by an exponential [12, 38]:

$$\eta\left(\vec{r}\right) = \exp\left(-\ln 2 \cdot h_{STED}\left(\vec{r}\right)/I_{sat}\right), \tag{2.15}$$

with $h_{STED}\left(\vec{r}\right) = I_{STED}\left(\vec{r}\right)$, the STED PSF.
The effective PSF of the STED microscope, $h_{eff}^{STED}\left(\vec{r}\right)$, defines the region in the focus, from which fluorescence can still be emitted after the depletion with the STED beam and is given by the multiplication of the confocal illumination PSF with the suppression factor:

$$h_{eff}^{STED}\left(\vec{r}\right) = h_{ill}^{conf}\left(\vec{r}\right) \cdot \eta\left(\vec{r}\right). \tag{2.16}$$

In the vicinity of the focal spot, the confocal illumination PSF can be described by a Gaussian [12] and the intensity distribution of the depletion pattern close to the focal point can be approximated by paraboloid [12]

$$h_{STED}(\vec{r}) \propto I_{STED}^{max}\vec{r}^2, \tag{2.17}$$

with I_{STED}^{max} being the maximum STED intensity within the depletion pattern. Due to the exponential behavior in equation 2.15, h_{eff}^{STED} can be described by a Gaussian with a reduced width [12]. The lateral resolution of the STED microscope is then

given as its FHWM [23, 39]

$$\Delta r_{STED} = \frac{\lambda}{2n \sin\alpha \sqrt{1 + I_{STED}^{max}/I_{sat}}} = \frac{\lambda}{2n \sin\alpha \sqrt{1+\zeta}}, \tag{2.18}$$

with $\zeta = I_{STED}^{max}/I_{sat}$, being the saturation factor [39, 40]. Theoretically the resolution can be increased down to the molecular level by increasing I_{STED}^{max} [7]. Resolutions of 5.8 nm [41] and 2.4 nm [42] have already been demonstrated on single nitrogen vancancies centres in diamonds. Contrary to the nitrogen vacancies, fluorescent molecules do bleach which limits the number of times a fluorescent molecule can be excited and subsequently de-excited. This limits the achievable resolution. Still a lateral resolution of $\Delta x = 15$ nm was demonstrated by imaging single fluorescent molecules [39].

The doughnut-shaped depletion pattern allows to only confine the effectively excited volume in the lateral direction as its intensity along the optical axis is zero. In order to achieve a resolution increase in axial direction, a depletion pattern with an intensity distribution above and below the focal plane must be applied. For example a circular phase plate can be used to imprint a phase shift of π to the central regions of a Gaussian STED beam and thus create such a STED intensity distribution [11, 12].

Another approach is to use the advantage of the already reduced axial extent of a 4Pi illumination PSF, $h_{ill}^{4\mathrm{Pi}}(\vec{r})$, (cf section 2.1) in combination with a depletion pattern formed by the interference of two counter-propagating Gaussian STED beams which exhibit a relative phase shift of π. The generated depletion pattern features a zero-intensity region at $(x, y, z = 0)$ with an FWHM of $\sim \lambda/(4n)$ [43]. This method is called STED-4Pi fluorescence microscopy [38, 43, 44].

The combination of the STED-4Pi microscope and a second doughnut shaped-depletion beam is able to generate an isotropic effective illumination PSF. With this so called isotropic STED (**isoSTED**) microscope an isotropic resolution of 30 nm has been demonstrated [15, 16].

2.4. IsoSTED microscope

Unlike in standard 4Pi microscopy [13, 14, 45], in isoSTED microscopy linearly polarized light is used to generate the excitation and depletion patterns [15]. Two depletion patters are used, one for lateral confinement (STEDxy) and one for axial confinement (STEDz). The interference patterns in the common focus of the objective lenses are presented in figure 2.4. They are simulated for oil-immersion objective lenses (NA = 1.49, $n = 1.515$) and $\lambda_{exc} = \lambda_{ill} = 640$ nm and $\lambda_{STED} = 775$ nm, for

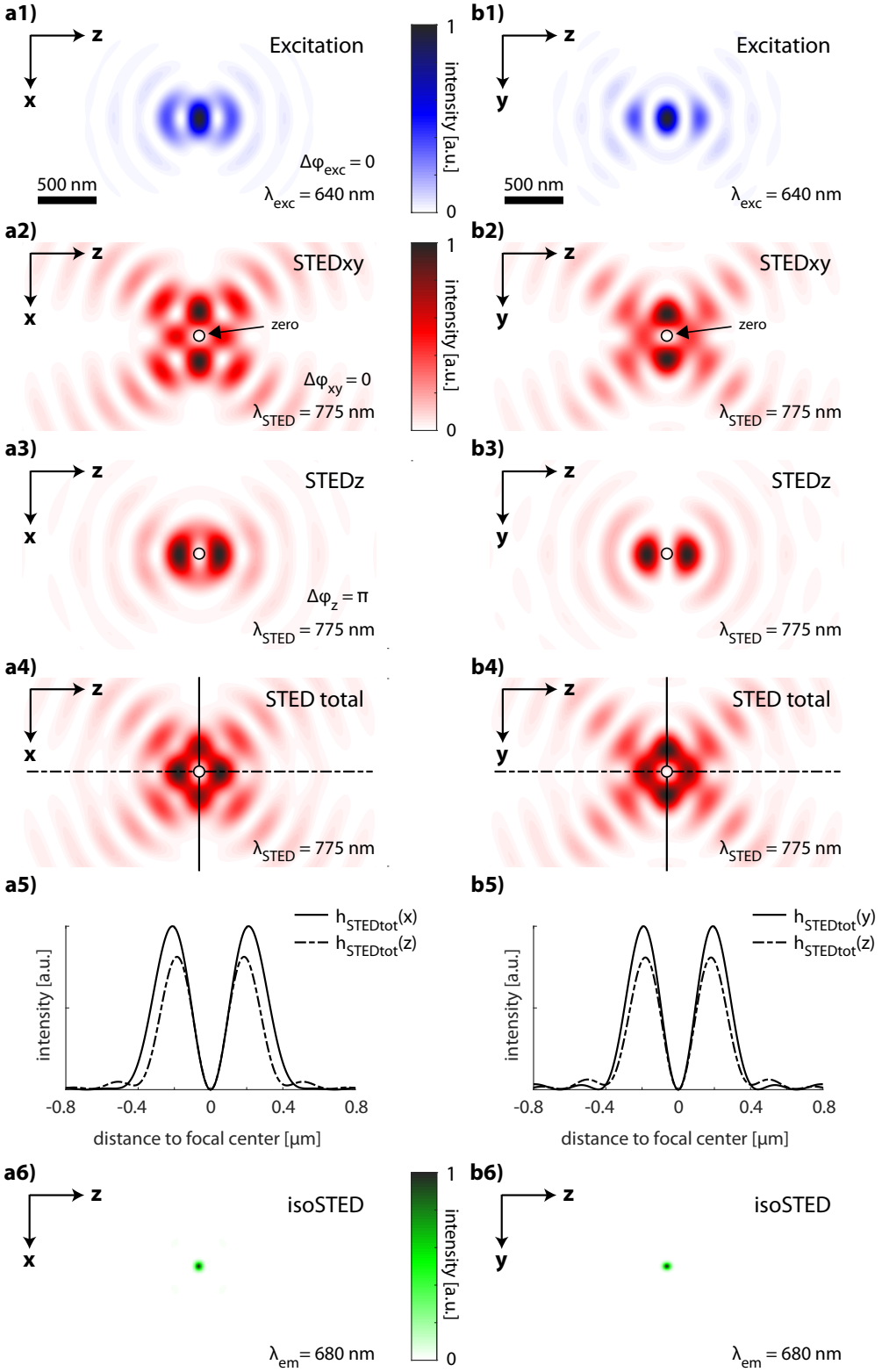

Figure 2.4.: Central **(a)** x-z- and **(b)** y-z-section through the simulated PSFs of the isoSTED microscope. Due to the linearly polarized light, the interference patterns look similar but not the same. **(a1,b1)** Show the interference pattern for excitation. Both depletion patterns, the **(a2,b2)** constructive STEDxy and the **(a3,b3)** destructive STEDz pattern feature a zero-intensity region in the center. **(a4,b4)** Adding them up incoherently and adjusting their intensities allows to create a depletion pattern with the same steepness around the zero-intensity point in axial and lateral direction **(a5,b5)**. **(a6,b6)** As result the region from which fluorescence can still be emitted after fluorescence depletion can be compressed to an isotropic sphere.

the excitation, emission and STED wavelength, respectively. The phase difference of the counter propagating beams is set to zero for the excitation and STEDxy and to π for the STEDz beams. This ensures a constructive interference for excitation and STEDxy and a destructive interference for STEDz at $\vec{r} = (0, 0, 0)$. The central x-z-sections $(x, 0, z)$ and the central y-z-sections $(0, y, z)$ through the PSFs are presented in figure 2.4**a1-a4** and **b1-b4**, respectively. Due to the linear polarization of the light they look similar but not the same. Note, that the interference patterns of the STEDxy beams only posses zero-intensity in the geometrical focus ($x = y = z = 0$) and not along the entire optical axis. This is because the helical phase mask for imprinting the doughnut works best for circularly polarized light. With linearly polarized light residual z-components in the electrical field occur in the focus of each objective. These are only canceled out in the geometrical focus by the focused light of the other objective lens. Therefore, already the STEDxy pattern of the isoSTED microscope increases the axial resolution. The depletion pattern created by the STEDz beam increases the axial confinement of the fluorescence further. The total depletion pattern is given by adding up the STEDxy and STEDz patterns incoherently

$$h_{STEDtot}\left(\vec{r}\right) = h_{STEDxy}\left(\vec{r}\right) + h_{STEDz}\left(\vec{r}\right). \tag{2.19}$$

The effective PSF of the isoSTED microscope is therefore calculated by:

$$h_{eff}^{isoSTED}\left(\vec{r}\right) = h_{ill}^{4Pi} \cdot \eta\left(h_{STEDtot}\left(\vec{r}\right)\right). \tag{2.20}$$

Due to the exponential behavior of the suppression factor for a pulsed STED scheme (see equation 2.15) and the incoherent add up of both depletion beams, the suppression factor of the isoSTED microscope is given by the multiplication the suppression factors of the STEDxy and STEDz beams:

$$\eta\left(h_{STEDtot}\left(\vec{r}\right)\right) = \eta\left(h_{STEDxy}\left(\vec{r}\right)\right) \cdot \eta\left(h_{STEDz}\left(\vec{r}\right)\right). \tag{2.21}$$

We therefore can define two saturation factors, one for the lateral and one for the axial confinement:

$$\begin{aligned} \zeta_{xy} &= I_{STEDxy}^{max}/I_{sat} \\ \zeta_{z} &= I_{STEDz}^{max}/I_{sat}, \end{aligned} \tag{2.22}$$

with I_{STEDxy}^{max} and I_{STEDz}^{max} being the maximum intensity in the respective depletion pattern.

Multiplication with the detection PSF yields the isoSTED PSF

$$h_{isoSTED} = h_{eff}^{isoSTED}\left(\vec{r}\right) \cdot h_{det,real}\left(\vec{r}\right). \tag{2.23}$$

By adjusting the maximum intensities of STEDxy and STEDz, the depletion pattern steepness around the zero-intensity point becomes the same in both directions (see fig. 2.4**a5 & b5**) and the fluorescence can be compressed to an isotropic subdiffraction sized sphere of diameter d [46]:

$$\Delta r_{isoSTED} \approx \lambda / \left(2\mathrm{NA}\sqrt{1 + I_{max}^{STED}/I_{sat}}\right), \tag{2.24}$$

that converges to point for $I_{max}^{STED}/I_{sat} \to \infty$ and a perfect central zero [46]. Sections through the central x-z- and y-z-plane of the isoSTED PSF are depicted in figure 2.4**a6 & b6**, respectively. The saturation factors for the calculation are $\zeta_{xy} = 20$ and $\zeta_z = 2$ for STEDxy and STEDz, and the pinhole radius was set to $p_0 = 0.42$ airy units in order to match our experiment. Note, that the side lobes visible in the 4Pi illumination PSF (see fig. 2.1) are suppressed in the simulated isoSTED PSF.
The isoSTED microscope built up during the doctoral thesis is described and characterized in the following.

3. Experimental realization

3.1. The isoSTED microscope utilizing oil-immersion lenses

The isoSTED setup is based on the design shown by Schmidt et al. [15].

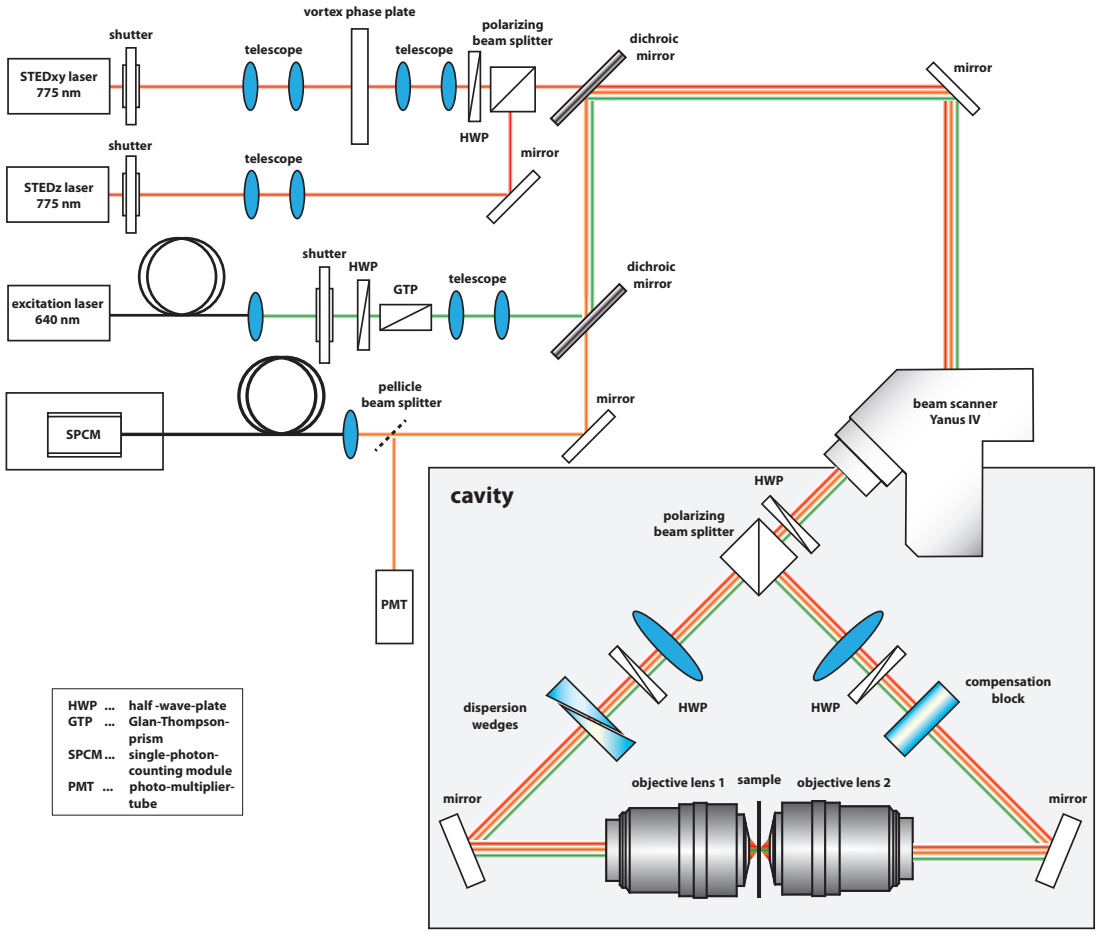

Figure 3.1.: The isoSTED microscope. The beams for excitation, STEDxy (lateral confinement) and STEDz (axial confinement) are combined using an appropriate set of dichroic mirros and directed through a beam scanner into the cavity with two opposing objective lenses (UAPON 100XO TIRF, NA = 1.49, Olympus). A vortex-phase-plate imprints a circular phase mask onto the STEDxy-beam. Emitted fluorescence is collected by both objective lenses and backpropagates along the same optical path to the detector.

Figure 3.1 illustrates the main components of the isoSTED setup. As shown in chapter 2, two incoherent depletion patterns are needed to generate an isotropic effective

illumination PSF. In order to avoid unwanted interference, two independent STED laser systems are used, one for depletion in the lateral direction, the STEDxy-beam, and the other for axial confinement, the STEDz-beam.

The STEDxy-beam is provided by a mode-locked Titanium:Sapphire-laser (Ti:Sa, *Chameleon Ultra II, Coherent Inc., Santa Clara, Ca, USA*), delivering pulses with a temporal FWHM of 140 fs at a wavelength of 775 nm at a repetition rate of 80 MHz. In order to prevent back reflections into the laser-system a Faraday isolator (*IO-5-NIR-LP, Thorlabs, Dachau, Munich, Germany*) is placed directly after the light source. Since the 140 fs pulses are too short for an effective depletion of the fluorescence, the pulses are temporally stretched by a combination of SF6-glass rods and a 120 m long optical fiber (*PMJ-A3HPC, 3S-633-4/125-3-120-1-SP, AMS-Technologies, Martinsried, Germany*). After the fiber the pulses have a temporal width of approximately 600 ps. A vortex phase plate (*VPP-1a, RPC Photonics, Rochester, NY, USA*) is used to imprint a $0 - 2\pi$ radial phase pattern onto the STEDxy-beam profile, such that a doughnut-shaped intensity pattern is formed at the focus of the objective lenses (see chapter 2).

The STEDz-beam is provided by a 775 nm picosecond laser system (*Katana - 08 HP, Onefive GmbH, now part of NKT Photonics, Birkerød, Denmark*), delivering pulses with a temporal width of approximately 600 ps at a repetition rate of 80 MHz. The STEDxy and the STEDz-beams are combined using a polarizing beam splitter.

For excitation, a picosecond diode laser (*LDH-P-C-640B, PicoQuant GmbH, Berlin, Germany*) with a wavelength of 640 nm and a pulse width < 90 ps is used. The temporal delay between excitation and STED pulses is adjusted by custom electronics provided by the electronic workshop of the *Laser-Laboratorium Göttingen e.V.*. A commercial picosecond delayer (*MPD Picosecond Delayer, Micro Photon Devices, Bolzano, Italy*) is used to adjust the relative timing of the STEDxy and STEDz pulses.

Telescopes in the individual beam paths are used to adjust the beam diameters such that the entrance pupils of the objective lenses are illuminated. Additionally, they are used to adjust the divergence of the individual beams. All laser beams are combined utilizing two custom dichroic mirrors (*AHF Analysentechnik, Tübingen, Germany*).

A beam scanner (*Yanus IV, TILL Photonics GmbH, now part of Thermo Fisher Scientific Munich GmbH, Munich, Germany*) is used to move the focal spots generated by focusing the beams with the 100x oil-immersion objective lenses (*UAPON 100XO TIRF, Olympus, Japan*), laterally through the sample.

The isoSTED cavity, underlaid with a grey box in figure 3.1, is designed in a way that beams propagating in the two arms of the cavity experience the same optical

path lengths and therefore interfere at the common focus of both objective lenses. In section 3.3, a closer look at the cavity and its components is provided.
The fluorescence emitted from the sample is collected by both objective lenses incoherently, de-scanned and separated from the laser light by the dichoric mirrors. Additional filters suppress residual laser light in the detection path. A multimode fiber coupled to a single-photon counting module (*SPCM-AQRH-13-FC, Excelitas Technologies, Waltham, MA, USA*) acts as a confocal pinhole. A removable pellicle beam splitter and a photo-multiplier tube (PMT, *Hamamatsu, Japan*) allow for measurements in reflection mode, which are needed for system alignment.
In each laser beam path a fast shutter (*Uniblitz LS6ZM2-NL, Vincent Associates, Rochester, NY, USA*) is implemented to block the lasers separately and thus allowing to switch between confocal and STED imaging.
For electronic component and microscope control, as well as for data acquisition, a multifunction National Instruments Data Acquisition (NIDAQ) card (*PCIe-6363, National Intruments, Austin, TX, USA*) in combination with the acquisition software Imspector (*Abberior Instruments GmbH, Göttingen, Germany*) is used.
While this configuration performs at its best with fixed samples, it has some limitations for live cell imaging. When living cells are under analysis, they have to be embedded in an aqueous medium with nutrients. This results in a refractive index difference between the embedding medium and the immersion medium. Focusing into a mismatched medium causes spherical aberrations that increase with increasing sample depth [47]. The influence of the cover glass is typically corrected by the objective lenses. Therefore, a variant of the presented setup, adapted for live cell imaging is described in the following.

3.2. The isoSTED microscope for live cell imaging

The isoSTED setup for live cell imaging is presented in figure 3.2. The implemented adaptations are highlighted in green boxes.

Objective lenses: In order to minimize the aberrations due to refractive index differences, the oil-immersion objective lenses are replaced by 60x water-immersion objective lenses (*UPLSAPO 60XW, Olympus, Japan*).

STED laser system: Since STED microscopy uses high laser powers, the fluorescent molecules have an increased chance of bleaching. This bleaching scales nonlinearly with the applied STED intensity [48, 49]. STED pulses impinging on molecules in T_1 can effectively pump them into higher triplet states T_n, which are known as starting points for bleaching reactions [29, 44]. With a repetition rate

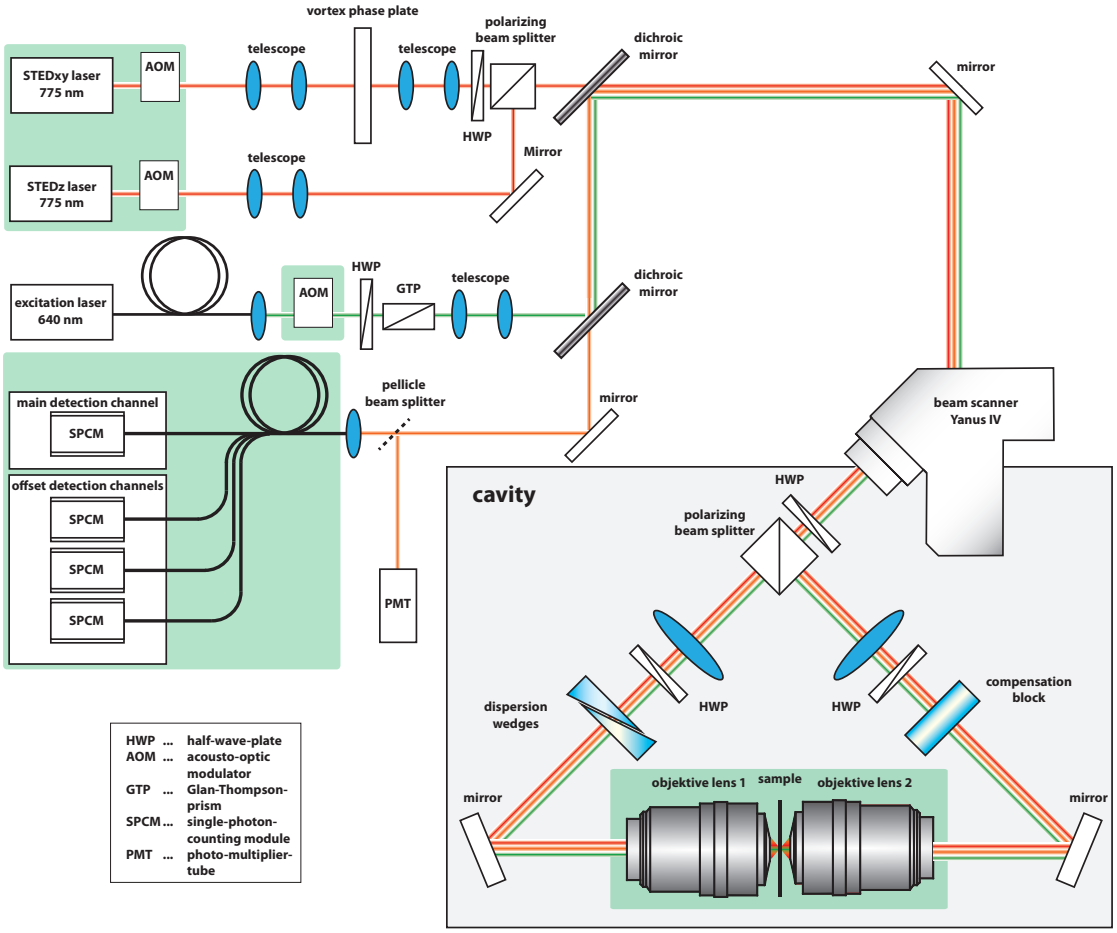

Figure 3.2.: Adaption of the isoSTED microscope for live cell imaging. Changes in the setup are highlighted in green boxes. The objective lenses are changed to water-immersion objectives (UPLSAPO 60XW, NA 1.2, Olympus). STED laser systems with a repetition rate of 30 MHz and acousto-optical modulators that allow to switch off pixelwise reduce the effect of photobleaching. For improving the image quality the detection fiber is replaced by a fiber bundle.

of 80 MHz, a fluorophore in its triplet state will experience on average 80 high intensity pulses before it relaxes back to S_0 (triple lifetime of 1 µs [29]). Therefore reducing the repetition rate and thus decreasing the number of laser pulses that hit the molecules while they are in T_1, reduces the probability of photobleaching. This method is called triplet relaxation (T-Rex) STED. In extreme cases even lasers with only 250 kHz repetition rate are used [29]. In our setup two independent fiber lasers (*PFL-P-30-775-B1R, MPB Communications Inc., Quebec, Canada*) delivering pulses with a temporal width of approximately 900 ps and a wavelength of 775 nm at a repetition rate of 30 MHz are used. This reduces the probability of photobleaching without substantially increasing the data acquisition time.

Acousto-optic modulators (AOM): In order to reduce photobleaching even further, the ability to switch the lasers pixelwise on and off is beneficial. Techniques as RESCue-STED [50] reduce photobleaching by switching the lasers off when enough or no fluorescence is detected within a certain time. This reduces the amount of state transitions as well as the average time the dye molecules stays in the off-state. The so far used shutters have a maximum continuous frequency of 20 Hz, and thus only allow switching from line to line or frame to frame. Faster switching is realized by inserting acousto-optic modulators into the STED beam paths (*AA-MT110-A1.5-IR, AA Opto-Electronic, Orsay, France*) and the excitation beam path (*AA-MT110-A1.5-VIS, AA Opto-Electronic, Orsay, France*). Those modulators utilize the acousto-optical effect to generate a refractive index grating within a glass or crystal by applying sound waves. Incident light is diffracted by this grating. With these AOMs switching of the laser beams on the single pixel level is possible.
To handle the increased amount of electronic signals, e.g. the switching signals for the AOMs, the previously used NIDAQ card is upgraded to an FPGA card (*PCIe-7852R, National Intruments, Austin, TX, USA*) and a patch panel (*Abberior Instruments GmbH, Göttingen, Germany*) is used to simplify the communication between Imspector and the hardware.

Detection: For improving the image quality (see section 4.2.3) the detection path is also changed. The multimode fiber, used as a detection pinhole, is exchanged with a customized 1-7-fan-out fiber (*Thorlabs, NJ, USA*) and three additional single-photon counting modules are implemented (*SPCM-AQRH-13-FC, Excelitas Technologies, Waltham, MA, USA*).

3.3. IsoSTED cavity

Since the cavity is the essential part of the isoSTED microscope, its most important components are described in the following. A schematic drawing of the components in the cavity, as well as a corresponding photograph, are shown in figure 3.3. The cavity is designed as an isosceles right triangle. A polarizing beamsplitter (**pol-BS**) splits incoming light into two beams with orthogonal linear polarization. Those beams propagate along the cathetes of the cavity and are reflected by two mirrors onto its hypotenuse. The now counter propagating beams are focused by the two objective lenses and interfere in the center of the hypotenuse, where the sample is placed. The center of the hypotenuse is called the center of the cavity. Light that is transmitted by the pol-BS follows the transmitted beam path, while reflected light follows the reflected beam path. We hereafter call the individual beam paths within the cavity the arms of the cavity. This symmetrical arrangement of both cavity arms ensures that their optical path lengths match within the pulse length of the lasers. For a fine adjustment of the optical path lengths, the pol-BS can be moved in the direction of the incident beam. Therefore it is mounted on a translation stage equipped with a piezo (*P-841.1, Physik Instrumente GmbH & Co.KG, Karlsruhe, Germany*) to enable a positioning accuracy much finer than the wavelength of the light used.

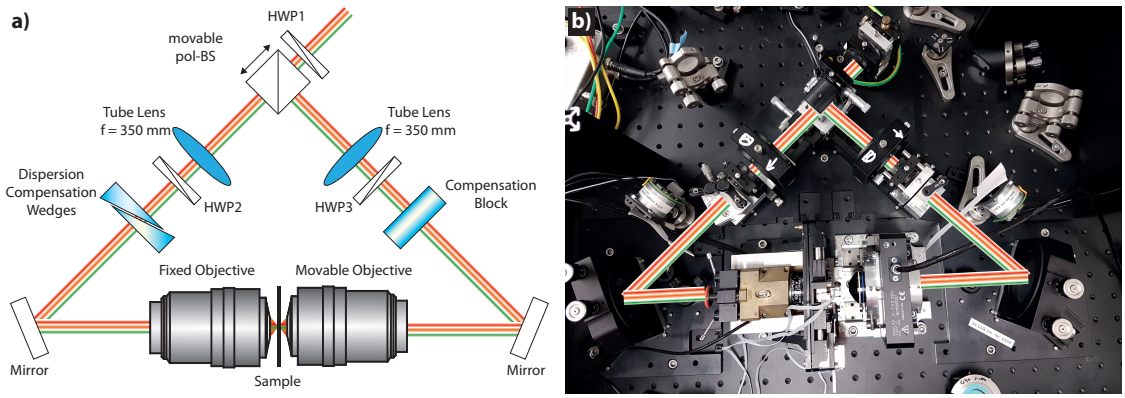

Figure 3.3.: **(a)** Light enters the cavity through a half-wave-plate and is split in two beams by a pol-BS. In the common focus of both objective lenses the counter propagating beams interfere. A pair of glass wedges and a compensation block, allow to compensate optical path length difference within the cavity arms. The pol-BS can be translated in the direction of the incident light to fine tune the pathlength difference. **(b)** Corresponding photograph of the isoSTED cavity.

The laser beams enter the cavity through a half-wave-plate (**HWP**) and the pol-BS. Thus HWP1 allows to rotate the polarization of the incident light and therefore in combination with the pol-BS to adjust the laser power ratio in the transmitted and reflected beam path.

In both paths a **tube lens** with a focal length of f = 350 mm and an additional

HWP (HWP2 & HWP3) are placed. To generate the required depletion patterns the counter propagating STEDxy-beams must interfere constructively, while the STEDz-beams must interfere destructively, in the common focus of both objective lenses. Hence, the phase difference of the counter propagating beams must be zero for STEDxy and π for STEDz. In accordance to [15], this is achieved by using linearly polarized laser beams and a pol-BS. The polarization states in the cavity are illustrated in figure 3.4. Initially the polarization of the STEDxy and STEDz-beams are perpendicular. The polarization of the excitation light is chosen to match the polarization of the STEDxy light (position **1** in figure 3.4**a & c**). The HWP rotates the polarization such that the beams enter the pol-BS at an angle of 45° with respect to the splitting plane (p). After the pol-BS the partial beams of $STED_{xy}$

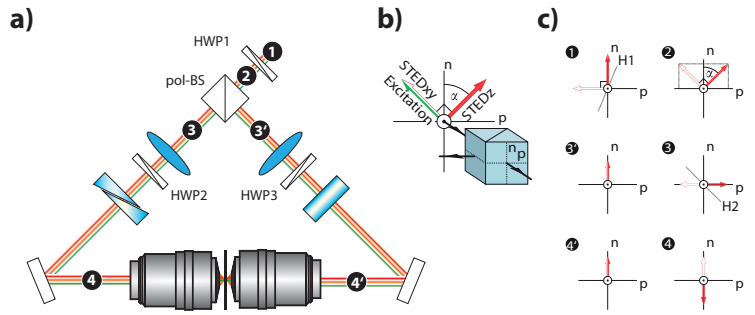

Figure 3.4.: **(a)** Sketch of the isoSTED cavity. Numbers in black circles indicate the position of the light polarization shown in **(c)**. The polarization states of excitation and STEDxy are parallel to each other and perpendicular to STEDz. The beams enter the pol-BS at 45° with respect to its splitting plane **(b)**. Right behind the pol-BS, the partial beams of STEDxy and STEDz are mutally orthogonally polarized (positions 3 and 3') [15]. HWP2 rectifies a polarization for both beam pairs (position 4 and 4') with a phase difference of π. H1 and H2 indicate the orientation of HWP1 and HWP2 (modified in accordance to [15])

and $STED_z$ are mutually orthogonally polarized (position 3 and 3'). The additional HWP rectifies a parallel polarization for both beam pairs with phase difference of π between both beam pairs (position 4 and 4') [46]. Actually one HWP would be sufficient to achieve this, however the second is needed for the symmetrical design of the cavity.

Like the STEDxy light the excitation light needs to interfere constructively in the common focus. Therefore, the phase difference needs to be set for both involved wavelengths (λ_{exc} = 640 nm, λ_{STED} = 775 nm) simultaneously, which necessitates to take dispersion effects into account. Optical components are produced with a certain tolerance, e.g. in thickness, and thus it is unlikely to have 100% identical optical components within both cavity arms. Despite those variations being small for a single element, they add up in a complex system, e.g. an objective lens, that contains many lenses, or the entire isoSTED cavity. The resulting optical path

length difference (**OPD**) is the sum of the path length differences of each material in the cavity:

$$OPD\left(\lambda\right) = \sum_i n_i\left(\lambda\right) \cdot \Delta d_i, \tag{3.1}$$

with $n_i\left(\lambda\right)$ being the refractive index and Δd_i the path length difference of the $i-th$ material. The OPD results in a wavelength dependent phase difference

$$\Delta\Phi\left(\lambda\right) = \frac{2\pi}{\lambda} \cdot OPD\left(\lambda\right), \tag{3.2}$$

which adds to the previously set phase differences of zero and π. In order to adjust the OPD we inserted a pair of glass wedges (**Dispersion Compensation Wedges**; BK7 glass) into the transmitted and a **Compensation Block** (BK7 glass) into the reflected beam path of the cavity. The glass wedges could be shifted with respect to each other to add glass into or remove glass from the cavity and thus achieving a stable phase difference over a wide spectral range. The thickness of the compensation block was chosen such, that it compensates the thickness of the wedges in their zero position.

Although the immersion medium of the objective lenses and the embedding medium of the sample are chosen to match each other, the refractive index of the sample can still be slightly different, or even vary within the sample. Thus the optical path length difference and hence the phase difference between both cavity arms must be fine tuned before each measurement. Moving the pol-BS in or opposite the direction of the incident beam adds or removes air in the transmitted beam path and thus changes the OPD. This allows to compensate for refractive index differences of the sample and the immersion medium. A further advantage of the pol-BS on the piezo translation stage becomes apparent when the sample is moved in the axial direction during the measurement. Due to the refractive index difference between the sample and the immersion medium, the optical path length and thus the phase difference is changed when the sample is moved axially. By synchronizing the movement of the sample stage with the movement of the pol-BS it is possible to maintain constructive interference for excitation and STEDxy, as well as destructive interference for STEDz, throughout the entire sample depth.

Objective lenses and sample stage

The objective lenses are the optical components whose optical quality affects the performance of the microscope most. Their NA defines the smallest possible spot size to which the laser light can be focused and their opening angle directly relates to the fluorescence collection efficiency. The objective lenses have a high transmission in the spectral range from 640 nm (λ_{exc}) to 775 nm (λ_{STED}) and are corrected for

spherical and chromatic aberrations.
Spherical aberrations occur when extended incident light beams are focused by a spherical lens. In the paraxial approximation, the entire beam is focused onto the geometrical focus. However, this paraxial approximation does not apply to extended light beams. Due to the curvature of the lens, light that strikes the lens further away from the optical axis is refracted more strongly than light close to the optical axis. The refraction for off-axis light is so strong that it is no longer focused onto the geometrical focal point, but further and further towards the lens as the distance to the optical axis increases.
Chromatic aberrations are caused by the dispersion of the lens. Different wavelengths experience a different refractive index in the materials and are therefore focused onto different points on the optical axis, causing a wavelength dependent focus shift.
To generate the desired excitation and depletion patterns the focal spots of both objective lenses must overlap congruently for both, the excitation and depletion wavelength. Although the objective lenses are corrected for chromatic aberrations and thus chromatic focus shifts, slight variations in the optical properties of the objectives lenses due to the production process are usually observed. A compensation of the residual chromatic focal shift can be achieved for one objective lens. In order to do that, the aforementioned telescopes (see section 3.1) are used to change the divergence of the laser beams for one wavelength and thus ensure an overlap of the foci for λ_{exc} and λ_{STED}. As the telescopes are outside the cavity, the divergence is changed for both cavity arms simultaneously. Therefore, the excitation and STED foci of the second objective lens only overlap, when its chromatic focus shift is identical or very similar to that of the first objective lens.

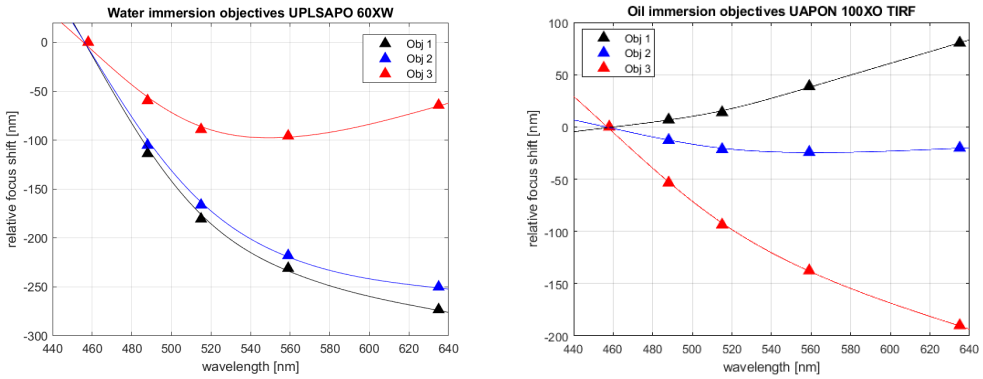

Figure 3.5.: Wavelength dependent chromatic focus shift along the optical axis for the water- **(a)** and oil-immersion objective lenses **(b)** relative to the focus position $\lambda = 458$ nm. Splines are fitted to show the general behavior. In both cases Obj 1 and Obj 2 show the most similar behavior.

In order to select the objective lenses which are suitable for our application, three water and three oil immersion lenses were tested. For each, the axial focus posi-

tion for five wavelengths (458 nm, 488 nm, 515 nm, 559 nm and 635 nm) relative to the axial focal position of $\lambda_{\text{ref}} = 458$ nm was determined. The objective lenses were successively inserted into a confocal microscope and their correction ring was set to the optimal position, such that the recorded signal was maximized and no spherical aberrations were visible in the measured data. A sample containing a metal coated cover glass was mounted and scanned axially through the focus of the objective lens. The total scan range was 8 µm with a step size of 0.1 µm. For each z-position the reflected signal was acquired. To determine the axial focus shift for the different wavelengths, this signal was plotted against the respective z-positions and fitted with a Gaussian. Subtracting the central position of the Gaussian fit for the measurement wavelength from the center of the Gaussian fit for the reference wavelength determined the relative focus shift.
Figure 3.5 shows the wavelength dependency of the relative axial focus shift for the tested water and oil immersion lenses. As a guide for the eyes splines were fitted to the data. For the water-immersion lenses, the objective lenses labeled as Obj 1 and Obj 2 showed a matching behavior, while the behavior of Obj 3 deviates strongly. For the oil-immersion lenses the behavior of Obj 1 and Obj 2 was the most similar, but not as similar as for the water-immersion lenses. Therefore in both cases Obj 1 and Obj 2 are used for the following measurements.

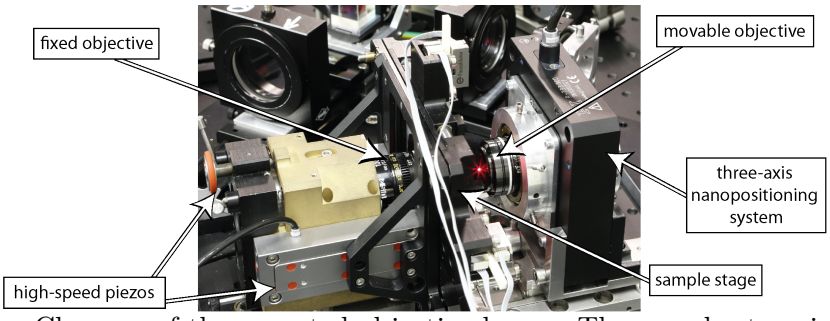

Figure 3.6.: Close up of the mounted objective lenses. The sample stage is attached to two high-speed piezos (axial scanning) that are mounted on the holder of the fixed objective lens. The movable objective lens is placed in a three-axis nanopositioning system.

A close up of the mounted objective lenses and the sample holder is shown in figure 3.6. One objective lens is mounted in a hollow cylinder, which is then placed on a V-shaped block so that the optical axis of the objective lens is aligned with the beam path. Since it has no further adjustment options, it is referred to as the **fixed objective** lens in the following.
The second objective lens, also mounted in a hollow cylinder, is held in another cylinder separated by two O-rings. This allows to tilt the objective in any direction by using adjustment screws and thus to align the objectives such that their focal planes are parallel. This arrangement is integrated into a **three-axis nanopositioning system** (*P-733.3DD, Physik Instrumente GmbH & Co.KG, Karlsruhe, Germany*)

so that the foci of both objective lenses can be superimposed. As this objective can be moved for alignment it is called the **movable objective** lens in the following.
The sample stage is attached to the holder of the fixed objective lens and consists of a custom x-y stage with two piezos (*Piezo LEGS® Linear Twin 20N, PiezoMotor, Sweden*). Two screws allow to tilt the sample stage in order to align the sample with respect to the common focal plane of the objectives. Three magnets are embedded in the sample stage in order to keep the magnetic sample holder at its position.
During a measurement x-y-scanning is performed by the beam scanner. Axial scanning is done by moving the sample stage utilizing two high-speed linear piezo stages (*LISA P-753.3CD, Physik Instrumente GmbH & Co.KG, Karlsruhe, Germany*).
All non-commercial parts of the cavity were produced by the mechanics workshop of the Max-Planck institute for biophysical chemistry.
Super-resolution microscopy is only possible if the mechanical instabilities and drift, e.g. thermal drift, in the setup are smaller than the expected resolution. Therefore, the stability of the cavity is analyzed in the following.

Stability

The system consisting of both objective lenses and the sample stage has the biggest influence on the stability of the setup. Since the objective lenses have the largest magnification of all lenses within the entire setup, every movement of the sample stage or the objective lenses with respect to each other influences the imaging performance negatively. Therefore, the stability is tested in two steps. At first, the stability of the objective lenses with respect to each other and afterwards the stability of the sample holder with respect to the fixed objective lens is analyzed.

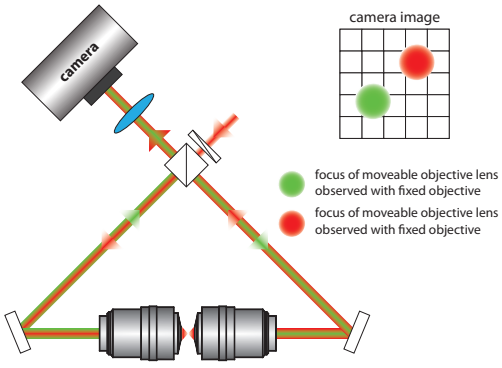

Figure 3.7.: Sketch of the setup used for stability measurements of the objective lenses with respect to each other. Both objective lenses focus incident parallel light and simultaneously detect the focus of the other objective. The foci are imaged onto a camera.

Figure 3.7 illustrates the setup used for testing the stability of the objective lenses. Each objective lens focuses the incident light and simultaneously detects the light

focused by the opposing objective lens, which is then imaged onto an EMCCD camera (*IXON, Andor Technology, Belfast, UK*). The movable objective lens is shifted laterally using the three-axis nanopositioner until the images of both foci are seen as two clearly separated spots on the camera. The readout area of the camera is limited to these spots in order to decrease the acquisition time.
In order to distinguish between instabilities on short and long time scales, two different measurements are performed. For the long time scales, an image is taken every second for five minutes with a dwell time of 10 ms, while for the short time scales, 5,000 camera frames are obtained consecutively, with 1 ms dwell time. The recorded images are analyzed using a localization algorithm that is used e.g. in PALM [51]. This algorithm identifies the spots in the image, fits a Gaussian to them, and maps their positions into a position histogram.
The position histograms of the focus of the fixed objective lens observed with the movable objective lens are presented in figure 3.8. The graphs for the short time scale measurement are shown in figure 3.8**a & b** and for the long time scale measurement in figure 3.8**c**. Each data point represents the localized position of the focus in one image corresponding to one time point. The time is color coded. Early data points are depicted in blue and late data points in red. Note that the origin of the position is set to the average position during the measurement. Since the focus of the movable objective lens observed with the fixed objective lens shows the same behavior, only the focus of the fixed objective lens is analyzed. Even though the

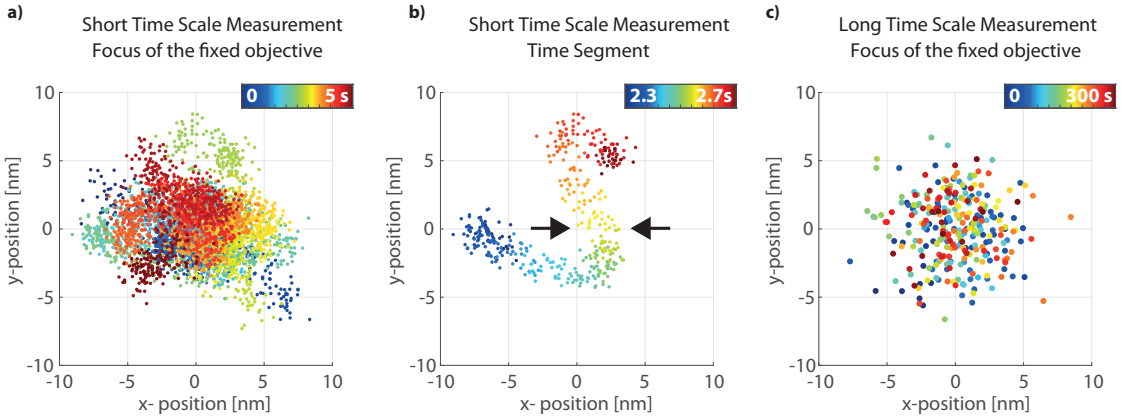

Figure 3.8.: Stability of the objective lenses with respect to each other: Temporal change of the localized position of the focus of the fixed objective lens observed with the movable objective lens in a **(a, b)** short time scale and **(c)** long time scale measurement. **(b)** A closer look at only a time segment reveals that the change consists of two contributions: The error due to the localization process and a directed movement of the objective lenses with respect to each other. As the first contribution is small the standard deviation, σ, of the focus position is an upper estimate for the stability of the objective lenses with respect to each other ($\sigma \leq 2.9$ nm).

change in the focus position looks arbitrary (see fig. 3.8**a**), a closer look at only a

time segment ranging from 2.3 - 2.7 s (see fig. 3.8**b**) shows a directional contribution. The change of the focus position can be quantified by its standard deviation, σ, and attributed to two effects. First, the error due to the localization process, σ_{loc}, and second, movements of the objective lenses with respect to each other, σ_{mov}. The smaller fluctuations in figure 3.8**b**, indicated by the two arrows, show the contribution of the localization accuracy, whereas the overall change is dominated by the movement of the objective lenses. As both contributions are statistically independent σ is given by $\sigma = \sqrt{\sigma_{\mathrm{loc}}^2 + \sigma_{\mathrm{mov}}^2}$. Since $\sigma_{\mathrm{loc}} \ll \sigma_{\mathrm{mov}}$, the calculated values for σ are good upper estimates for the stability of the objective lenses with respect to each other. We get $\sigma_{\mathrm{x}} = 2.9$ nm and $\sigma_{\mathrm{y}} = 2.1$ nm for the short time scale measurement and $\sigma_{\mathrm{x}} = 2.5$ nm and $\sigma_{\mathrm{y}} = 2.4$ nm for the long time scale measurement.

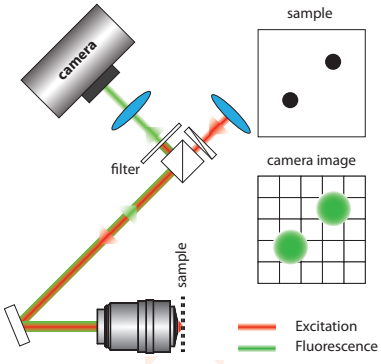

Figure 3.9.: Sketch of the setup used for stability measurements of the sample stage with respect to the fixed objective lens. Incident light is focused into the back-focal plane of the objective for wide-field illumination. The fluorescent signal emitted by excited crimson fluorescent beads is imaged onto the camera.

In order to analyze the stability of the sample stage with respect to the fixed objective lens, a lens is inserted into the beam path to focus the incident light onto the back focal plane of the objective lens for wide-field illumination (see fig. 3.9). A sample containing crimson fluorescent beads with a diameter of 200 nm (*F8806, Thermo Fisher Scientfic, Waltham, MA, USA*), prepared following a standard protocol (see appendix A) is placed on the sample stage. The emitted fluorescence is collected by the fixed objective lens, separated from the excitation light by a filter and imaged onto the camera. The acquired images are analyzed as before.
In the figures 3.10**a & b** the change of the position of two beads (1 and 2) within is shown. In comparison to the focus position in figure 3.8**a & b** no directed change is visible. Since the fixed objective is tightly screwed, directed contributions can only stem from a movement of the sample stage σ_{sample} (e.g. drift).
The detected fluorescence signal is much weaker than the signal detected from the foci in the previous measurement. As the the localization accuracy is proportional to the detected spot size and the inverse of the square root of the total number of

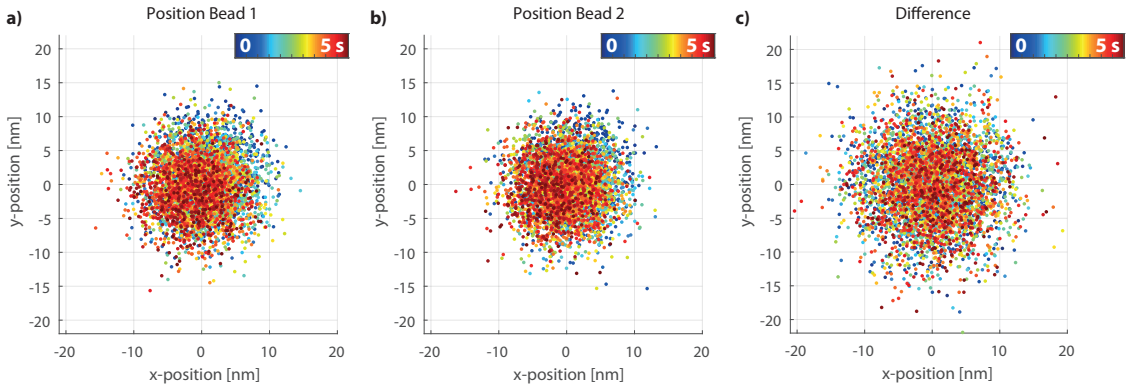

Figure 3.10.: Stability of the sample stage with respect to the fixed objective lens (short time scale measurement): **(a,b)** Temporal change of the localized position of two fluorescent beads and their difference **(c)**. The standard deviation is a measure for the localization error $\sigma_{\mathrm{locX}} = 3.8$ nm and $\sigma_{\mathrm{locY}} = 3.9$ nm in x- and y-direction. The influence of the sample stage on the overall movement in **(a,b)** is less than 2 nm.

detected photons, a larger influence of the localization process on the bead position is expected. In order to determine the influence of the localization process, the difference of the positions of both beads is calculated for each time point. This eliminates the effects of any directed contributions. The graph in figure 3.10**c** shows this quantity. The standard deviation of the difference σ_{diff} is a measure for the localization accuracy σ_{loc}. As the localization accuracy is the same for both beads ($\sigma_{\mathrm{loc1}} = \sigma_{\mathrm{loc2}} = \sigma_{\mathrm{loc}}$), the standard deviation of the difference is given by $\sigma_{\mathrm{diff}} = \sqrt{\sigma_{\mathrm{loc1}}^2 + \sigma_{\mathrm{loc2}}^2} = \sqrt{2} \cdot \sigma_{\mathrm{loc}}$. We get $\sigma_{\mathrm{locX}} = 3.8$ nm and $\sigma_{\mathrm{locY}} = 3.9$ nm.
Using this information, we can estimate the systemic influence on the relative bead positions in figure 3.10**a & b**. The standard deviations for the bead positions are $\sigma_{\mathrm{Bead1x}} = 4.1$ nm, $\sigma_{\mathrm{Bead1y}} = 4.2$ nm, $\sigma_{\mathrm{Bead2x}} = 4.0$ nm and $\sigma_{\mathrm{Bead2y}} = 4.1$ nm, which is slightly larger than the localization accuracy. The systemic influence can be estimated via $\sigma_{\mathrm{sys}} = \sqrt{\sigma_{\mathrm{Bead}}^2 - \sigma_{\mathrm{loc}}^2}$ to be less than 2 nm.

The data for the long time scale measurement is presented in figure 3.11. In the graphs for the bead positions 3.11**a & b** a directed change in x-direction is visible for both beads. This becomes even more evident when looking at the time traces of the x- and y-position of bead 1 depicted in 3.11**d & e**. While the y-position remains stable over time, the x-position changes by approximately 20 nm. The standard deviations are $\sigma_{\mathrm{Bead1x}} = 7.1$ nm, $\sigma_{\mathrm{Bead1y}} = 5.6$ nm, $\sigma_{\mathrm{Bead2x}} = 7.0$ nm and $\sigma_{\mathrm{Bead2y}} = 5.1$ nm.
Calculating the difference of the bead positions (see fig. 3.11**c**) removes the influence of the directed change. We get a localization accuracy of $\sigma_{\mathrm{locX}} = 3.8$ nm and $\sigma_{\mathrm{locY}} = 3.9$ nm. Thus, the systemic influence can be estimated with $\sigma_{\mathrm{sys,x}} \approx 6$ nm and $\sigma_{\mathrm{sys,y}} \approx 4$ nm. Especially in x-direction this is larger than σ_{locX} and therefore

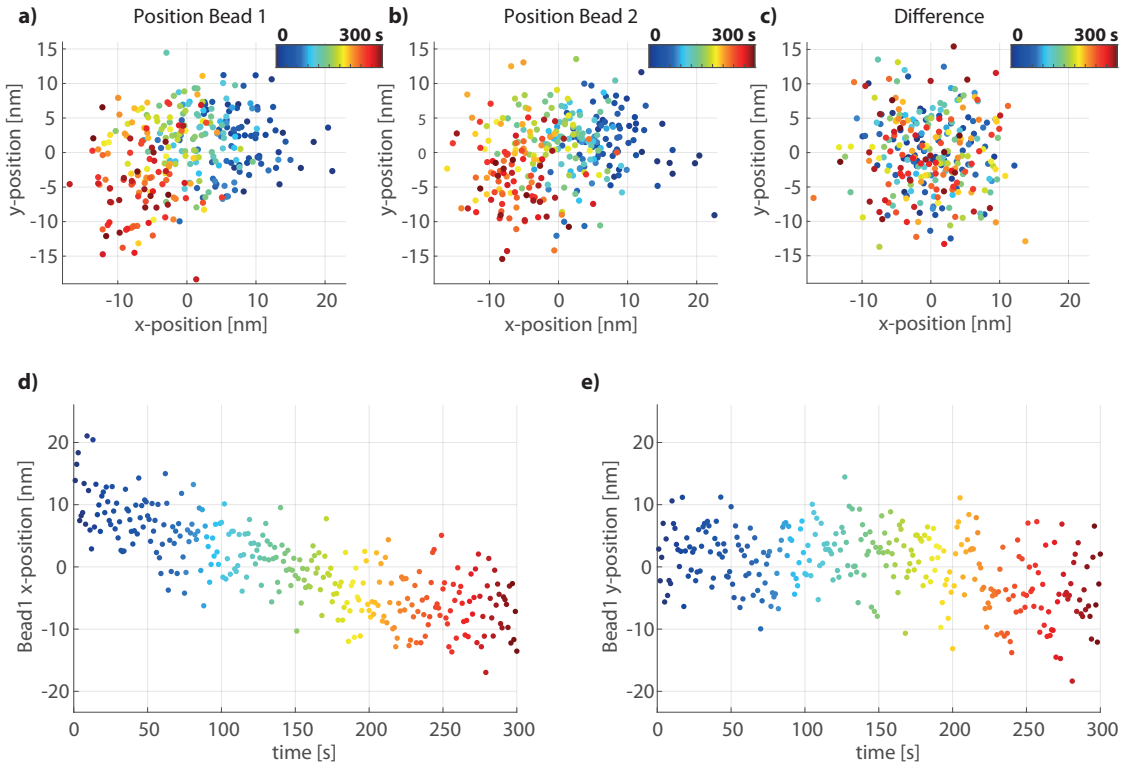

Figure 3.11.: Stability of the sample stage with respect to the fixed objective lens (long time scale measurement): **(a,b)** Temporal change of the localized position of two fluorescent beads and their difference **(c)** in the long time scale measurement. **(d,e)** Time traces of the x- and y-position of Bead1 show a movement of the sample stage in x-directions. After 300 s the x-position stabilizes.

the dominant contribution. As both bead positions show this change in x-direction it can be accounted to a drift of the sample stage. It appears that the x-position in figure 3.11**d** stabilizes at the end of the measurement.

As the acquisition of a three dimensional isoSTED data stack is in the range of some minutes to tens of minutes, the results for the long time scale provide a good indication on the stability of the setup during a measurement. Waiting five minutes after placing the sample allows the sample stage to settle into a stable position. The short time scale is comparable to acquiring one image plane. Overall the systemic contributions are small compared to the expected resolution of 30 nm and 50 nm for oil- and water-immersion lenses, respectively. Therefore, the microscope is sufficiently stable for isoSTED imaging.
In order to acquire a three-dimensional isoSTED stack the sample is moved axially. The influence of axial scanning on the stability of the setup is analyzed in the following.

Axial scan speed

Axial scanning is performed by two high-speed piezo stages that move the sample stage with respect to the fixed objective. The piezos are mounted vertically on the holder of the fixed objective lens. In the software (NanoCapture), they are defined as one single axis whose z-position is the mean value of the two individual piezos. Since the manufacturer can only supply parameters, e.g. the maximum scan frequency or the resonance frequency, for the horizontally mounted piezos and since these parameters are dependent on the load, we have to test how fast we can scan without influencing the stability of the setup. Therefore, the previous stability measurements on the short time scale are repeated while performing a sinosoidal z-scan with an amplitude of 2 µm and an image dwell time of 2 ms. This mimics the process of e.g. continuously measuring a x-z plane.

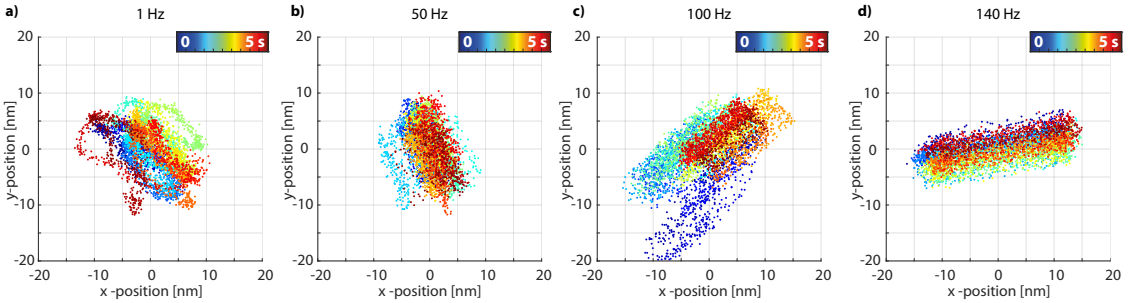

Figure 3.12.: Influence of axial scanning on the stability of the objectives with respect to each other: The temporal change of the position of the fixed objective lens observed with the movable objective shows that at frequencies larger than 100 Hz the stability of the objective lenses with respect to each other is decreased due to resonant vibrations.

As for the stability measurements, at first the influence of axial scanning on the focus position of the objective lenses is analyzed. The movable objective lens has no physical contact to the fixed objective lens and the sample stage. Thus, the observation of the focus of the fixed objective lens allows conclusions whether resonant vibrations arise and transfer to the objective lens during axial scanning. In figure 3.12 the position of the focus of the fixed objective lens observed with the movable objective lens is shown for axial scan frequencies of 1 Hz, 50 Hz, 100 Hz and 140 Hz. For 1 Hz and 50 Hz the position of the focus is as stable as in the case of no scanning (see fig. 3.8**a**). At a scan frequency of 100 Hz the temporal change of the focus position increases. It increases even more when the scan frequency is increased to 140 Hz. In these cases it is clearly visible that the focus of the fixed objective lens moves in x- and y-direction. As the objective lens is fixed and only the sample stage is moved in z-direction, these movements originate from resonant vibrations that couple from the sample stage to the holder of the fixed objective lens.

In order to investigate the behavior of the sample stage during axial scanning, a

sample containing fluorescent beads was scanned through the focus of the fixed objective lens. Figure 3.13 shows the position of one bead for different scan frequencies ranging from 1 Hz to 140 Hz. Already for a scan frequency of 1 Hz (fig. 3.13**a**) it is visible that the change in the bead position over time and is not centered around the zero position. The inset in the graph is a close up of the bead position. Two regions can be identified in the data distribution. One in which the data points are located densely (red box) and the other in which the data points are distributed in a club like shape and are scattered further apart (blue box). A skewed movement of the sample stage would lead to a symmetrical change in the bead position and can therefore be excluded. Thus the observed change in the bead position is caused by imperfections of the detection PSF.

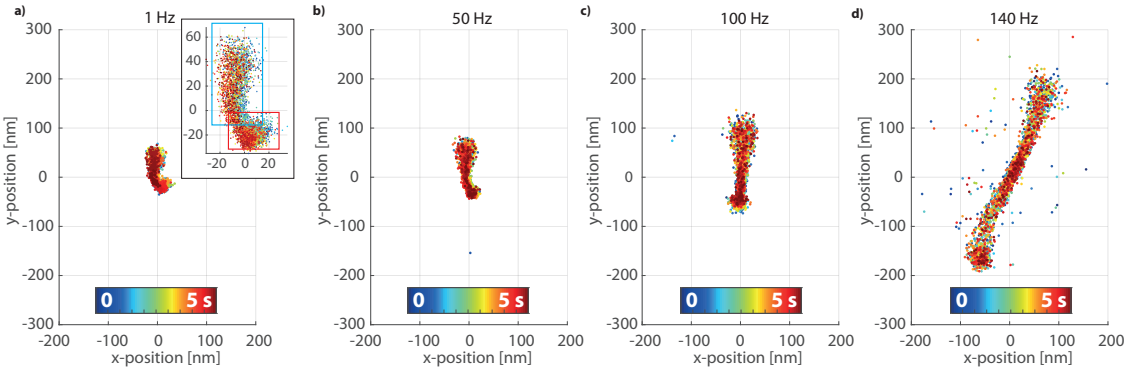

Figure 3.13.: Influence of axial scanning on the stability of the sample stage with respect to the fixed objective lens: **(a)** At low axial scan frequencies the detection PSF of the setup is imaged. **(b-d)** At increasing scan frequencies resonant vibrations couple to the sample stage and lead to oscillations of the sample stage in x- and y-direction. This effect is stronger than the resonant vibrations that couple to the fixed objective lens.

When the bead is in the focus of the objective lens its recorded image is the smallest and thus the localization accuracy is the best. Data points within the densely packed region (red box) belong to images in which the bead is in focus or just slightly defocused. The club like region (blue box) shows that during the defocusing of the bead the localized bead position moves in y direction. As this deviation is not symmetrical, we assume that it is the same for defocusing in both directions. Therefore, we can assume that the detection PSF is aberrated with coma.
With an image dwell time of 2 ms, the z-scan is sampled with a frequency of 500 Hz and thus one axial scanning period of e.g. 1 Hz, 50 Hz or 100 Hz, consists of 500, 10 or 5 images, respectively. Hence, for low scan frequencies the PSF is well sampled, while for faster scans each image is an average of signal from several scan positions. Up to an axial scan frequency of 50 Hz the general behavior of the bead positions does not change. As the scan frequency approaches the resonance frequency of the system consisting of the high-speed piezos, the sample stage, and the sample, resonant vibrations give rise to oscillations in lateral directions. Already for 100 Hz

an additional oscillation in y-direction, that intensifies and translates into the x- and y-direction for larger frequencies (e.g. see fig. 3.13**d**), occurs. Note, that the oscillations observed in the stability measurements of the sample stage with respect to the fixed objective lens are larger than the oscillations observed in the stability measurements of the objective lenses with respect to each other (see fig. 3.12). In order to avoid these resonant vibrations the axial scan frequency should be less than 70 Hz.

Although most data sets are recorded with z-axis as the slow axis, our microscope offers the possibility to perform measurements with axial scanning frequencies of up to approximately 70 Hz. The limiting factor are resonant vibrations of the sample stage. Thereby it has to be considered that for such measurements the resolution is slightly worse due to small vibrations of the system.

3.4. Alignment steps before a measurement

Before starting an acquisition the foci of both objective lenses must overlap congruently. Therefore at first the sample is moved into the focus of the fixed objective lens. Then the movable objective is moved in axial direction until its focus is in the sample plane. Afterwards, a bead or a distinct feature in the sample serves as an alignment aid to shift the focus of the movable objective laterally onto the focus of the fixed objective. For the best possible axial superposition, x-z sections of the alignment aid are recorded and the axial position of the movable objective is fine tuned.

In order to generate the constructive interference patterns for excitation and STEDxy and destructive interference pattern for STEDz, the optical path length difference within both cavity arms must be adjusted. Translating the pol-BS at the entrance of the cavity compensates for small path length differences within the cavity arms.

4. IsoSTED microscopy

In order to test the performance of the isoSTED microscope under optimal conditions oil-immersion objective lenses are utilized (see section 4.1). Afterwards the setup is adapted in accordance to section 3.2 to match the imaging conditions in living cells. The resolution of the isoSTED microscope utilizing water-immersion lenses is analyzed (see section 4.2) and isoSTED imaging in living cells is demonstrated (see section 5).

4.1. IsoSTED microscopy utilizing oil-immersion objective lenses

As shown in chapter 2, the resolution of a microscope strongly depends on the NA of the objective lenses. A high NA allows to focus the incident light to the smallest possible spot. Additionally, a large semi aperture angle allows to collect more emitted light from the sample. The objective lens with the largest NA of 1.57 is from Zeiss (*420792-9771-000, Carl Zeiss Microscopy GmbH, Jena, Germany*). It requires using high refractive index oil ($n = 1.66$) in combination with special cover glasses. The semi-aperture angle of this objective lens is $\approx 71°$.
The oil-immersion objective lenses used in our setup have a slightly lower NA (NA = 1.49), but a larger semi-aperture angle of $\approx 79°$. They can be used with standard immersion oil ($n_{\text{oil}} = 1.518$) and standard cover glasses and are therefore more versatile than the Zeiss objective lenses.
In super-resolution microscopy already small aberrations deteriorate the performance of the microscope. Since focusing light with a high NA objective through an interface with a refractive index mismatch introduces spherical aberrations [5, 6], it is beneficial to match the refractive indices of immersion medium, cover glass and sample. The immersion oil is designed to match the refractive index of the cover glass. A matching index of the sample can be achieved by embedding it in a mixture between phosphate buffered saline (**PBS**) and 2'2-Thiodiethanol (**TDE**) [52]. By adjusting the volume ratio of water to TDE, a refractive index of the mixture can be set between $n_{\text{PBS}} \approx 1.333$ and $n_{\text{TDE}} = 1.5215$. A mixture of 97 % TDE and 3 % PBS perfectly matches the refractive index of the immersion oil.

In summary, the use of oil-immersion lenses enables the minimization of aberrations by refractive index matching and allows to focus light to the smallest possible spot size and ensures that as much fluorescence as possible is collected. This chapter analyzes the resolution capability of the isoSTED microscope on fluorescent beads and its suitability for measuring fixed cells.

4.1.1. Resolution

In order to test the resolution capability of the isoSTED microscope utilizing oil-immersion lenses, a bright test sample of known size is needed. Therefore, we decided to use polystyrene microspheres loaded with a crimson dye. These fluorescent beads can be excited and depleted with our laser wavelengths $\lambda_{exc} = 640$ nm and $\lambda_{STED} = 775$ nm. A layer of spatially separated beads is created by placing a drop of sonicated bead suspension on a cover glass. The sample is embedded in a 97 % TDE solution, covered with a second cover glass and sealed with nail polish and placed into the isoSTED microscope. For the full sample preparation protocol see appendix A. A data stack with a size of 20 µm x 1.5 µm is acquired with a pixel size of 10 nm x 10 nm, a 10 µs pixel dwell time and with laser powers of $P_{Exc} = 0.4$ µW, $P_{STEDxy} = 13$ mW and $P_{STEDz} = 1.3$ mW in the back-focal plane of each objective lens.
Figure 4.1**a** shows an x-z-section through a recording of a fluorescent bead of 25 nm size (*F8782, Thermo Fisher Scientific, Waltham, MA, USA*) for 4Pi and isoSTED imaging. The primary side lobes visible in the 4Pi image disappear when the STED beams are applied.

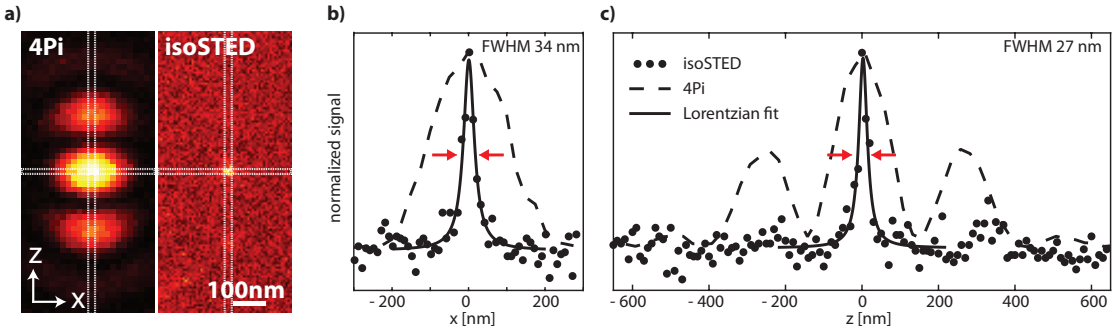

Figure 4.1.: IsoSTED measurement on 25 nm-diameter crimson fluorescent beads: **(a)** X-z-section through the center of a bead acquired with 4Pi illumination. The primary side lobes are clearly visible. **(b)** In the isoSTED measurement the detected spot is shrunk and no residual side lobes are visible. **(b,c)** Lorentzian fits of the averaged line profiles in x- and z-direction through the center of the bead result in measured bead size of 34 nm and 27 nm in lateral and axial direction.

In the bead image, the pixel with the maximum signal count is called the center of the bead. To determine the resolution in the image, the signal count of pixels along an arbitrary line, e.g. a column or row in the picture, is plotted against its

position on that line. Such a curve is called a line profile. Hence, the line profile in x-direction through the center of the bead in figure 4.1**a** is the signal count along the row through the center of the bead plotted against the x-position. In order to increase the signal-to-noise ratio, the signal count of three parallel, neighboring line profiles is averaged. These averaged line profiles are fitted with Lorentzian curves to derive their FHWMs. The averaged line profiles through the center of the bead in x- and z-direction are displayed in figure 4.1**b** & **c**, respectively. Dashed lines show the line profiles for the 4Pi image, whereas the points show the isoSTED line profiles. The line profiles for the isoSTED image have an $FHWM_x = 34$ nm and an $FHWM_z = 27$ nm. Considering the fact, that the bead size is already specified as 25 nm by the manufacturer, our isotropic resolution is better than the calculated FWHM of 34 nm.

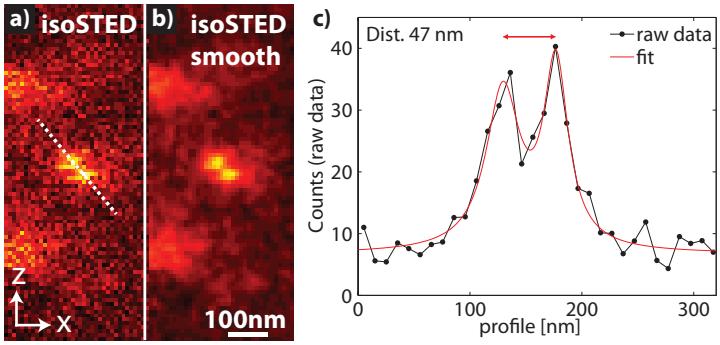

Figure 4.2.: IsoSTED measurement on 48 nm-diameter crimson fluorescent beads: **(a)** X-z-section through two adjacent beads and **(b)** their smoothed image. **(c)** A double Gaussian fit to a line profile through the beads gives a distance of 47 nm which corresponds to their diameter.

Another example for the resolution capability is presented in figure 4.2. A sample containing crimson fluorescent beads with a diameter of 48 nm is measured at 10 nm x 10 nm pixel size and 5 µs pixel dwell time. The applied laser powers are P_{Exc} = 0.3 µW, P_{STEDxy} = 5.4 mW and P_{STEDz} = 0.9 mW in the back-focal plane of both objective lenses. Figure 4.2**a** shows the raw data of an x-z-section of two adjacent beads. Already in the raw data it is apparent that the touching beads can be resolved. This becomes even more evident when the data is smoothed (see fig. 4.2**b**). The averaged line profile along the dashed line in the raw data is shown in figure 4.2**c**. Fitting the data with a double Gaussian function yields a distance of 47 nm between the centers of both beads, which corresponds perfectly to their diameter.

4.1.2. Cell measurements

After testing the resolution capability of the setup on fluorescent beads, more complex structures should be investigated. In order to avoid aberrations due to a refrac-

tive index mismatch, the sample has to be embedded in a medium with a refractive index close to oil. This allows only imaging of fixed cells.
Adult human mesenchymal stem cells (**hMSCs**) offer an interesting field of research for biology and medicine due to their ability to differentiate into different spezialized cell types. A factor that determines the cell type in which stem cell differentiate is the elasticity of the surrounding tissue. Studies of stem cells grown on collagen-coated acrylamide gels and glass showed that cells on soft gels develop into neurons, cells on gels with a mediocre stiffness become myoblasts, and cells on a comparatively rigid gel differentiate into osteoblasts [53, 54]. During this spezialization the acto-myosin network of the cell is reorganized [55]. Changes in the morphology of the cells and the alignment of the acto-myosin stress fibers occur within the first 24 hours and allow to make statements on the final cell type. Therefore the acto-myosin stress fibers have been analyzed utilizing fluorescence microscopy [54, 56] and X-rays [55].
IsoSTED microscopy offers the possibility to investigate the three-dimensional stress fiber orientation with isotropic resolution and is thus a powerful tool to better understand stem cell differentiation. The hMSCs are provided by the group of Florian Rehfeldt from the Third Institute of Physics - Biophysics of the University of Göttingen. The cells are fixed using -20 °C cold methanol. Afterwards the sample is incubated with a primary antibody (*monoclonal Anti-β-Actin produced in mouse, A5441, Merck, Darmstadt, Germany*) that specifically binds to the actin filaments, followed by a secondary antibody (*STAR635P goat anti-mouse IgG, Abberior, Göttingen, Germany*) that binds to the primary antibody and holds the fluorescent dye molecules. Thereafter the sample is washed in PBS and embedded in a 97 % TDE solution following a dilution series in accordance to [57] in order to prevent changes in the cellular structure by osmotic shock. The sample is covered with a second cover glass, sealed using a two component silicone glue (*picodent twinsil® 22, Picodent, Wipperfürth, Germany*) and mounted into the microscope.
A drawback of antibody staining is that the measured structure size is increased due to the non-negligible size of the antibodies. For example, the diameter of microtubules in mouse 3T3 cells decorated with antibodies is approximately 60 nm, while unlabeled microtubules have a diameter of 25 nm [58]. This 60 nm diameter was confirmed by STED-4Pi microscopy measurements [44] and 4Pi-SMS imaging [59].
Figure 4.3 shows a three-dimensional representation of an isoSTED recording of a hMSC. The size of the stack is 40 µm x 30 µm x 2.5 µm and it is recorded with 40 nm x 40 nm x 40 nm voxel size and a voxel dwell time of 5 µs. The used laser powers are P_{Exc} = 0.33 µW, P_{STEDxy} = 8.6 mW and P_{STEDz} = 1.1 mW in the back-focal plane of each objective lens. The z-axis is color coded using the color bar shown. Features within the cell that are close to the cover glass e.g. below the nucleus

appear in green, while structures on top of the nucleus are depicted in yellow. The isotropic resolution within the whole data stack is 100 nm. This is comparable with the expected size of the stress fiber bundles. Compared to the previously shown isoSTED measurements [15, 16], the field of view in our microscope is increased by a factor of approximately five in x- and y-direction.

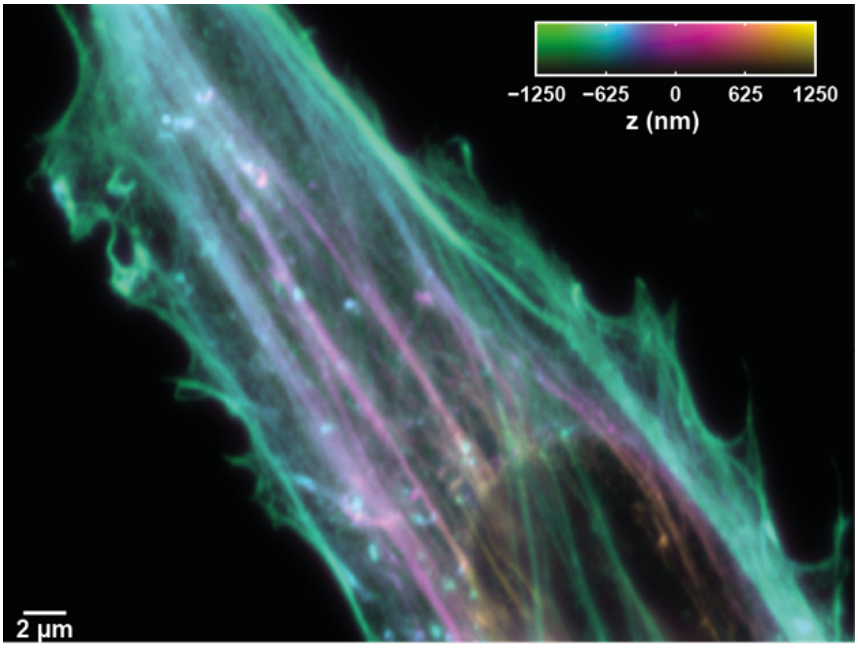

Figure 4.3.: Three-dimensional representation of a recording of the actin stress fibers in a human stem cell. Signal from regions close to the cover glass, e.g. below the nucleus, are visualized in green, while filaments on top of the cell are depicted in yellow.

Fluorescence microscopy of fixed cells has proven to be a versatile tool to understand protein organization in cells. The fixation changes the morphology of the cells and so-called fixation artifacts occur. Moreover, the quality of the cellular ultrastructure is not apparent [60]. In order to investigate cells in their most natural state, live cell imaging is necessary. Therefore the isoSTED setup was modified according to chapter 3.2.

4.2. IsoSTED microscopy utilizing water-immersion objective lenses

Measurements on fixed cells allow conclusions on the structure and organization of cells at the time of fixation. In order to get information about temporal changes, different samples have to be fixed and analyzed at different points in time. Thus temporal information of the cell before and after the fixation are lost. Another disadvantage is that the structure of cells changes due to the fixation, which can lead to misinterpretation.

Live cell microscopy offers the possibility to investigate single cells over a prolonged period of time and to visualize changes directly. Therefore, isoSTED microscopy of living cells is a promising method to better understand biological processes in cells. Living cells must be embedded in an aqueous cell culture medium. Its refractive index is similar to the refractive index of water.

Due to the 4Pi arrangement, the combination of both objective lenses focuses through the entire sample. The so far used oil-immersion objective lenses are designed to compensate for aberrations that occur when focusing into high refractive index media ($n_{\mathrm{medium}} \approx n_{\mathrm{oil}}$) through a cover glass with a thickness of 170 µm. Spherical aberrations that occur at the transition from the cover glass to the cell culture medium are not compensated. However, water immersion objective lenses are designed to compensate for these, which is why they were used in the following. Nevertheless, imaging with water immersion objective lenses is more prone to aberrations due to the relatively large refractive index steps at the immersion medium-glass and the glass-embedding medium interface [5, 6]. Furthermore, a slight tilt of the cover glass with respect to the focal plane introduces coma [61]. Therefore, special care has to be taken during sample preparation to minimize aberrations.

The used water immersion objectives have a correction ring to correct for spherical aberrations caused by different cover glass thicknesses. It allows to pre-compensate spherical aberrations for cover glass thicknesses of 130 - 210 µm. Because of the mounting of the movable objective lens it is not possible to reach its correction ring while it is mounted into the setup. Therefore it is important to use the same cover glass thickness for all measurements. Since the cover glasses are produced with a certain tolerance, their thickness has to be determined by using a micrometer screw. Only cover glasses with a thickness of 154 - 155 µm are used in the following as the correction ring of the movable objective lens is set to correct for aberrations at this thickness.

Besides the experimental difficulties, focusing light with the water-immersion objectives results in an increased spatial extent of the focal spots. Compared to the

previously used oil-immersion objective lenses this decreases the maximum intensity in the focal spot when the laser power entering the objective lenses is kept constant. The central y-z-section $(x = 0, y, z)$ through the simulated 4Pi excitation PSFs ($\lambda_{exc} = 640$ nm) for oil-immersion objective lenses (NA = 1.49, $n = 1.518$) and water-immersion objective lenses (NA = 1.2, $n = 1.333$) are shown in figure 4.4**a** **& b**, respectively. The increased spatial extent of the excitation pattern for water-immersion objectives is clearly visible.

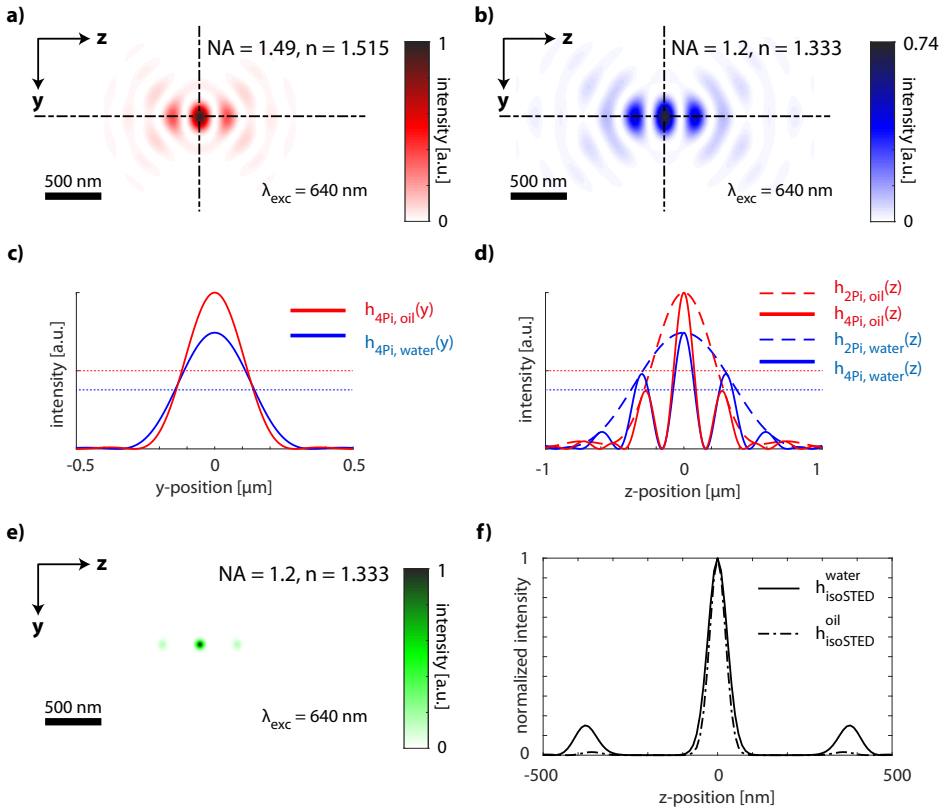

Figure 4.4.: Comparison of the simulated PSFs of the isoSTED microscope for oil- and water-immersion objective lenses: Central y-z-section through the 4Pi excitation PSF for **(a)** oil- and **(b)** water-immersion objective lenses. Lowering the NA of the objective lenses increases the spatial extent of the PSF and decreases the maximum intensity when the incident laser power is constant. Line profiles along the **(c)** y-axis and **(d)** z-axis illustrate this even more and show that the relative height of the primary side lobes is increased when water-immersion objective lenses are used. **(e)** In the central y-z-section through the isoSTED PSF for water-immersion objective lenses the primary side lobes are not fully suppressed, which is also visible in the **(f)** line profile along the z-axis.

In figure 4.4**c** the line profiles through the center of these PSFs along the y-axis and in figure 4.4**d** along the z-axis are presented. The profiles for the oil-immersion objective lenses are depicted in red and profiles for the water-immersion objective lenses in blue. Dotted lines in red and blue indicate the 50 % intensity line for the respective PSF. The broadening of the PSFs for the water-immersion lenses is even more evident in the line profiles in z-direction (fig. 4.4**d**). The line profiles for the 4Pi illumination PSFs are shown as lines, while dashed lines show the line profiles

through the illumination PSF of a single objective lens. The relative height of the primary side lobes for water-immersion objectives is larger than for oil-immersion objectives. Furthermore, the z-position of the side lobes is shifted away from the focal point ($x = y = z = 0$). The wavelength of light propagating in a medium is given by

$$\lambda = \lambda_0/n, \tag{4.1}$$

with λ_0 being the vacuum wavelength and n the refractive index of the medium. Since $n_{water} < n_{oil}$, the wavelength in water is longer than in oil and thus the distance between the interference maxima is larger, too.
The enlarged focal spot size and the decreased maximum intensity reduce the resolution of the isoSTED setup when water-immersion objective lenses are used. As the lateral resolution of a STED microscope is proportional to NA^{-2} the change in resolution can be estimated to be:

$$\Delta r_{water}/\Delta r_{oil} = \frac{1.49^2}{1.2^2} \approx 1.54. \tag{4.2}$$

Thus, at the same STED laser power a resolution of $1.54 \cdot 30$ nm $\approx$ 46.2 nm is expected in a STED microscope utilizing water-immersion objective lenses.
Figure 4.4**e** shows the central y-z-section ($x = 0, y, z$) through a simulated isoSTED PSF calculated for water-immersion objectives, an excitation wavelength of $\lambda_{exc} =$ 640 nm, fluorescence emission at $\lambda_{em} = 680$ nm and a STED wavelength of $\lambda_{STED} =$ 775 nm. The saturation factors for the inhibition are $\zeta_{xy} = 20$ and $\zeta_z = 2$ in lateral and axial direction and the pinhole diameter is set to 0.84 airy units. The side lobes of the 4Pi illumination PSF are not fully suppressed and thus residual side lobes are visible. The line profile through the center of the isoSTED PSF along the z-axis is shown as black line in figure 4.4**f**. Furthermore, a dashed line shows the line profile through the isoSTED PSF calculated for oil-immersion lenses. The other simulation parameters are as before. When using oil-immersion objective lenses, no side lobes can be seen at saturation factors of $\zeta_{xy} = 20$ and $\zeta_z = 2$, however, they become visible when water-immersion objective lenses are used.
In this section the resolution of the isoSTED microscope utilizing water-immersion objective lenses on samples containing fluorescent beads is determined. Afterwards, fixed cells are investigated, a method to improve the quality of the measured data sets is discussed and subsequently applied for measuring living cells.

4.2.1. Resolution

For the determination of the resolution capability of the isoSTED microscope utilizing water-immersion lenses, samples containing crimson fluorescent beads with a

diameter of 48 nm (*customized, LifeTechnologies™ now Thermo Fisher Scientfic, Waltham, MA, USA*), embedded in purified water are analyzed. The beads are attached to a cover glass and thus all beads are located in the same plane. The sample is covered with a second cover glass, sealed using a two component silicone glue and mounted into the microscope. Three-dimensional data stacks are recorded with an isotropic voxel size of 15 nm and setting the voxel dwell time to 100 µs. The applied laser powers are P_{Exc} = 1.4 µW, P_{STEDxy} = 36.2 mW and P_{STEDz} = 1 mW in the back-focal plane of each objective lens, and are optimized to achieve the highest possible resolution while still collecting a reasonable signal. As the bead layer is thin, the beads are in focus when the detected signal is maximal.

In order to determine the resolution in the recorded data measurements of 28 beads are analyzed statistically. For each bead recording the evaluated area is limited to a region of interest (**ROI**) of laterally 600 nm x 600 nm around the bead. As before, the center of the bead (x_0, y_0, z_0) is the pixel with the maximum signal count. The central x-y-section is the x-y-section through the center of the bead (x, y, z_0). To evaluate the bead data in the lateral direction, the signal count of its central x-y-section and the two neighboring x-y-sections in the data stack is summed up pixel wise. This gives a summed up x-y-image of the bead. Afterwards, in this image, averaged line profiles are dragged through the center of the bead in x- and y-direction. For the determination of the axial resolution the signal count of the central x-z-section (x, y_0, z) and its two neighboring x-z-sections is added up pixel wise and an averaged line profile through the center of the bead is dragged. The averaged line profiles are fitted with Gaussian functions to calculate the apparent FWHMs in the image. In order to ensure stable fitting, the averaged line profiles are interpolated twofold by spline interpolation.

Figure 4.5 shows the results from the evaluation of the recorded beads: In figure 4.5**a** an example of the summed up x-y-image of a single bead is presented. The summed up x-z-image of this bead is shown in figure 4.5**b**. The dashed white boxes indicate the orientation as well as the averaging used for the averaged line profiles in lateral direction and axial direction, which are presented in figure 4.5**c** **&** **d**, respectively. The size of the beads in the recordings is determined by the FWHM of the Gaussian fit and is 55.9 nm in x-direction and 53.7 nm in z-direction. Note, that the residual side lobes in the averaged line profile in z-direction in figure 4.5**d** are almost absent. This is due to the high STED powers applied in this measurement.

In figure 4.5**c** box plots illustrate the distribution of the bead sizes determined on the 28 beads. The central red mark on each box indicates the median of the FHWM in the respective direction, the bottom and top edges of the blue box indicate the 25th and 75th percentiles, respectively and the whiskers extend to the most extreme FWHMs. The median bead size is $FWHM_x = (55.9 \pm 1.5)$ nm,

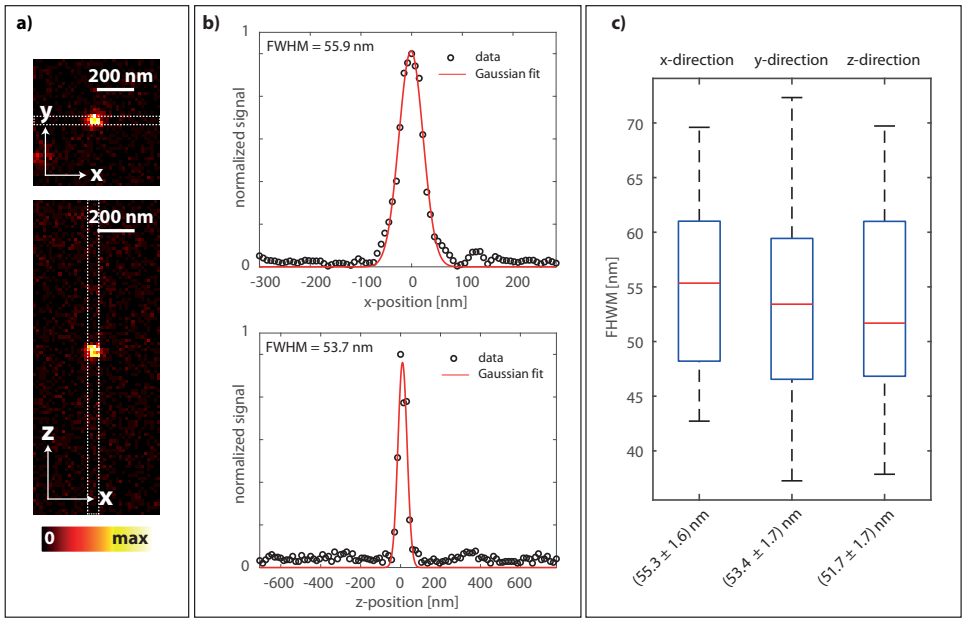

Figure 4.5.: IsoSTED measurement on 48 nm-diameter crimson fluorescent beads: **(a)** X-y-section and x-z-section through the center of a single bead. Dashed white boxes indicate the direction and averaging for the line profiles in **(b)**. Fitting a Gaussian function to the profiles gives a bead size of laterally 55.9 nm and axially 53.7 nm. **(c)** Box plots of distribution of the calculated FWHMs of 28 beads in x-, y- and z-direction. Red marks indicate the median FWHM in the respective direction. The resolution of the isoSTED microscope is better than 56 nm in all directions.

$\mathrm{FWHM_y} = (55.0 \pm 1.6)$ nm and $\mathrm{FWHM_z} = (54.7 \pm 2.3)$ nm in x-, y- and z-direction. As those values are close to the actual bead size of 48 nm we conclude, that the resolution of the isoSTED microscope utilizing water-immersion objective lenses is better than 56 nm in all directions.

4.2.2. Cell measurements

Fluorescent beads are the optimum sample to test the microscopes resolution under ideal conditions. They can be placed in a thin layer and embedded such that the refractive index is constant throughout the entire sample. Cell samples on the other hand are extended, three dimensional objects with e.g. different refractive indexes in the nucleus and the cytoplasm [62]. These refractive indexes also differ from that of the embedding medium and are therefore challenging for isoSTED microscopy.
In order to initially test the isoSTED microscope utilizing water-immersion lenses under such non-ideal conditions, fixed cell samples are investigated. In comparison to live cell imaging, fixed cells do not move during the measurement and do not need to be embedded in cell culture medium. Therefore it is possible to image larger field of views. Moreover, staining protocols for fixed cells are easier. A primary antibody that is recognized by several dye-labeled secondary antibodies is used to stain the protein of interest with a high molecular specificity and superior signal-to-noise ratio

due to the inherent signal amplification [63].

We decided to test the isoSTED microscope on the vimentin network in fixed neonatal human dermal fibroblasts (**HDFn**). Vimentin is an intermediate filament and part of the cytoskeleton. The thickness of a single filament is 10 nm [64]. It has been observed that the vimentin organization in human fibroblasts varies from short mesh-like, randomly oriented fragments to longer, linear bundles [65]. Moneron et al. [66] showed a lateral structure size of about 70 nm on fixed PtK2 cells stained with antibodies using STED microscopy.

For our measurements HDFn cells are seeded on cover glasses and incubated at 37 °C, 5 % carbon dioxide ($\mathbf{CO_2}$) in cell culture medium until the desired confluency is reached. Afterwards the cells are fixed by paraformalehyde incubation and stained following a standard protocol with a primary antibody (*V6389, Merck, Darmstadt, Germany*) at dilution of 1:200 and a secondary antibody (*STAR635P goat anti-mouse IgG, Abberior, Göttingen, Germany*) at dilution of 1:50. Thereafter the sample is embedded in *PBS*, sealed using a two component silicone glue and mounted into the microscope.

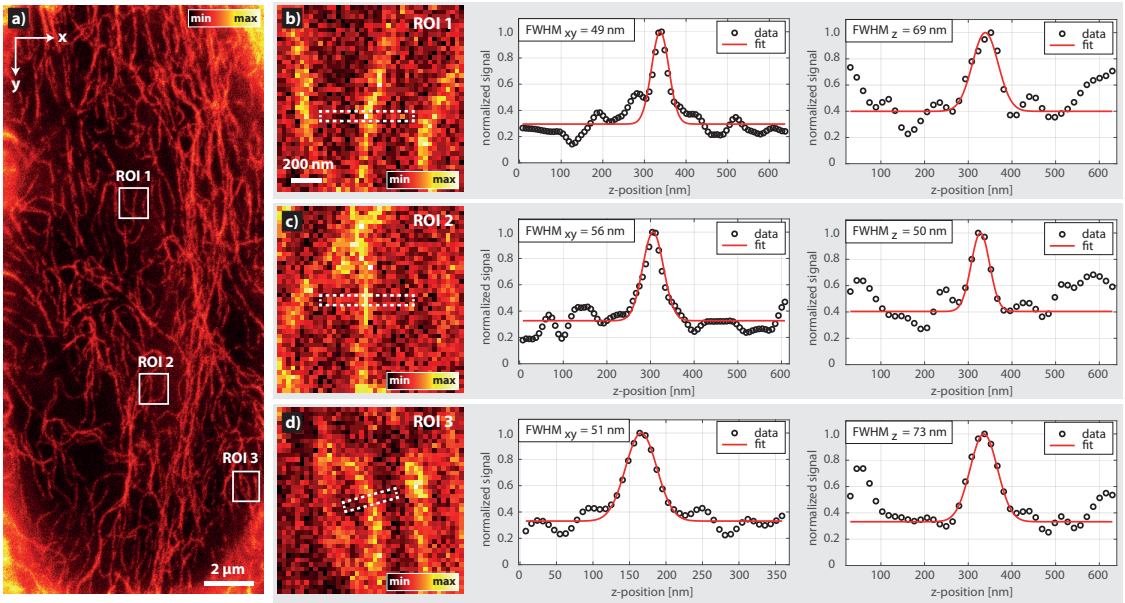

Figure 4.6.: IsoSTED measurement on the vimentin network in a fixed human fibroblast: **(a)** X-y-section below the nucleus. White boxes indicate three ROIs. **(b-d)** Zoomed views of the ROIs and lateral (along the white boxes) and axial (through the center of the filament) line profiles. Gaussian fits show a resolution of up to laterally 49 nm and axially 50 nm.

Figure 4.6**a** shows an x-y-section through the raw data of a recording of the vimentin network below the nucleus. The entire data set covers a volume of 10.44 µm x 23.64 µm x 5.01 µm (x, y, z) and is recorded with an voxel size of 30 nm in all directions and the voxel dwell time set to 20 µs. The applied laser powers are P_{Exc} = 1 µW, P_{STEDxy} = 23.1 mW and P_{STEDz} = 1.8 mW in the back-focal plane of each

objective lens. Three ROIs are marked with white boxes. A close up of these ROIs is presented on the left hand side of the panels in figure 4.6**b-d**. Dashed white boxes in each ROI show the orientation as well as the averaging used for the averaged lateral line profiles illustrated in the central graphs of the panels in 4.6**b-d**. Since the filaments are oriented arbitrarily in the x-y-section we do not distinguish between the resolution in x- and y-direction. A Gaussian fit of the averaged line profiles reveals a lateral FHWM of 49 nm, 56 nm and 51 nm for ROI1, ROI2 and ROI3, respectively, which is in the same order as the resolution determined on the bead measurements (cf section 4.2.1). In order to ensure stable fitting, the averaged line profiles are interpolated twofold by spline interpolation. The averaged line profiles in axial direction are determined as in the evaluation of the bead data and depicted in the rightmost graphs in the panels figures 4.6**b-d**. Besides the main peak they exhibit two additional regions with an increased signal at $z < 100$ nm and $z > 500$ nm. This signal most likely stems from the residual primary side lobes. Therefore, the Gaussian fit is limited to the central region of the profiles. As before the averaged line profiles are interpolated twofold. The axial FHWMs are 69 nm, 50 nm and 73 nm for ROI1, ROI2 and ROI3, respectively. Additionally to the lateral and axial line profiles their Gaussian fits are shown as red lines.

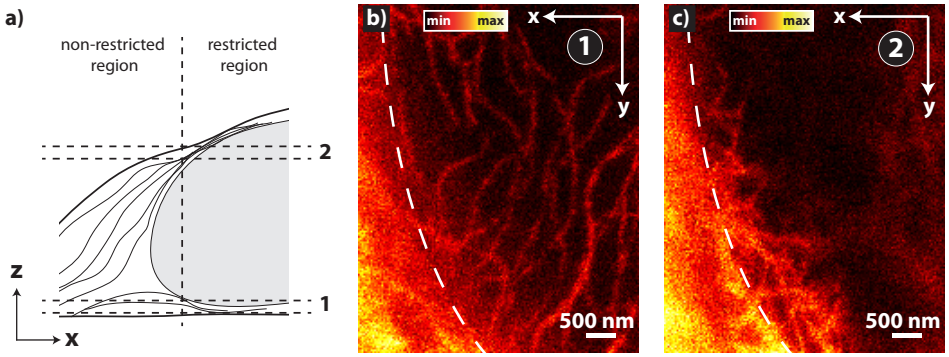

Figure 4.7.: Close-up of the isoSTED measurement on the vimentin network in a fixed human fibroblast: **(a)** Sketch of a cell with a filamental structure. Within the cytoplasmic region the filaments can form an arbitrary three-dimensional network that is limited to e.g. an almost two-dimensional structure in the physically restricted region below the nucleus. **(b)** Close up of the bottom left corner of the x-y-section depicted in 4.6**a**. **(c)** Image of the respective x-y-section 1.44 µm further in the sample. The blurred signal in the non-restricted region decreases the image quality.

A sketch of a cell and a filamental structure within the cell is shown in figure 4.7**a**. Two regions are visible: The non-restricted region, in which the filaments can form a three-dimensional network and a physically restricted region, in which the nuclear envelope and the cell membrane limit the axial extent of the vimentin network. Especially below the nucleus the vimentin is mostly arranged two dimensionally. The non-restricted regions are visible in the corners of the image in figure 4.6**a**. The signal in these regions is higher and the image appears less crisp. A close up of

the bottom left corner of the x-y-section presented in figure 4.6**a** is shown in figure 4.7**b** and the respective x-y-section 1.44 µm further in the sample is depicted in figure 4.7**c**. The approximate position of the nuclear envelope is shown by a dashed white line. The axial position in the cell for these x-y-sections is indicated by dashed lines **1** and **2** in figure 4.7**a**. In figure 4.7**b** the restricted area is below the nucleus where the network is arranged mostly two-dimensional, whereas in figure 4.7**c** the restricted area follows the curvature of the nuclear envelope. In this region the network is still arranged three-dimensionally. Therefore, only filaments within or slightly above or below the focal plane are visible. The region on the right-hand side of the image (fig. 4.7**c**) is inside the nucleus and thus no vimentin filaments are visible. The dim, broadened structures can be attributed to filaments above the nucleus and are generated by the residual side lobes of the isoSTED PSF.
Despite the difficult imaging conditions, the images of the vimentin network below the cell nucleus show a structure size of 50 nm, which corresponds to the resolution of the microscope. However, problems arise in regions where the structures under investigation are extended in the axial direction as contributions from planes above and below the focal plane deteriorate the image quality. The following chapter discusses these contributions and a possibility to increase the overall image quality is presented.

4.2.3. Improving the image quality

The change from oil- to water-immersion objectives to meet the requirements for live cell microscopy presents also some drawbacks: Beside the decrease in the maximum resolution achievable, due to the lower NA, with a water-immersion objective unwanted fluorescent signal from areas far away from the focal plane is detected. These out-of-focus contributions, their effects on the measurement data and a way to reduce this influence are described in the following.

Physical reason for the out-of-focus contributions

In order to explain the origin of the OOFCs in the data, we have to take a closer look at the image formation in isoSTED microscopy. The image is recorded by scanning the isoSTED PSF through the object which is mathematically described by a convolution:

$$\begin{aligned} I(\vec{r}) &= O(\vec{r}) * h_{isoSTED}(\vec{r}) \\ &= O(\vec{r}) * \left(h_{eff}^{isoSTED}(\vec{r}) \cdot h_{det,real}(\vec{r}) \right), \end{aligned} \tag{4.3}$$

with the effective isoSTED PSF, $h_{eff}^{isoSTED}(\vec{r})$, defining the regions from which fluorescence can still be emitted after the depletion. The detection PSF, $h_{det,real}(\vec{r})$, describes the probability to detect such a photon at position $\vec{r}$ (see chapter 2).
The depletion pattern in isoSTED microscopy is designed such that an isotropic depletion probability around the focal spot is generated. As the wavelengths for excitation and depletion are not identical, the distance between the maxima/minima of the respective patterns is not identical. Therefore, there are regions with low STED intensity, which are excited. Even if both wavelengths would be the same, such regions would exist since the lateral depletion pattern is generated by focusing a beam with an imprinted helical phase pattern, while the excitation pattern is formed by focusing a plane Gaussian beam.

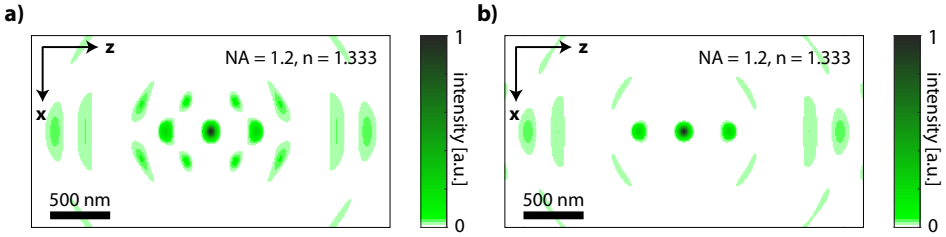

Figure 4.8.: Simulated effective isoSTED PSF in the case of water-immersion objective lenses: **(a)** Central x-z-section and **(b)** central y-z-slice through a simulated effective isoSTED PSF. The color table is adjusted to visualize low intensity regions of the PSF. Due to their comparatively large distance to the focal plane they are called out-of-focus contributions.

Figure 4.8**a & b** show the central x-z-section $(x, 0, z)$ and the central y-z-section $(0, y, z)$ through a simulated effective isoSTED PSF. The simulation parameters are: NA = 1.2, $n = 1.333$, $\lambda_{exc} = 640$ nm, $\lambda_{em} = 680$ nm, $\lambda_{STED} = 775$ nm, $\zeta_{xy} = 20$ and $\zeta_z = 2$. Note, that the colormap is different than in the figures before and is adjusted in order to visualize regions with lower intensity. It is clearly visible that regions exist, which can be neither attributed to the main peak nor to the residual side lobes of the isoSTED PSF. Therefore, a significant number of fluorescent photons is not only generated at the main peak and the residual side lobes, but also in regions further away from the focal plane. Because of their comparatively large distance from the focal plane these contributions are called out-of-focus contributions (**OOFCs**). Those OOFCs are even generated 1.5 µm away from the focal plane of the isoSTED microscope.
In order to visualize their influence on the image formation in isoSTED microscopy, we simulated the isoSTED PSF for oil-immersion objective lenses (NA = 1.49, $n = 1.515$) as well as for water-immersion objective lenses (NA = 1.2, $n = 1.333$) within a volume of 6.03 µm x 6.03 µm x 6.03 µm (x, y, z) and an isotropic voxel size of 30 nm. The wavelengths and saturation factors were chosen as before and setting the pinhole diameter was set to 0.84 airy units. Both PSFs are simulated for the

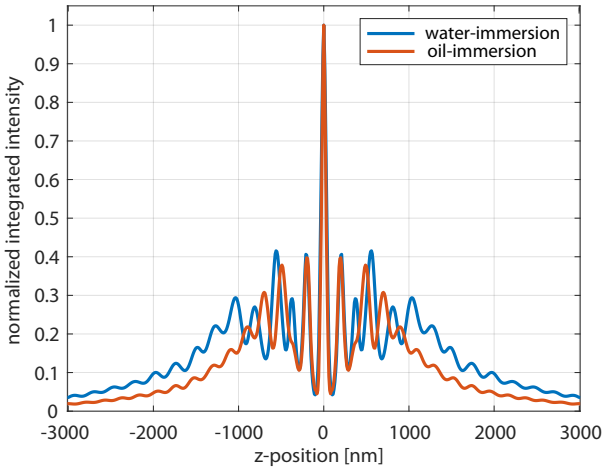

Figure 4.9.: Simulated isoSTED PSF for water- and oil-immersion objective lenses: Intensity of the PSF in the regions of the OOFCs is small, z-profiles, integrated over a lateral ROI of 6.03 µm x 6.03 µm, are used to show their influence on the measured data. For water-immersion objectives the contributions at ± 1 µm significantly increase.

same laser power. As the value of the effective isoSTED PSFs within the OOFCs is low, z-profiles integrated over the entire x-y-sections are used for their visualization (see fig. 4.9). The integrated z-profile for the oil-immersion objective lenses is presented in red and the integrated z-profile for the water-immersion objective lenses in blue. Both profiles oscillate strongly in the focal plane, but have values well above zero over the entire range. The profile for the water-immersion objective lenses is wider than that for the oil-immersion objective lenses and the individual peaks are shifted further away from the focal plane.
A significant increase in the OOFCs around ± 1 µm is visible in the profile for the water-immersion objectives.

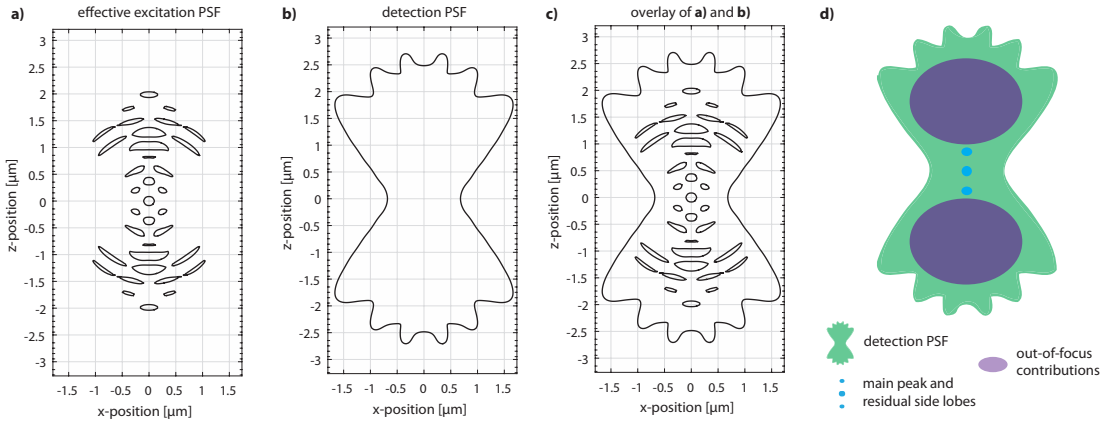

Figure 4.10.: Simulated effective isoSTED and detection PSF: **(a)** 1 % iso intensity lines of the effective isoSTED and **(b)** the detection PSF. **(c)** The entire effective excitation PSF is within the detection PSF and thus will contribute to the recorded signal. **(d)** Simplified representation of both PSFs.

Figure 4.10 shows the central x-z-section $(x, 0, z)$ through the focus of the isoSTED

microscope. The iso-intensity lines at 1 % of the maximum intensity of the effective isoSTED PSF and the iso-intensity lines at 1 % of the maximum intensity of the detection PSF within this x-z-section are shown in figure 4.10. Note, that due to the use of linearly polarized light the isoSTED PSF in the central y-z-section $(0, y, z)$ looks similar, but not exactly the same. For simplicity, without loss of generality only the x-z-section is considered. The overlay of the 1 % iso-intensity lines of the effective excitation and the detection PSF in figure 4.10**c** shows that all contributions of the effective isoSTED PSF that are larger than 1 % of its maximum intensity lie within the regions of the detection PSF that are detected with 1 % effectiveness and thus will contribute to the detected signal. A simplified representation of both PSFs is illustrated in figure 4.10**d**. The detection PSF is shown in green and effective isoSTED PSF is split into two parts: One that consists of the main peak and the residual side lobes (blue), and a second part that covers the OOFCs (purple). The resolution of the microscope is proportional to the spatial extent of h_{eff}, signal originating from the main peak ($\mathbf{S_{MP}}$), contains high resolution information, whereas detected out-of-focus signal ($\mathbf{S_{OOFC}}$) mostly consists of low resolution information. In order to quantify the isoSTED PSF a sample containing crimson fluorescent beads with a diameter of 200 nm (*F8806, Thermo Fisher Scientfic, Waltham, MA, USA*), embedded in purified water is analyzed. The beads are attached to a cover glass and thus all beads are located in the same plane. The sample is covered with a second cover glass, sealed using a two component silicone glue and mounted into the microscope. A 12 µm x 12 µm x 4 µm (x, y, z) data stack is recorded with an isotropic voxel size of 50 nm and setting the voxel dwell time to 40 µs. The applied laser powers are $P_{Exc} = 0.2$ µW, $P_{STEDxy} = 12.7$ mW and $P_{STEDz} = 1.3$ mW in the back-focal plane of each objective lens. In comparison to the 20 nm- or 40 nm-diameter beads used for determining the resolution of the microscope, the 200 nm-diameter beads are large and contain more dye molecules and thus allow a much better visualization of the low intensity S_{OOFC}.

Figure 4.11**a** shows the central x-y-section (x, y, z_0) through the recording. A close up of the central x-y-section through a single bead indicated by the white box is shown in figure 4.11**b**. The central x-z-section (x, y_o, z) through this bead in figure 4.11**c** & **d** with different color tables: While in figure 4.11**c** the color table is adjusted to visualize the entire signal range, it is modified in figure 4.11**d** to highlight the low intensity signal of the S_{OOFC}. The graph in figure 4.11**e** represents the averaged line profile in z-direction. It is determined as in the evaluation of the resolution on the bead recordings in section 4.2.1. This is equivalent to integrate the signal count of a lateral 3 pixel x 3 pixel ROI around the center of the bead for each x-y-section and plot it against the z-position. Due to the high signal from the main lobe and the residual side lobes no influence of S_{OOFC} is observed. When the

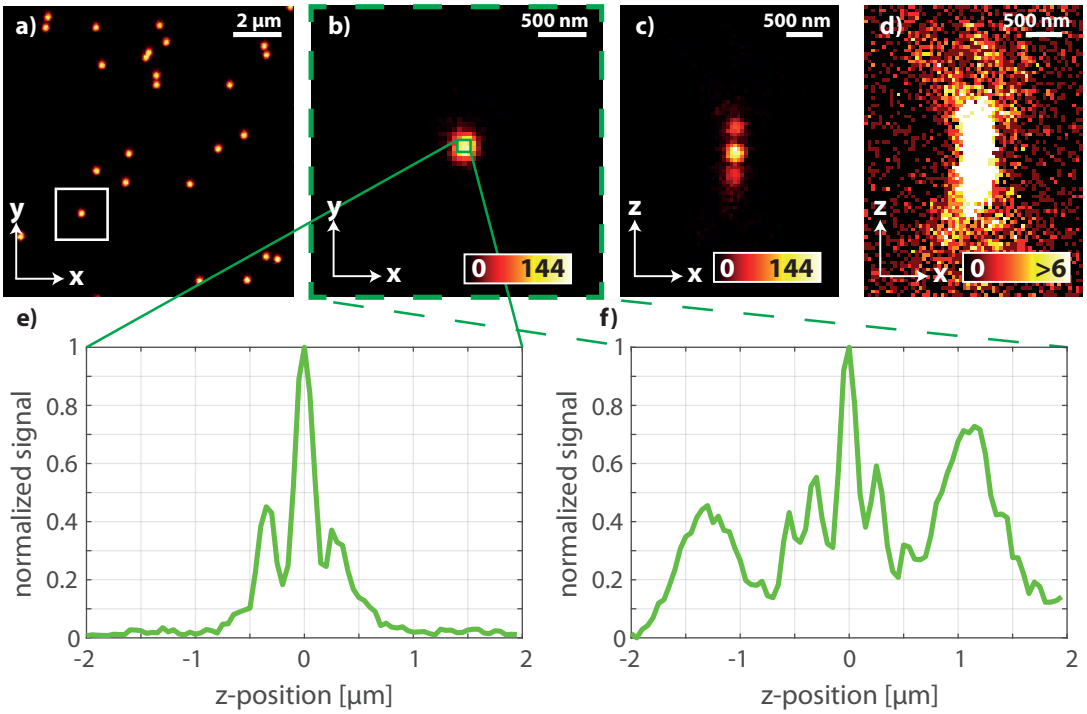

Figure 4.11.: IsoSTED measurement on 200 nm-diameter crimson fluorescent beads: **(a)** Central x-y-section through the entire data set. **(b)** Central x-y-section and **(c)** central x-z-section through a single bead indicated by the white box in **(a)**. Adapting the color table enables the visualization of the S_{OOFC} **(d)**. Z-profiles integrated over a **(e)** small lateral ROI of 150 nm x 150 nm and a **(f)** larger lateral ROI of 3 µm x 3 µm show the influence of the S_{OOFC}.

lateral integration area is increased to 3 µm x 3 µm (entire lateral size of the image in figure 4.11**b**) it is evident that the S_{OOFC} is not negligible (see fig. 4.11**f**).
The influence of the S_{OOFC} on the recorded image becomes more apparent when extended samples, e.g. cells, are measured. Figure 4.12 shows schematically two different situations that may arise while measuring filamentary structures in cells. In sparse regions, such as the periphery of the cell, only structures within the main peak will contribute to the detected signal. As the measurement proceeds and axially-extended regions are measured, structures in axially distant regions will contribute to the detected signal via OOFCs. Even though these structures are not in the focal plane, their signal lies within the detection volume and is thus assigned to the same pixel. Therefore the acquired image includes both: high-resolution information from the focal plane and low-resolution information from structures above and below the focal plane. In order to improve the image quality the S_{OOFC} must be removed. Three possible ways to address this issue will be discussed in the following.

Fourier-Filtering: The haze in the measurements stems from poorly resolved structures outside the focal plane. It is known from Fourier analysis that small, well resolved spatial structures have high spatial frequency components, whereas large

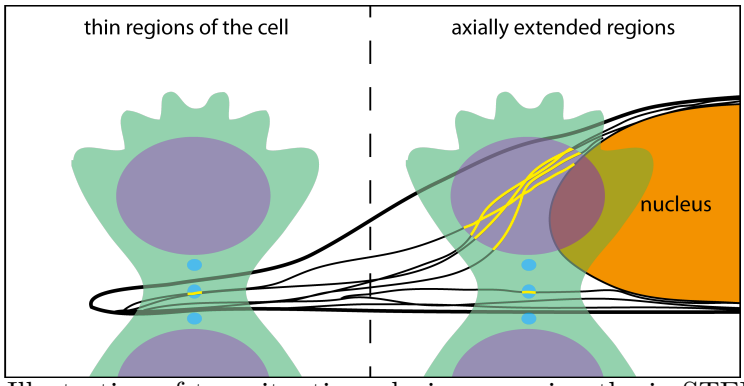

Figure 4.12.: Illustration of two situations during scanning the isoSTED PSF through a cell with fluorescently labeled filaments: In thin sample regions only structures within the main peak of $h_{eff}^{isoSTED}$ are effectively excited and contribute to the detected signal at the respective position. In thicker sample areas, the signal generated by the OOFCs adds to the total detected signal at each position.

structures mainly have low spatial frequency components. By means of a high-pass filter in the Fourier space, low frequency components can be filtered out of the image. The problem with this method, however, is that the high-pass filter does not differentiate between spatially extended and highly resolved, and poorly resolved fine structures. Therefore a priori information of the sample is required to perform proper filtering.

Deconvolution: If the PSF of the microscope is known, the object can be reconstructed by deconvolving the measured data with the PSF. In order to do this, the entire object must be scanned with the full extent of the PSF, which is often not practical. Many times only a part of the sample is of interest (e.g. filaments below the cell nucleus), or the data acquisition must be sped up (e.g. live cell imaging) and thus a reduction of the recorded volume is beneficial. If in these cases the axial scan range does not cover the full object, deconvolution is not possible.

Selective measurement of the S_{OOFC}: If it is possible to measure the S_{OOFC} separately, they can be removed from the data. This method would be independent of the sample and the extent of the imaged area.
Figure 4.13 shows one possible way to measure the S_{OOFC} separately. A second, laterally shifted, point-like detector is implemented into the setup. The detection PSF of this offset detection channel (**CH1**, red) is laterally shifted with respect to the main detection channel (**CH0**, green). If the displacement of the offset detector is chosen correctly both detection PSFs will only overlap in the regions of the OOFCs and thus, no signal from the main peak and the side lobes will be detected by the offset detector.
The previously shown measurement of a 200 nm-diameter fluorescent bead in fig-

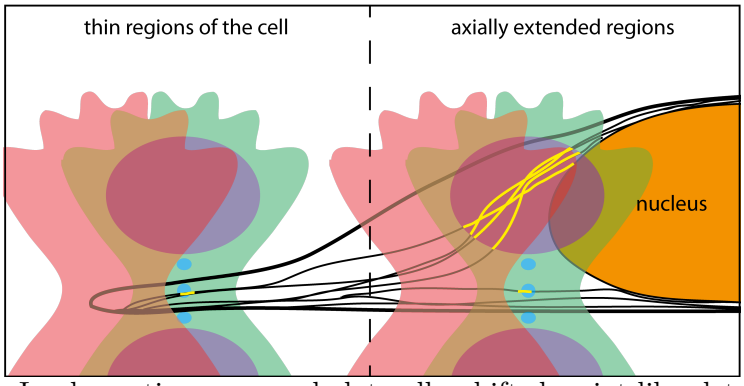

Figure 4.13.: Implementing a second, laterally shifted point-like detector, creates a second laterally shifted detection PSF in the sample. If the shift is chosen properly, this second detector only detects signal generated by the OOFCs.

ure 4.11 only showed the signal detected by the main detection channel. Figure 4.14**a** depicts the smoothed central x-z-section (x, y_o, z) through the bead recorded with CH0. Smoothing has been performed in order to better visualize the S_{OOFC}. The same x-z-section through the data set recorded simultaneously by an offset detection channel is shown in figure 4.14**b**. Note, that the color tables are adjusted in order to visualize the low intensity S_{OOFC}. Furthermore, the z-profiles integrated over a lateral ROI of 3 µm x 3 µm around the center of the bead for CH0 (green) and CH1 (red) are illustrated in figure 4.14**c**.

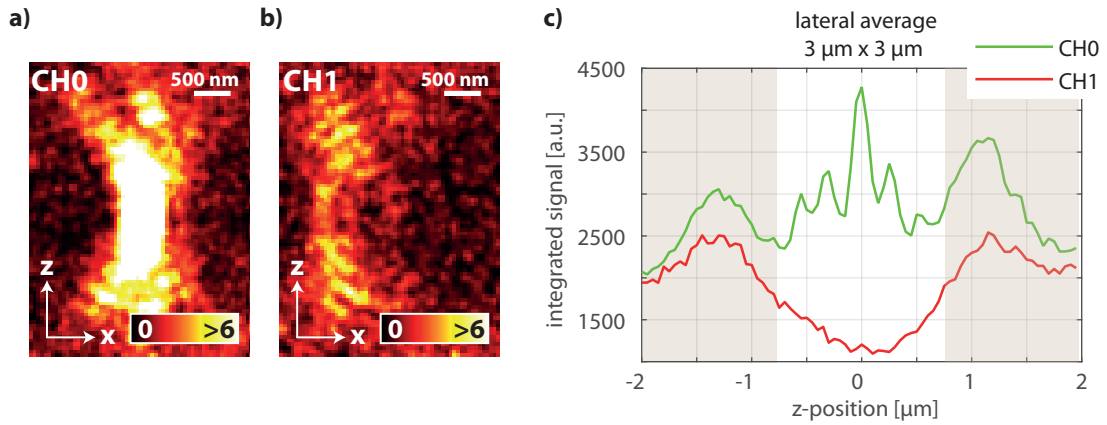

Figure 4.14.: IsoSTED measurement with one additional offset detection channel (CH1): **(a)** Smoothed central x-z-section through the bead depicted in 4.11**d** recorded by CH0. **(b)** The respective x-z-section of the bead recorded by CH1 shows that the S_{OOFC} is measured to the side the detector is shifted to. **(c)** Z-profiles of the signal detected with the CH0 and the CH1, integrated over a lateral ROI of 3 µm x 3 µm. The z-profile for CH1 exhibits a minimum in the focal plane and two maxima at the position of the S_{OOFC} in the z-profile of CH0. Therefore, by subtracting the scaled S_{OOFC} the image quality can be improved.

From figure 4.14 three conclusions can be drawn:

1. The z-profile of the offset detector exhibits a minimum in the focal plane and two maxima at the axial positions of the S_{OOFC} in the main channel. It can

therefore be used to improve the image quality.

2. The z-profile of the shifted detector does not perfectly represent the S_{OOFC} within the signal of the main detector. Therefore a simple subtraction of the signal detected with the offset channel from the signal detected with the main channel will not give the optimum result and thus a method to properly scale the detected S_{OOFC} must be derived.

3. The shifted detector rather measures the S_{OOFC} from the side it was shifted to. Signal contributions originating from the focal plane do not stem from the main peak but from respective peripheral areas. In order to measure the entire S_{OOFC} in an optimal way, several detectors will be needed which are grouped symmetrically around the main detector.

In order to better understand the detection with several offset detectors and their signal scaling, the next section presents a mathematical approach to the problem. This approach has been developed in cooperation with Dr. Frank Werner from the Statistical Inverse Problems in Biophyics Group at the Max Planck Institute for biophysical Chemistry. Subsequently, the experimental implementation and results are discussed.

Mathematical approach to the S_{OOFC}

As shown in figure 4.14**c** the signal collected by the main detector ($\mathbf{Y}$) consists of fluorescence stemming from the main peak and potential residual side lobes of the effective isoSTED PSF (S_{MP}) and the S_{OOFC}, that is

$$Y = S_{\mathrm{MP}} + S_{OOF}. \tag{4.4}$$

The shifted detectors measure a signal, Y_i, proportional to S_{OOFC}, with $i = 1 \dots N$ being the number of the i-th offset detector. All $\{Y, Y_1, \dots, Y_N\}$ are measured signals saved as three dimensional matrices with real entries ≥ 0. Assuming that the summation of all scaled Y_i gives the full S_{OOFC}, i.e.

$$\sum_{i=1}^{N} \mu_i Y_i = S_{\mathrm{OOFC}}, \tag{4.5}$$

equation 4.4 can be rearranged to derive S_{MP}. We obtain

$$\begin{aligned} S_{\mathrm{MP}} &= Y - S_{\mathrm{OOFC}} \ , \\ S_{\mathrm{MP}} &= Y - \sum_{i=1}^{N} \mu_i \cdot Y_i \ . \end{aligned} \tag{4.6}$$

If the shifted detectors do not collect signal from the center of the focus (fig. 4.14**b,c**) a summed up, scaled subtraction of the Y_i should remove their contribution without deterioration of the main-peak signal. We are therefore looking for the scaling factors μ_i that are optimal for the entire image and thus utilize the method of least squares to obtain a set of estimators $\hat{\mu}_i$ for μ_i that minimizes the norm

$$\hat{\vec{\mu}} = \underset{\vec{\mu}}{\operatorname{argmin}} \left\| Y - \sum_{i=1}^{N} \mu_i \cdot Y_i \right\|_2^2 . \tag{4.7}$$

Here $\hat{\vec{\mu}}$ and $\vec{\mu}$ are column vectors of $\hat{\mu}_i$ and μ_i respectively. Let B be a linear operator

$$B = (Y_1, \ldots, Y_N) ,$$

such that

$$B\vec{\mu} = \sum_{i=1}^{N} \mu_i Y_i .$$

Then equation 4.7 can be rewritten as

$$\hat{\vec{\mu}} = \underset{\vec{\mu}}{\operatorname{argmin}} \| Y - B\vec{\mu} \|_2^2 . \tag{4.8}$$

To determine $\hat{\vec{\mu}}$, this so-called minimization problem must be solved. This is done by calculating the extreme values of $\left\| Y - B\hat{\vec{\mu}} \right\|_2^2$, i.e. by computing the zeroes of the gradient

$$\nabla \left\| Y - B\hat{\vec{\mu}} \right\|_2^2 = 2(Y - B\hat{\vec{\mu}})^T(-B) \stackrel{!}{=} 0 . \tag{4.9}$$

Transforming this equation yields

$$2(Y - B\hat{\vec{\mu}})^T(-B) = -2Y^T B + 2\hat{\vec{\mu}}^T B^T B \stackrel{!}{=} 0 .$$

This can be rewritten as $B^T B\hat{\vec{\mu}} = B^T Y$, i.e.

$$\underbrace{\begin{pmatrix} \langle Y_1, Y_1 \rangle & \ldots & \langle Y_1, Y_N \rangle \\ \vdots & \ddots & \vdots \\ \langle Y_N, Y_1 \rangle & \ldots & \langle Y_N, Y_N \rangle \end{pmatrix}}_{A} \hat{\vec{\mu}} = B^T Y , \tag{4.10}$$

where A is a N x N matrix with $a_{ij} = \langle Y_i, Y_j \rangle$. To solve this equation for $\hat{\vec{\mu}}$, we assume that A is invertible. Then $\hat{\vec{\mu}}$ can be calculated by

$$\hat{\vec{\mu}} = A^{-1} B^T Y . \tag{4.11}$$

The S_{MP} calculated with this $\hat{\vec{\mu}}$ does not depend on S_{OOFC} and is thus linearly independent of all Y_i, i.e. the dot product of S_{MP} and any Y_i is zero:

$$\langle S_{\mathrm{MP}}, Y_i \rangle = \langle Y - B\hat{\vec{\mu}}, Y_i \rangle = 0 \ .$$

To verify that $\hat{\vec{\mu}}$ is the minimizer of equation 4.7, a proof by contradiction is performed. Suppose there exists an Y_i with

$$\langle S_{\mathrm{MP}}, Y_i \rangle = \langle Y - B\hat{\vec{\mu}}, Y_i \rangle \neq 0$$

for some $i \in \{1, \ldots, N\}$. We define $\hat{\vec{z}}$ as

$$\hat{\vec{z}} = \hat{\vec{\mu}} + \alpha \vec{e_i} \ ,$$

with e_i being the i-th unit vector, i.e. $B\vec{e_i} = Y_i$, and α is defined as

$$\alpha = \frac{\langle Y - B\hat{\vec{\mu}}, Y_i \rangle}{\|Y_i\|_2^2} \ .$$

Then

$$\begin{aligned} \left\| Y - B\hat{\vec{z}} \right\|_2^2 &= \left\| Y - B\hat{\vec{\mu}} - \alpha B\vec{e_i} \right\|_2^2 \\ &= \left\| Y - B\hat{\vec{\mu}} \right\|_2^2 - 2\alpha \underbrace{\langle Y - B\hat{\vec{\mu}}, Y_i \rangle}_{\alpha \|Y_i\|_2^2} + \alpha^2 \|Y_i\|_2^2 \\ &= \left\| Y - B\hat{\vec{\mu}} \right\|_2^2 - \alpha^2 \|Y_i\|_2^2 \\ &< \left\| Y - B\hat{\vec{\mu}} \right\|_2^2 \ , \end{aligned} \tag{4.12}$$

where $Y_i \neq 0$ and $\alpha \neq 0$ is used for the last step. This is a contradiction to $\hat{\vec{\mu}}$ being the minimizer of equation 4.7.

If we apply equation 4.11 to the data shown in figure 4.14**a & b**, we get a $\hat{\mu}$ of 0.578. Consequently, we can calculate a corrected signal by subtracting the correspondingly rescaled signal of the offset detection channels from the signal recorded by the main channel. In the following $\tilde{\mathrm{S}}_{\mathrm{OOFC}}$ and $\tilde{\mathrm{S}}_{\mathrm{MP}}$ denote data derived from recorded signals which are ideally the same as $\mathrm{S}_{\mathrm{OOFC}}$ and S_{MP}. Since no negative intensities are allowed all negative values in the corrected image are set to zero.

Figure 4.15**a** shows the z-profiles, integrated over a lateral ROI of 3 µm x 3 µm around the center of the bead, for the data recorded by (green), the $\tilde{\mathrm{S}}_{\mathrm{OOFC}}$ (red) as well as the accordingly corrected data, $\tilde{\mathrm{S}}_{\mathrm{MP}}$ (blue). It can be clearly seen that the signal in the regions of the $\mathrm{S}_{\mathrm{OOFC}}$ in the main channel is reduced in the corrected data. Furthermore, the z-profile of the corrected data is also lower in the focal

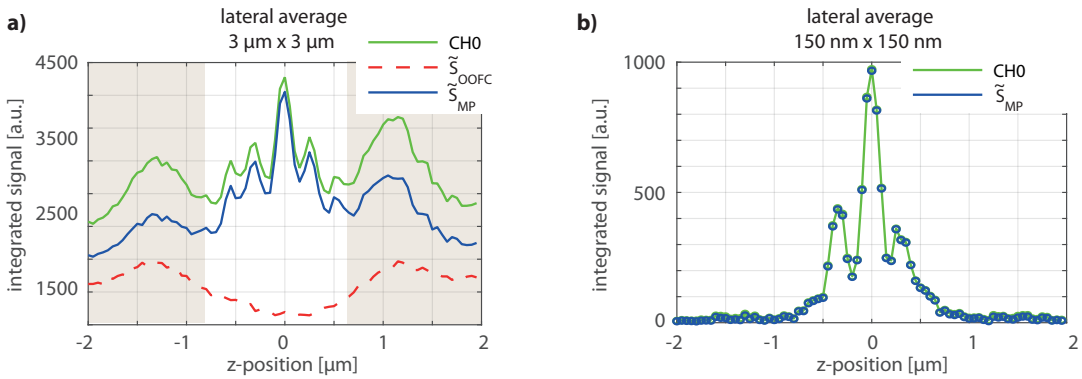

Figure 4.15.: IsoSTED measurement on a 200 nm crimson fluorescent bead with one additional offset detection channel (CH1): **(a)** Integrated z-profiles through a bead (cf figure 4.14). It can be clearly seen that the signal in the regions of the S_{OOFC} in the main channel (green) is reduced in the corrected data (blue). **(b)** The z-profiles through the center of the bead (lateral ROI of 150 nm x 150 nm) show, that no information is lost due to the subtraction of the $\tilde{S}_{OOFC}$.

plane ($z = 0$) as compared to the z-profile of the uncorrected data due to the large integration area. As mentioned earlier, this is because the offset channel contains not only S_{OOFC} but also signal from peripheral areas in the focal plane which is also subtracted in the corrected image. However, the z-profiles of the uncorrected and corrected data do not differ when the integration area is reduced from 3 µm x 3 µµm to 150 nm x 150 nm (see fig. 4.15**b**). Which means that the signal originating from the structure i.e. the bead is preserved.

Experimental implementation and results

As already mentioned in section 4.2.3, several shifted detectors, arranged symmetrically around the main channel, are necessary to detect the complete OOFCs in an optimal way. Since the resolution capability as well as the detected signal strength meet our expectations, the changes to the setup should be minimal.
We therefore decided to replace the previously used detection fiber with a customized 1-to-7 fan-out fiber (*Thorlabs, Newton, NJ, USA*) and thus integrate several shifted detection channels in the immediate vicinity of the main detection channel.
The 1-to-7 fan-out fiber consists of seven single fibers at one end, which are joined in a common end and arranged so that six fibers are positioned hexagonally around a central fiber. An image of the common end of the fiber recorded with a CCD camera (*GS3-U3-28S5M-C, Point Grey, Richmond, British Columbia, Canada*) attached to an upright microscope (*ZEISS Axioskop, ZEISS, Oberkochen, Germany*) and using a 50x objective lens (*Epiplan-NeoFluar, 50x/0.75, ZEISS, Oberkochen, Germany*) is shown in figure 4.16**a**. The fiber core for the main detection channel (CH0) is marked in green. Even though each of the seven individual fiber cores

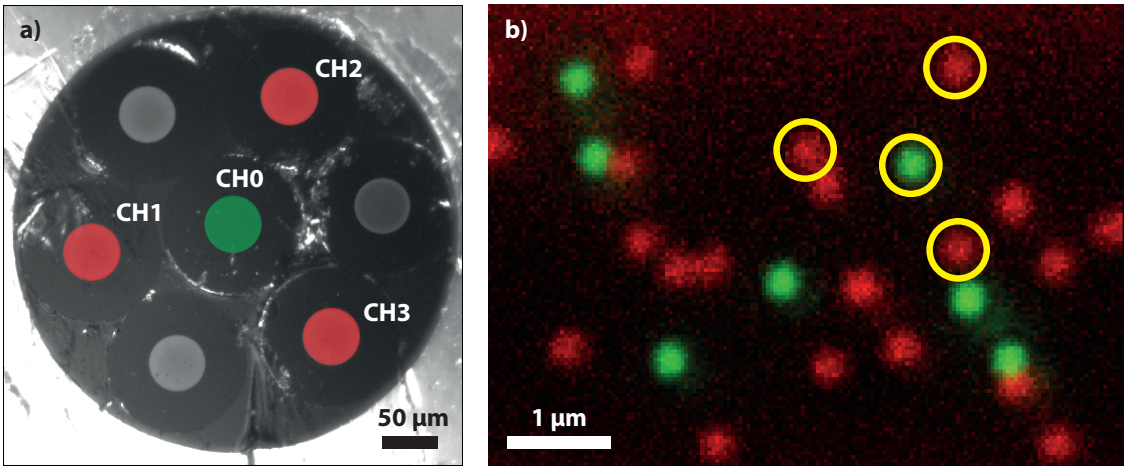

Figure 4.16.: Experimental realization of the offset detection channels: **(a)** Microscope image of the common end of the 1-to-7 fan-out fiber used for the detection. Six laterally shifted fibers are arranged hexagonally around the main detection fiber (CH0). Only three offset fibers are used as offset detection channels CH1, CH2 and CH3. **(b)** Reflection measurements on gold beads show the position of the detection channels in the focal plane.

could be used as a distinct detection channel, only three offset detection channels (CH1, CH2, CH3) can be utilized in addition to the central fiber core (CH0), since the measurement program only allows to use four channels at a time. The fiber cores used as offset channels in the further measurements are highlighted in red.

In order to illustrate the position of the individual detection channels in the focal plane, light was successively sent backwards through the individual ends of the fibers to illuminate a sample containing gold nano-particles, whose reflected light was recorded with a photo-multiplier tube (**PMT**). The superposition of these measurements is depicted in figure 4.16**b**. Analog to figure 4.16**a**, the signal belonging to the main detection channel is shown in green and the signals belonging to the offset detection channels in red. Yellow circles indicate the same bead, recorded with the respective detection channel.

Even though only three of the six offset detection channels can be used they are sufficient to reconstruct the S_{OOFC}. The data set examined in figure 4.11 & 4.14 was actually measured with three offset detection channels. Figure 4.17**a** shows the smoothed central x-z-section (x, y_0, z) through the bead already presented in figure 4.14**a**. The dashed black line indicates the position of the x-y-section through the maximal out-of-focus contributions in the main channel (position of the maximum OOFCs in the z-profile in figure 4.14**c**). This plane is axially distant enough from the focal plane to measure only signals originating from the OOFCs. The x-y-sections through this plane recorded with CH0, CH1, CH2 and CH3 are presented in figure 4.17**b**. Although each offset channel measures only a portion of the out-of-focus signal in the direction in which it is shifted to, the scaled and summed up x-y-section of all offset channels ($\tilde{S}_{OOFC}$) has a great similarity to the signal in

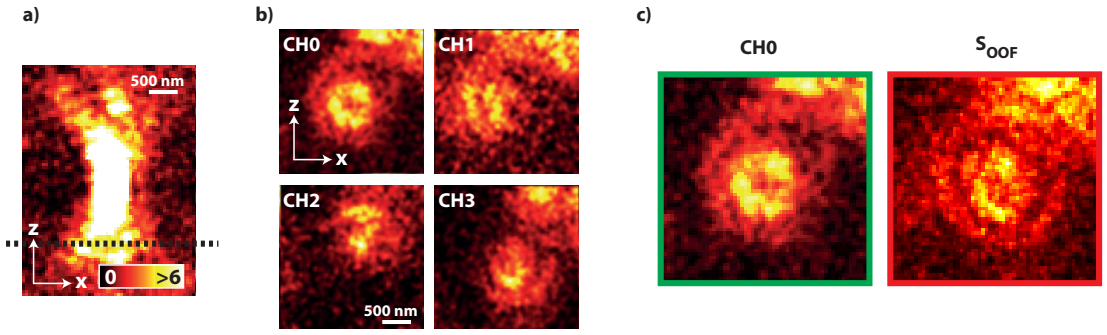

Figure 4.17.: IsoSTED measurement on a 200 nm crimson fluorescent bead with three additional offset detection channels (CH1, CH2, CH3): **(a)** Smoothed central x-z-section through a recording of a 200 nm crimson fluorescent bead (see fig. 4.14). A dashed black line indicates the plane of the maximum of the S_{OOFC} in the main detection channel. **(b)** X-y-sections through this plane recorded with CH0, CH1, CH2 and CH3. Even though the individual offset detectors only measure a part of the S_{OOFC}, they can be well reconstructed by scaling and summing up the signals of the offset detectors **(c)**.

the corresponding plane of the main channel (see fig. 4.17**c**). We therefore conclude that S_{OOFC} are sufficiently well mapped by the three offset detection channels used.

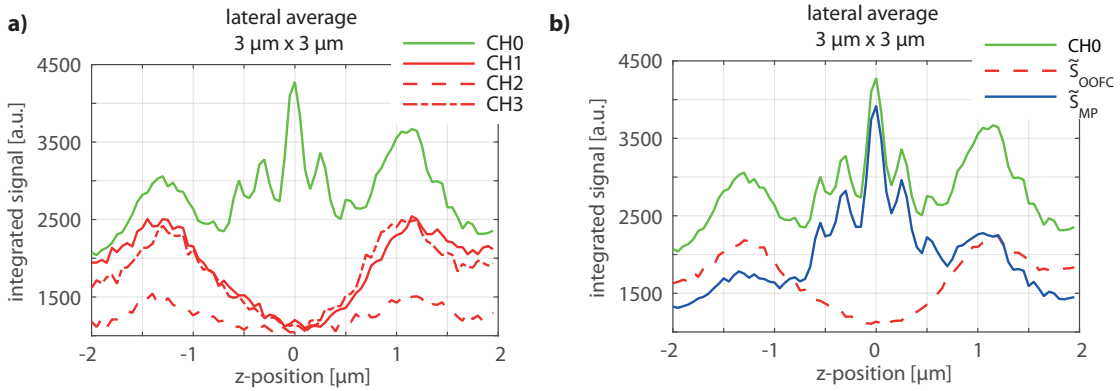

Figure 4.18.: IsoSTED measurement on a 200 nm crimson fluorescent bead with three additional offset detection channels (CH1, CH2, CH3): **(a)** Z-profiles, integrated over a lateral ROI of 3 µm x 3 µm, through the center of a bead (cf figure 4.17) acquired with CH0, CH1, CH2 and CH3, Each offset channel detects the maxima of the OOFC at the same position as CH0 and has a minimum intensity in the center and therefore can be used for correction of the data. **(b)** Subtracting the $\tilde{S}_{OOFC}$ from the signal count detected by CH0 reduces the OOFC in the $\tilde{S}_{MP}$ even further than for one offset detection channel (cf figure 4.15).

The z-profiles, integrated over a lateral ROI of 3 µm x 3 µm around the center of the bead for the data recorded with CH0 (green) and CH1, CH2, CH3 (red) are shown in figure 4.18**a**. The z-profiles corresponding to the offset detection channels exhibit a minimum in the focal plane and two maxima in the regions of the $\tilde{S}_{OOFC}$ in the z-profile of the main detection channel and can thus be used for correction. Nevertheless they differ in height. Different detection efficiencies of the individual fibers,

e.g. due to production-related differences in the fiber orientations, or residual aberrations in the setup that easily break the symmetry of the PSF are possible reasons for these discrepancies. For a proper correction of the data recorded with the main detection channel, the signal of each offset detection channel is then independently rescaled according to equation 4.11.

Besides the integrated z-profile of the signal detected by CH0 (green), figure 4.18**b** also shows the z-profiles of the $\tilde{S}_{OOFC}$ (red), as well as the $\tilde{S}_{MP}$ (blue). In z-profile of the corrected data it is apparent, that our correction method removes the S_{OOFC} from the uncorrected data substantially. A comparison with the z-profiles in figure 4.15**a** shows that correction with three shifted detection channels is more efficient than a correction with only one shifted detection channel.

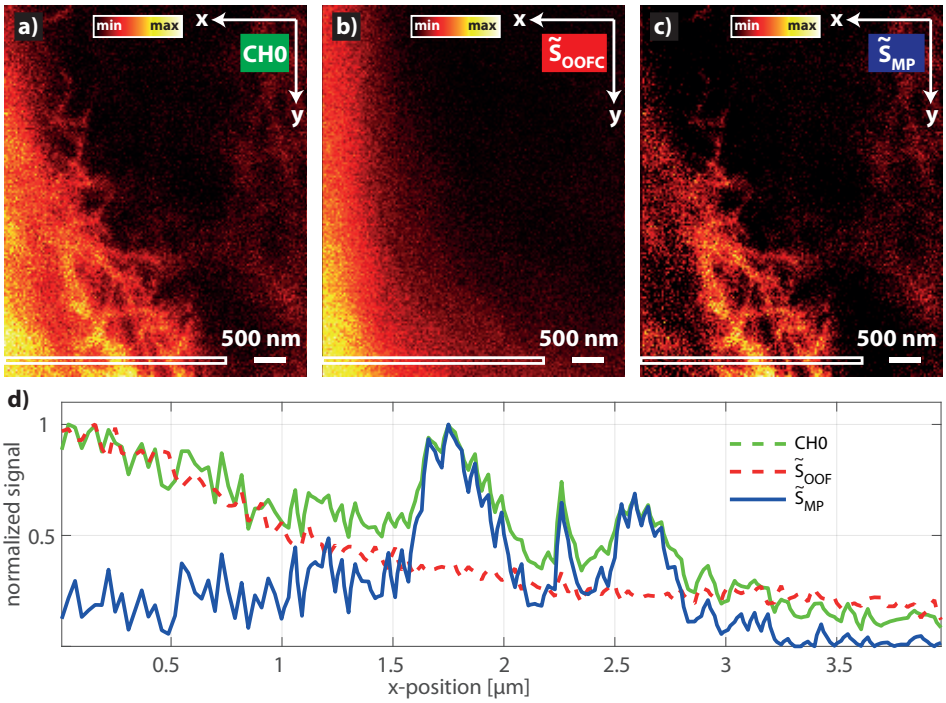

Figure 4.19.: Application of the OOFC-removal method on a recording of the vimentin network in a fixed human fibroblast.: **(a)** X-y-section in the perinuclear region of the cell (cf figure 4.7). **(b)** Respective x-y-section through the $\tilde{S}_{OOFC}$. The maximum S_{OOFC} is visible in the non-restricted region of the cell. **(c)** Respective x-y-section through the $\tilde{S}_{MP}$. The contrast in the image is increased. **(d)** After removing the $\tilde{S}_{OOFC}$, the gradient in the averaged line profile in x-direction is removed and only the signal from structures within the x-y-section is kept.

An example for applying this correction method to cell imaging is presented in figure 4.19. The color tables are set from minimum to maximum signal. Figure 4.19**a** shows the x-y-section already presented in figure 4.7**c**. As the maximum signal is dominated by the blurry S_{OOFC}, smaller structures appear dimmer and with less contrast to the background. The corresponding x-y-sections through the $\tilde{S}_{OOFC}$, and the corrected data ($\tilde{S}_{MP}$), are shown in figure 4.19**b** & **c**, respectively. Note,

that the $\tilde{S}_{OOFC}$ has its maximum in the non-restricted sample region next to the nucleus. Within the nucleus no $\tilde{S}_{OOFC}$ is detected, as there are no filaments in planes above and below the shown x-y-section. In the corrected data in figure 4.19**c**, the removal of the $\tilde{S}_{OOFC}$ improves the image quality substantially. The beforehand visible blurry signals in the bottom left corner are almost absent. After removing the $\tilde{S}_{OOFC}$ the highest signal count is in regions that contain filaments. Therefore, the visual contrast in the image is increased. The averaged line profiles in x-direction along the white boxes in figure 4.19**a-c** are presented in figure 4.19**d**. The profile of the main detection channel (green) shows a decreasing gradient along the x-direction. This gradient is also visible in the profile of the $\tilde{S}_{OOFC}$ (red) but is removed in the profile of the $c\tilde{S}_{MP}$ (blue).

OOFC-removal is a powerful tool to improve the image quality without a priori knowledge of the sample. The following section therefore focuses on isoSTED microscopy on living cells in combination with OOFC-removal.

5. IsoSTED microscopy for live cell imaging

Fluorescence microscopy of living cells poses challenges not encountered before. The limiting factor for super-resolution microscopy in living cells is the availability of suitable dyes. Most of the synthetic near-infrared fluorophores tend to be membrane impermeable and exhibit unspecific binding to cellular components [67]. As living cells do not tolerate a permanent disruption of their membranes antibody staining is not possible. Therefore, the fluorescent dyes must be membrane permeable in order to allow staining of intracellular structure while preserving the cell viability. Fluorescent probes based on silicon rhodamine (**SiR**), such as SiR-actin and SiR-tubulin can be used to stain the cytoskeleton in living cells [68–70]. By genetically modifying the cells using transfection it is possible to fluorescently label intracellular structures with far red fluorescent proteins such as TagRFP657 [71]. Furthermore, cells can be genetically modified in order to express SNAP-tagged or Halo-tagged proteins. Those cells can be labeled with a dye that binds to the respective tag [67, 72–74].
Despite these difficulties, imaging living cells in the near-infrared (**NIR**) regime has some advantages. In the so called NIR optical window of water (650 nm - 900 nm) the absorption coefficient of water is the lowest, which results in a larger penetration depth. This can for example be used for imaging thick tissues. Additionally, light scattering, autofluorescence in mammalian cells as well as the effect of phototoxicity is reduced at longer wavelengths [75, 76].
Another aspect to consider when imaging living cells is that living cells might change their cellular structure during the measurement. The rapidity and strength of these changes depends on the cell type, the environmental conditions and the structure of interest. In order to get a three-dimensional super-resolved data stack, the isoSTED PSF is scanned through the entire sample. When the acquisition time for an isoSTED data stack is too long, the data can be altered by the movement of the structures. An example for the movement of the microtubule network in a living HDFn cell during the acquisition of an isoSTED stack is presented in figure 5.1. In figure 5.1**a**, two axial neighboring x-y-sections (**1** and **2**) through the data set are shown. Both x-y-sections are separated by 30 nm in z and by approximately four seconds in time. The presented data is smoothed for a better visualization. Since the

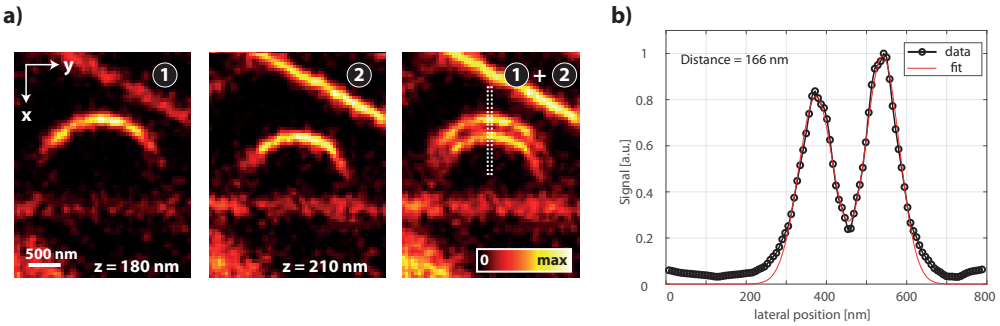

Figure 5.1.: Artifacts due to filament movements in an isoSTED measurement on microtubules in living HDFn cells: **(a)** Two axial neighboring x-y-sections through the recording (**1**,**2**) and the summation of both (**1**+**2**). The filament is in focus in **1** and **2**. A line profile **(b)** along the dashed lines in the sum of both x-y-sections **(1**+**2)** reveals that the filament moved laterally of about 166 nm in ≈ 4 s.

curved filament is in focus in both depicted planes, it must have moved during the measurement. This becomes even more apparent when both x-y-planes are added up (**1**+**2**): The filament position did change in axial as well as in lateral direction. By dragging a line profile along the dashed line in **1**+**2**, and fitting it with a double Gaussian function, we see that the filament position changed by 166 nm laterally within the ≈ 4 s (see fig. 5.1**b**). Note, that these profiles and all following profiles are interpolated twofold by spline interpolation in order to ensure a stable fitting.
In order to minimize those artifacts, it is beneficial to speed up the acquisition process. Therefore, the recorded volume is reduced by limiting the axial scan range to 600 nm (± 300 nm around the main peak of the isoSTED PSF). Furthermore, the voxel size is set to 30 nm in all directions for all subsequent cell measurements.

5.1. Microtubules

For testing the suitability of the isoSTED microscope for live cell imaging, we decided to image microtubules in HDFn cells. Microtubules are a part of the cytoskeleton in eukaryotic cells and are long, hollow cylindrical filaments made up of polymerized dimers of α- and β-tubulin. [77] The outer diameter of a microtubule is about 25 nm [58]. HDFn cells are seeded on cover glasses and incubated at 37 °C, 5 % CO_2 in cell culture medium until the desired confluency is reached. For staining, the cell culture medium is replaced with a staining solution (500 nmol SiR-tubulin in cell culture medium) and incubated at 37 ° C and 5 % CO_2 for four hours. SiR-tubulin (*SC002, tebu-bio, Offenbach, Germany*) is a cell memembrane permeable probe based on silicon rhodamine (SiR), that binds specifically to the microtubules. It features a far-red absorption and emission spectrum with maxima at λ_{abs} = 652 nm and λ_{em} = 674 nm and is suitable for live-cell STED microscopy [68–70]. Afterwards the staining medium is removed and replaced with ≈ 12 µl of $DMEM^{gfp}$-2 (*MC102,*

Evrogen, Moscow, Russia), an antibleaching live cell visualization medium. Then a second cover glass is placed on top of the sample and sealed using a two component silicone glue. Since the cells are embedded in a small volume of medium, they should be imaged as fast as possible as the limited supply of nutrients and CO_2 can quickly lead to cell degradation. According to our experience, no cell degradation is observed within the first two to three hours after sample preparation.

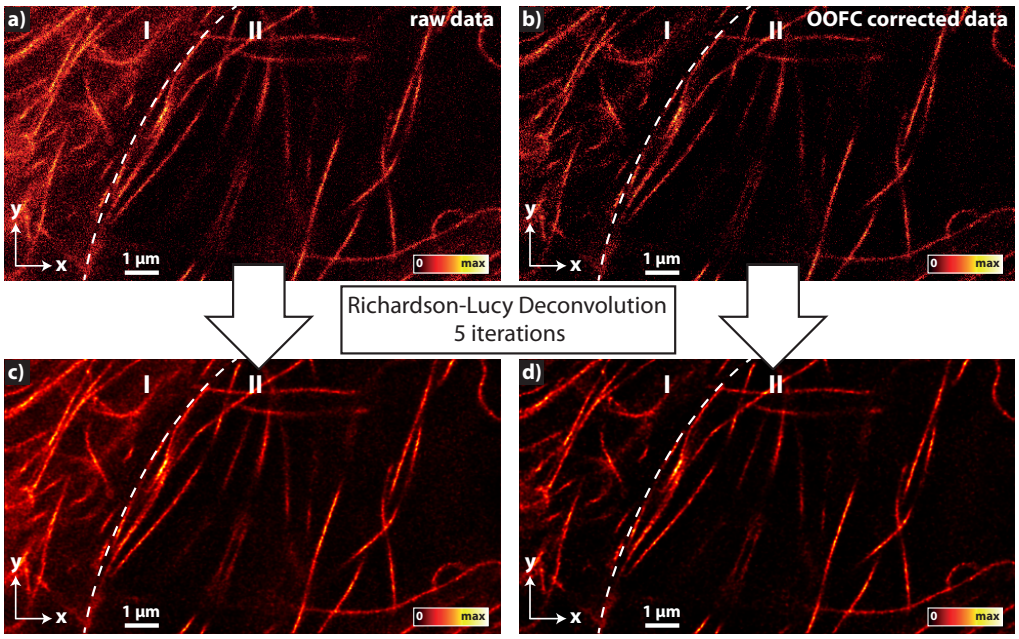

Figure 5.2.: Application of the OOFC-removal method to isoSTED imaging of living cells: **(a)** The x-y-section through the raw data of a recording of the microtubule network shows two regions: **I)** A blurry, physically non-restricted region where fluorescence is detected from the focal plane and the planes below and above the focal plane. **II)** A crisp region in which the filaments are physically restricted into a thin area by the cell nucleus and the plasma membrane. The position of the nuclear envelope is indicated by the dashed line. **(b)** The same x-y-section through the OOFC-removed data. The blur in region **I)** is drastically reduced. X-y-sections through the Richardson-Lucy deconvolved **(c)** raw data and **(d)** OOFC-removed data show that deconvolution with a simulated PSF improves the OOFC-removeed data even further.

An an x-y-section through such a recording of the microtubules is presented in figure 5.2. The size of the entire recorded stack is 14.55 µm x 8.04 µm x 0.6 µm (x, y, z). And the voxel dwell time set to 20 µs resulting in an acquisition time of about 57 s for the entire stack. The applied laser powers are $P_{Exc} = 2.4$ µW, $P_{STEDxy} = 9$ mW and $P_{STEDz} = 0.8$ mW in the back-focal plane of each objective lens.
In the image of the raw data in figure 5.2**a** two regions are visible: **I** Here the image quality is decreased due to the detection of signals from planes above and below the focal plane. The microtubule network in this regions is most likely arranged as an extended three-dimensional network as it is the case in the non-restricted regions described in section 4.2.2. **II** In this region the image quality is high, the microtubules look crisp and no blur in the image is visible. Here no signal contributions from

planes above and below the focal plane are observed. This is the case in physically restricted regions, as in regions below the nucleus where the microtubule network is an almost two-dimensional sample. Since, no microtubules are within the nucleus no signal from other planes than the focal plane can be detected. The dashed white line indicates the approximate position of the nuclear envelope.
The same x-y-section through the OOFC-removed data set is presented in figure 5.2**b**. The blurred signal contributions in region **I** are drastically reduced and thus the overall image quality is increased. By deconvolution, the image quality can be improved even further. The recorded data set is a convolution of the object and the PSF of the microscope and therefore, if the PSF of the imaging system is known, an estimate of the object can be derived by deconvolving the recorded data set with the PSF. In figure 5.2**c** & **d** the same x-y-sections through the raw data and the OOFC-removed data deconvolved with a simulated isoSTED PSF using a standard Richardson-Lucy (RL) deconvolution (5 iterations, regularization parameter 1e-10) are presented. The RL deconvolved raw data in figure 5.2**c** are already an improvement compared to the raw data, but still contain blurred contributions, especially in the non-restricted sample regions (**I**). These blurred contributions are almost absent in the OOFC-removed and RL deconvolved data shown in figure 5.2**d**. Standard deconvolution methods are based on signal conservation and require the sample to be scanned by the entire PSF, otherwise artifacts can be introduced in the deconvolved data set. In the presented data the axial scan range is limited to 600 nm, which is way smaller than the extent of the OOFC of the isoSTED PSF (cf. fig. 4.10). Therefore, removing the S_{OOFC} and applying the deconvolution subsequently yields a better estimate of the observed structure and thus a crisper image. In the following the data analysis is done on OOFC-removed data while the images show OOFC-removed and deconvolved data.
In order to determine the resolution of the isoSTED microscope in living cells, four samples are prepared, measured and analyzed. Since the staining efficiency is not the same for every sample, the applied laser powers and voxel dwell times are adjusted for each sample individually. For the determination of the lateral resolution averaged lateral line profiles in direction perpendicular to the filaments are analyzed. Filament movement can falsify the apparent structure size in the image and the averaged line profiles. Since the z-axis was chosen as the slow axis, this could particularly occur when the signal of neighboring z-planes is averaged. Hence, contrary to the analysis of the bead data no averaging in axial direction is done. The axial resolution is determined by analyzing integrated z-profiles through the center of the filaments. In total 100 lateral and axial line profiles are fitted with a Gaussian function, each fit is controlled manually, and only microtubules that are fitted properly in lateral and axial direction are used for further analysis. Thus the amount

of line profiles used is reduced to 59 in each direction. The results are presented in figure 5.3.

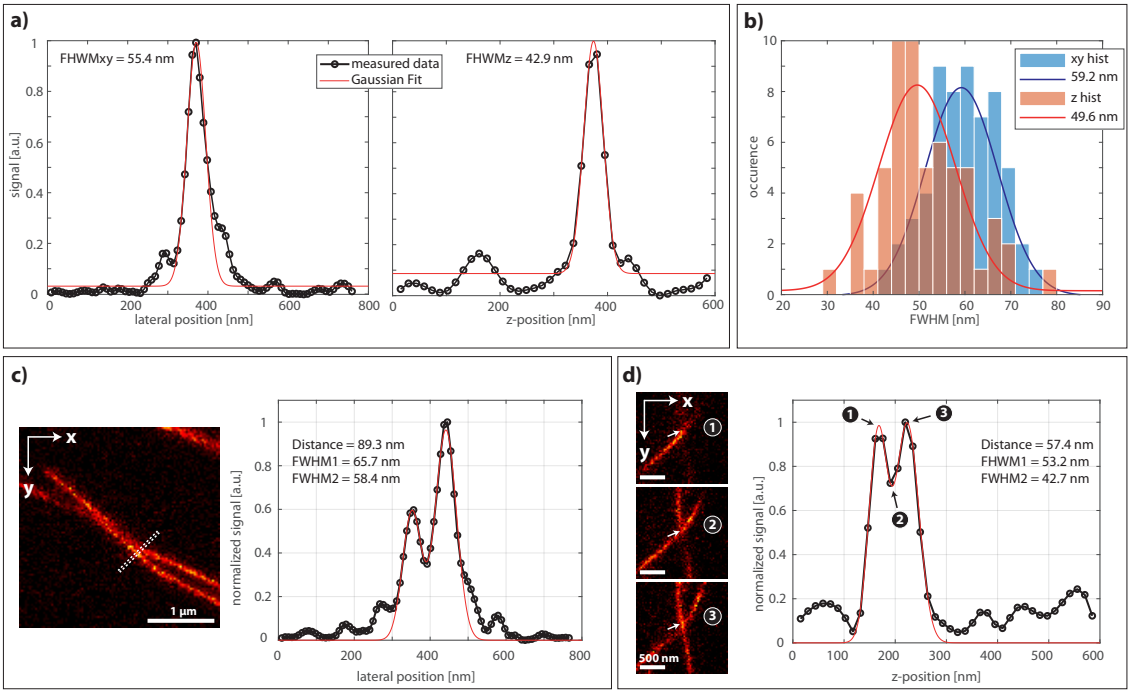

Figure 5.3.: IsoSTED measurement of microtubules in living HDFn cells: **(a)** Lateral and axial line profiles through a single microtubule depicted in the x-y-section. Gaussian fits show a lateral resolution of 55.4 nm and an axial resolution of 42.9 nm. **(b)** Histogram of the lateral and axial resolutions obtained by fitting Gaussian functions to 59 lateral and 59 axial line profiles. The average values are $\mathrm{FWHM_{xy}} = (59.2 \pm 1.0)$ nm and $\mathrm{FWHM_z} = (49.6 \pm 1.2)$ nm. **(c)** Filaments separated by 89.3 nm laterally and **(d)** 57.4 nm axially can be resolved.

An example of an averaged lateral line profile, an integrated z-profile through a microtubule as well as their respective Gaussian fits is presented in figure 5.3**a**. The lateral and axial size of the filament in the recording is determined by the FWHM of the Gaussian fit in the respective direction and is in this case $\mathrm{FWHM_{xy}} = 55.4$ nm and $\mathrm{FWHM_z} = 42.9$ nm.

The histograms of the FWHMs of the 59 filaments used for analysis are shown in figure 5.3**b**. Fitting a Gaussian function to the distributions of determined lateral and axial sizes results in an average size of the filaments of $\mathrm{FWHM_{xy}} = (59.2 \pm 1.0)$ nm and $\mathrm{FWHM_z} = (49.6 \pm 1.2)$ nm. The axial resolution is slightly better than the lateral resolution. This can be either due to movements of the filaments during the measurements, a slightly higher STED intensity in the axial direction or slight aberrations introduced by the refractive index difference between the embedding medium and the sample. As the diameter of the microtubules is known to be 25 nm, the determined structure size is a good indication for the resolution of the microscope. As a result it can be stated that the achievable resolution in living cells is in the same range as the resolution determined on bead measurements (cf section 4.2.1).

To show that structures that are close to each other can actually be resolved, microtubules that cross each other are analyzed. On the left hand side of figure 5.3**c** an x-y-section through a recording of the microtubule network, in which two single microtubules are crossing each other, is presented. The dashed white box indicates the orientation as well as the averaging region used for the averaged line profile illustrated on the right hand side of 5.3**c**. Fitting a double Gaussian (red) to the line profile reveals that the centers of the two microtubules with diameters of 65.7 nm and 58.4 nm are laterally separated by 89.3 nm.
An example for the axial resolution capability is shown in figure 5.3**d**. On the left hand side three axially adjacent x-y-sections (**1, 2, 3**) through a data set are depicted. The microtubule oriented in y-direction is lying above the diagonally oriented microtubule. On the right hand side the integrated z-profile through the pixel indicated by the white arrow is presented. A double Gaussian fit (red) of this profile results in an axial distance of 57.4 nm between the centers of both filaments which is in the same order as their axial extent (53.2 nm and 42.7 nm).
The data set presented in figure 5.3**c** is recorded with a voxel dwell time of 40 µs and applying laser powers of P_{Exc} = 1 µW, P_{STEDxy} = 11.2 mW and P_{STEDz} = 0.8 mW in the back-focal plane of each objective lens. And the data set shown in figure 5.3**d** is recorded with a voxel dwell time of 40 µs and laser powers of P_{Exc} = 2.4 µW, P_{STEDxy} = 9 mW and P_{STEDz} = 0.8 mW in the back-focal plane of each objective lens.

5.2. Time lapse imaging

With an isotropic resolution better than 60 nm isoSTED microscopy in living cells is a promising tool to investigate three-dimensional changes of intracellular structures. For this purpose samples several isoSTED stacks of the same sample are recorded consecutively.
The dynamics of the microtubule network can be well investigated with isoSTED microscopy as seen in figure 5.4. For the top view representation shown in figure 5.4 the iso-surfaces of three consecutive measurements are calculated in Matlab and presented in cyan for the first, in yellow for the second and in magenta for the third data stack. Already in this overview representation it is apparent that the microtubule network changes over time.
The displayed volume corresponds to 17.19 µm x 14.7 µm x 270 nm (x, y, z) of the entire recorded volume of 17.19 µm x 14.7 µm x 600 nm (x, y, z) and is recorded with a voxel dwell time of 40 µs resulting in an acquisition time of 264 s for one stack, corresponding to a base acquisition time of 1.7 $s\mu m^{-3}$. The applied laser powers are

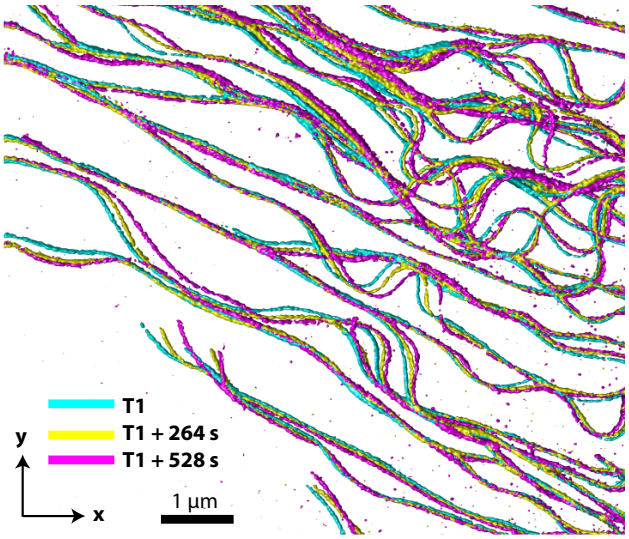

Figure 5.4.: IsoSTED time lapse imaging of microtubule network in a living HDFn cell. The iso-surfaces for the first data set are presented in cyan, for the second data set in yellow and in magenta for the third recording and presented in a top view.

P_{Exc} = 1 µW, P_{STEDxy} = 11.2 mW and P_{STEDz} = 0.8 mW in the back-focal plane of each objective lens.

Two further examples of microtubule dynamics are shown in figure 5.5. The depicted data is OOFC-removed and RL-deconvolved (5 iterations, regularization parameter 1e-10). In figure 5.5**a** an x-y-section through a recording at three different points in time (**T1**, **T2**, **T3**) is presented. The acquisition time for one stack is 57.4 s and therefore a plane recorded at T1 in the first stack is measured at T2 = T1 + 57.4 s in the second stack and T3 = T1 + 114.8 s in the third stack. This corresponds to a base acquisition time of 0.8 $s\mu m^{-3}$. The filament indicated by the white arrow in T1 retracts laterally in T2 and disappears in T3. As both effects, the retraction and the disappearance could also be attributed to an axial movement out of the depicted plane it has been ensured by investigating the planes above and below the imaged plane that this is not the case. Yellow arrows indicate a microtubule that is not visible in T1, but moves into the shown plane over time.
Another measurement is presented in figure 5.5**b**. Again, an x-y-section through the microtubule network is shown at three points in time. The temporal distance between consecutive x-y sections is 85.2 s, corresponding to a base acquisition time of 0.8 $s\mu m^{-3}$. As in figure 5.5**a**, yellow arrows indicate a microtubule that moves into the illustrated plane over time. The blue arrows point to a filament that moves laterally and axially. It is in the imaged plane in T1, slightly defocused in the second x-y-section (T2) and moves back into the observed plane in the third x-y-section (T3) and lastly pink arrows indicate a filament that moves laterally into the depicted x-y-section.

The data set presented in figure 5.5**a** is recorded applying laser powers of P_{Exc}

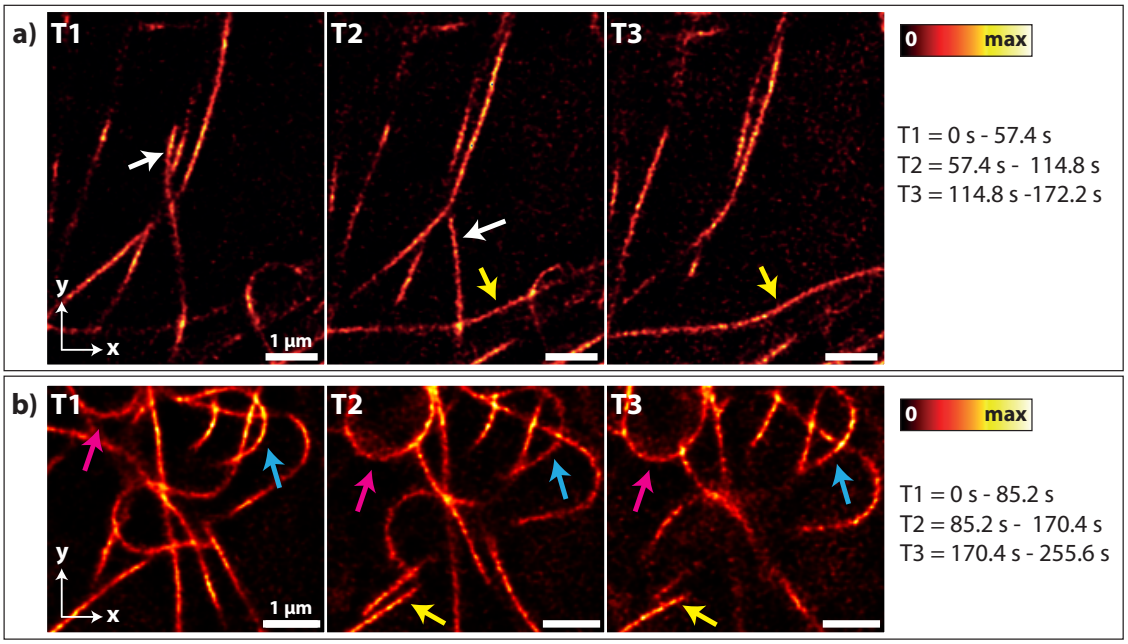

Figure 5.5.: Further examples for isoSTED time lapse imaging on microtubules in living HDFn cells.: X-y-sections through two different recording **(a & b)** at three different times (**T1**, **T2**, **T3**) show changes in the orientation of the microtubules. The filament indicated by white arrows retracts laterally out of the displayed region, filaments indicated by yellow arrows move into the z-plane. The blue arrows in **(b)** point to a filament that goes out of the observed plane and comes back into the observed plane and pink arrows indicate a filament that moves laterally into the displayed region.

= 2.4 µW, P_{STEDxy} = 9 mW and P_{STEDz} = 0.8 mW, and the data set shown in figure 5.5**b** with laser powers of P_{Exc} = 0.8 µW, P_{STEDxy} = 11.2 mW and P_{STEDz} = 0.8 mW in the back-focal plane of each objective lens, and setting the voxel dwell time to 20 µs in both measurements.

5.3. SNAP-tagged structures (vimentin)

We showed that SiR delivers great isoSTED perfomance in living cells. Moreover, it is possible to fabricate a membrane permeable derivative of SiR that binds to a SNAP-tag, which would allow virtually any protein to be labeled by this dye. In cooperation with Abberior (*Abberior, Göttingen, Germany*) such a SiR-SNAP substrate was produced. By transfection, cells can be genetically modified in order to express SNAP-tagged vimentin. Such a transfection can be either transient or stable. In a transient transfection the transfected genetic material is not integrated into the cell genome and thus exists in the cell only for a limited time. The efficiency of transient transfection varies between individual cells and therefore reproducibility is not guaranteed. However, in a stable transfection the introduced genetic material is incorporated in the genome of the cells and therefore to their progeny. Thus a stable and reproducible expression and hence reproduceable staining is possible. U-2 OS

cells of a knock-in cell line expressing SNAP-tagged vimentin [74] are provided to us by the group of Stefan Jakobs from the Max-Planck-Institute for biophysical Chemistry. The cells are seeded on cover glasses and incubated at 37 °C, 5 % CO_2 in cell culture medium until the desired confluency is reached. For staining, the cell culture medium is replaced with a staining solution (1 µmol SiR-SNAP in cell culture medium) and incubated at 37 ° C and 5 % CO_2 for four hours. Afterwards the staining medium is removed and replaced with DMEM^{gfp}-2. The second cover glass is placed on top of the sample and sealed using a two component silicone glue.

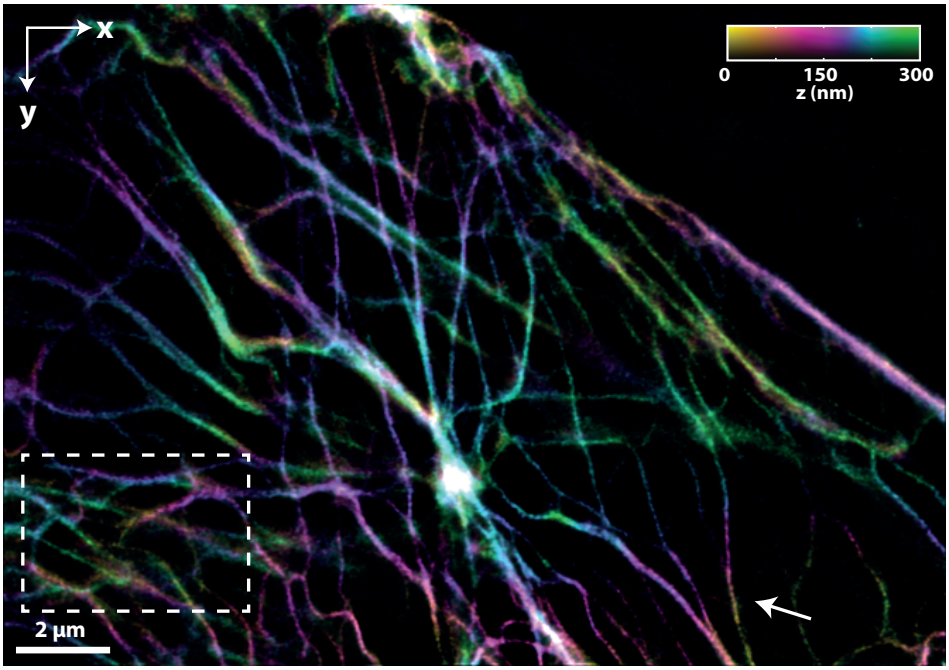

Figure 5.6.: Three-dimensional representation of a recording of the vimentin network in a living U-2 OS cell. The axial position is color coded using the color bar shown. A white box indicates mesh-like structures within the network, whereas the white arrow indicates a fiber bundle that runs through the entire data stack.

A three-dimensional representation of an isoSTED recording of the vimentin network of such a stained cell is presented in figure 5.6. The displayed volume corresponds to is 20.04 µm x 14.07 µm x 0.3 µm (x, y, z). The axial position is color coded using the color bar shown. The three-dimensional structure of the vimentin network is clearly visible. A white arrow indicates a vimentin filament that runs through the entire displayed axial range. Note, that the thickness of the filaments is not constant, but varies throughout the cell. As mentioned in section 4.2.2 the vimentin network varies from mesh-like randomly oriented structures to longer linear bundles [65]. A mesh-like region is indicated by the dashed white box and an example for a bundle is the filament indicated by the white arrow. The data set is recorded with a voxel size of 30 nm in all directions and a voxel dwell time of 40 µs. The applied laser powers

are $P_{Exc} = 3$ µW, $P_{STEDxy} = 12.6$ mW and $P_{STEDz} = 0.8$ mW in the back-focal plane of each objective lens.

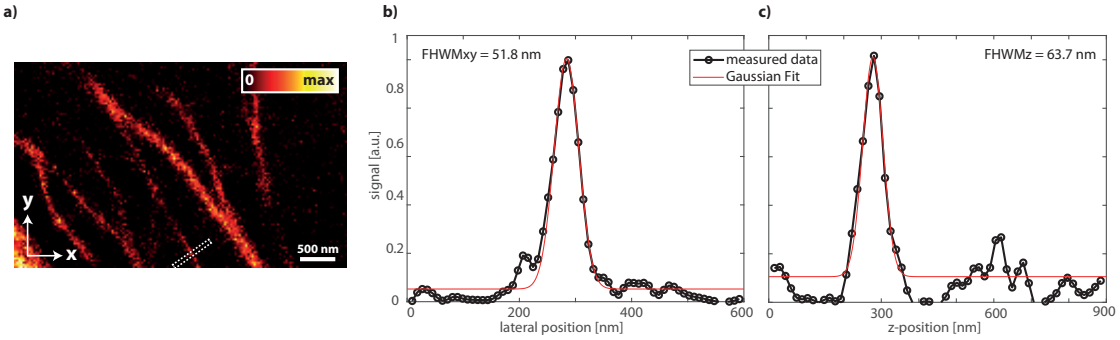

Figure 5.7.: IsoSTED measurement on the vimentin network in a living U-2 OS cell: **(a)** X-y-section through the data set shown in figure 5.6. The thickness of the filaments varies within the sample. Fitting a Gaussian function to the averaged line profile **(b)** and the integrated axial profile **(c)** reveals a lateral size of the filament of 51.8 nm and an axial size of 63.7 nm.

An x-y-section through the data set shown in figure 5.6 is presented in figure 5.7**a**. Due to the bundling of the vimentin the thickness of the individual filaments varies and thus a thin filament is analyzed in order to determine the resolution in the measurement. The dashed white box shows the orientation as well as the averaging used for the averaged line profile illustrated in figure 5.7**b**. Fitting a Gaussian function (red) reveals a lateral FWHM of the filament of 51.8 nm. The integrated axial profile through the center of the filament as well as the respective Gaussian fit (red) are shown in figure 5.7**c**. The axial extent of the filament is $FWHM_{xy} = 63.7$ nm. This is in the same range as the resolution determined in measurements on fluorescent beads (cf section 4.2.1), on microtubules in living cells (cf section 5.1) and on the vimentin network in fixed HDFn cells (cf section 4.2.2).

5.4. Towards physiological samples

Until now, all presented measurements have been performed on cells seeded on cover glasses. Under physiological conditions, e.g. in a tissue, cells are surrounded by the extracellular matrix that provides structural and biochemical support of the cells. Due to slight differences between the refractive index of the cell and the extracellular matrix aberrations can be introduced when cells are imaged under physiologial conditions. Nonetheless, the shape, structure and function of cells, especially of stem cells, is dependent on the properties of their surroundings (cf section 4.1.2). Aquaeous collagen-coated polyarcylamide (**PAA**) gels are used to mimic the elasticity of the extracellular matrix in vitro [53]. In order to demonstrate isoSTED imaging on more physiological conditions, samples on collagen-coated acrylamide

gels are examined in the following.
Adding an additional PAA layer poses, as already mentioned, some difficulties as the refractive index difference between the embedding medium and the PAA can give rise to aberrations. For a PAA gel with an elasticity of 30 kPa we measured a refractive index of $n_{\mathrm{PAA}} = 1.345$. Even though this is larger than the refractive index of the cell culture medium ($n_{\mathrm{medium}} = 1.333$), no aberrations in the PSF are directly apparent in measurements on fluorescent beads. However the resolution of the microscope might sill be slightly decreased.
In order to verify whether this is the case, samples containing crimson fluorescent beads with a diameter of 48 nm are measured and subsequently analyzed. A 30 µm thick collagen-coated PAA layer is placed onto our cover glasses by the group of Florian Rehfeldt from the Third Institute of Physics - Biophysics of the University of Göttingen. The bead suspension is diluted 1:5000 in purified water and placed on top of the PAA gel for 25 s. Afterwards, the supernatant is gently removed such that the PAA layer is not disrupted or stripped off. After adding 12 µl of purified water as embedding medium the sample is covered with a second cover glass and sealed using a two component silicone glue. Three-dimensional data stacks are recorded with a voxel size of 15 nm in all directions and a voxel dwell time of 20 µs. The applied laser powers are $\mathrm{P_{Exc}} = 0.5$ µW, $\mathrm{P_{STEDxy}} = 42.5$ mW and $\mathrm{P_{STEDz}} = 1.5$ mW in the back-focal plane of each objective lens.

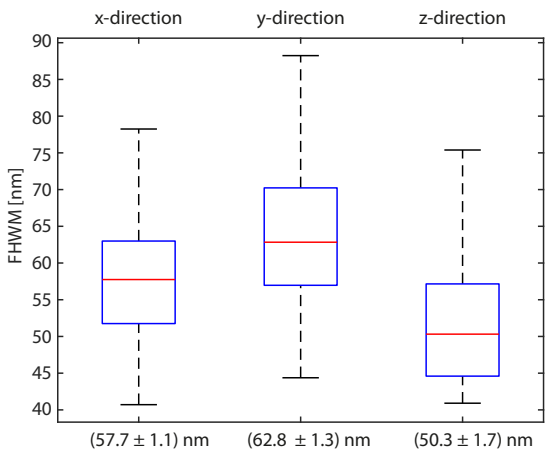

Figure 5.8.: Box plots of the calculated FHWMs of 55 crimson fluorescent beads on 30 µm thick layers of PAA gel with an elasticity of 30 kPa. The median bead size is $\mathrm{FWHM_x} = (57.6 \pm 1.1)$ nm, $\mathrm{FWHM_y} = (63.0 \pm 1.3)$ nm and $\mathrm{FWHM_z} = (52.7 \pm 1.1)$ nm and thus the resolution of the isoSTED microscope under such imaging conditions is better than 63 nm in all directions.

To identify the resolution in the recorded data sets, measurements on 55 beads are analyzed. The size of the beads in the recording is determined by the FWHM of a Gaussian function fitted to the averaged line profiles in x-, y- and z-direction through the center of the beads. In figure 5.8 box plots illustrate the distribuion

of the calculated FWHMs. The median bead size, indicated by the red mark in each box, is $FWHM_x = (57.6 \pm 1.1)$ nm, $FWHM_y = (63.0 \pm 1.3)$ nm and $FWHM_z = (52.7 \pm 1.1)$ nm. The bead size in the axial direction is slightly smaller than in the lateral direction. This could be due to a higher STED intensity in the axial direction compared to the lateral direction or slight aberrations introduced by the refractive index difference between the embedding medium and PAA layer. Nonetheless, the average measured beads' size is comparable to the measured beads' size determined in section 4.2.1. As those values are close to the actual bead size of 48 nm, we conclude that the resolution of the setup under these imaging conditions is better than 63 nm.

IsoSTED microscopy has been shown to be suitable for live cell imaging and an additional collagen-coated PAA layer only slighty lowers the resolution of the isoSTED microscope. Therefore we decided to perform isoSTED imaging on living human stem cells that are seeded on collagen-coated PAA gels. The hMSCs are provided and seeded on collagen-coated PAA gels with an elasticity of 11 kPa by the group of Florian Rehfeld. For staining, the cell culture medium is replaced with a staining solution (2 µmol SiR-actin (*SC001, tebu-bio, Offenbach, Germany*) in cell culture medium) and incubated at 37 ° C and 5 % CO_2 for 75 minutes. Afterwards the staining medium is removed and replaced with $DMEM^{gfp}$-2. The sample is covered with a second cover glass and sealed using a two component silicone glue. Three consecutive, three-dimensional data stacks are recorded with a voxel size of 30 nm in all directions and a voxel dwell time of 20 µs resulting in an acquisition time of 156 s for one stack. The applied laser powers are $P_{Exc} = 0.5$ µW, $P_{STEDxy} = 7.3$ mW and $P_{STEDz} = 0.8$ mW in the back-focal plane of each objective lens.

The results of such an isoSTED recording are presented in figure 5.9. An x-y-section through the recording is depicted in figure 5.9**a**. The dashed white box shows the orientation as well as the averaging region used for the line profile illustrated on the left hand side. Fitting a Gaussian function (red) reveals a lateral FWHM of the filament of 60 nm. On the right hand side, the integrated axial profile through the center of the filament as well as its Gaussian fit (red) are presented. The axial size of the filament is determined as $FWHM_{xy} = 39.8$ nm. The filament is thinner in the axial direction than in the lateral direction this can be either due to movement of the actin filament during the measurement, a non-symmetrical shape of the filament, a higher STED intensity in the axial direction or slight aberrations introduced by the refractive index difference between the embedding medium and the sample.

The actin network is a highly dynamic structure that changes it organization depending on its position and role within the cell. It can form branched and crosslinked networks e.g. at the cortex or the lamellipodia or fiber bundles in e.g. stress fibers or filopodia [78]. Depending on their function, the rapidity of the actin reorgani-

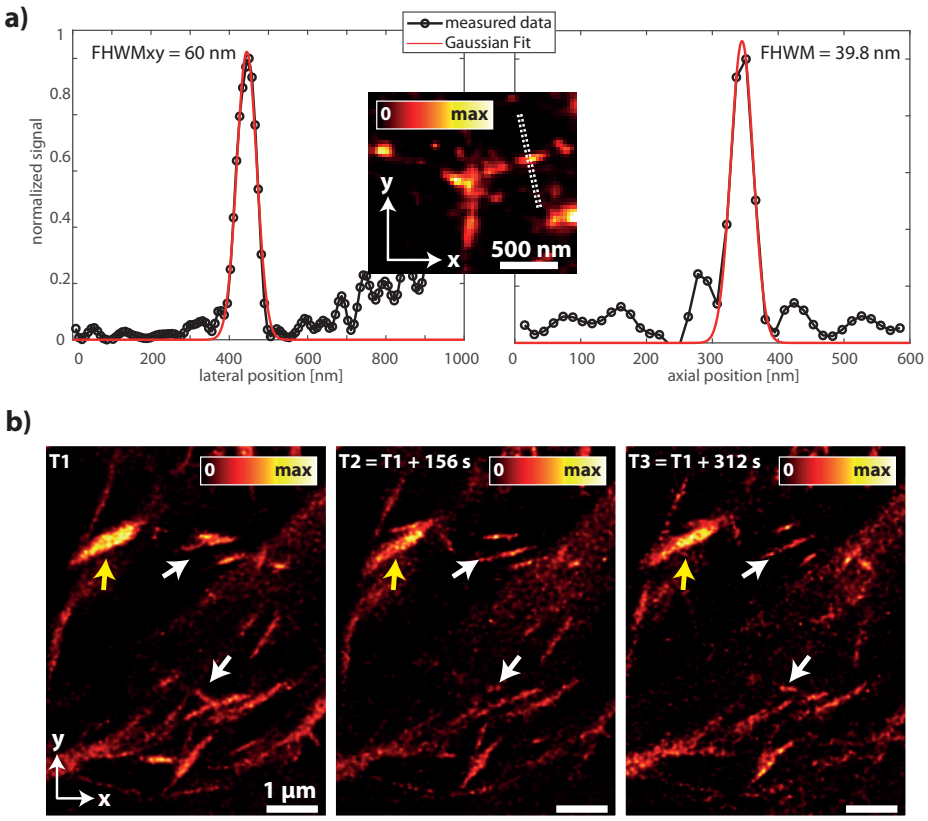

Figure 5.9.: IsoSTED measurement on the actin network of human stem cells grown on a PAA gel: **(a)** Smoothed x-y-section through the recording and the lateral and axial line profile through a thin filament. The orientation and averaging of the lateral profile is indicated by the dashed white box. Gaussian fits reveal a filament size of 60 nm and 39.8 nm in lateral and axial direction. **(b)** The same x-y-section at three different points in time reveals the reorganization of the actin network. Thin filaments indicated by white arrows reorganize faster than thicker filaments, indicated by yellow arrows.

zation changes. Figure 5.9**b** shows an x-y-section through the recording at three points in time, each separated 156 s from the other. The reorganization of the small filaments, indicated by the white arrows, is faster than reorganization of the large filament indicated by yellow arrows. This shows that the time between successive time series measurements can be adjusted depending on the structure of interest. Nonetheless, isoSTED microscopy of living cells on aquaeous gels can provide new insights on the three-dimensional distribution of intracellular structures.

6. Discussion and Outlook

In this thesis, for the first time, an isoSTED microscope for live cell imaging is introduced. In order to characterize the setup, the stability of the system consisting of both objective lenses and the sample stage is investigated in section 3.3. For measurements in which the z-axis is the slow axis, the stability of the objective lenses with respect to each other ($\sigma \leq 2.9$ nm) is the limiting factor for the achievable resolution. When fast axial scanning is performed, resonant vibrations occur and give rise to oscillations of the sample stage as well as the fixed objective lens in the lateral direction (see fig. 3.12 and fig. 3.13). Nonetheless, axial scanning with up to 70 Hz is possible without decreasing the resolution significantly. In order to achieve higher axial scanning frequencies, the mass of the sample stage could be reduced, which would increase the resonance frequency of the system. Measurements with a simplified and therefore lighter sample stage have shown that a reduction of the weight from 571 g to 268 g allows for axial scanning with up to 200 Hz. However, most of the data sets shown in this thesis are recorded with the z-axis as the slow axis.

The resolution of the isoSTED microscope utilizing oil-immersion objective lenses is determined under ideal measurement conditions on samples containing a layer of 25 nm-diameter crimson fluorescent beads and is better than 34 nm in all directions (see section 4.1.1). Furthermore, isoSTED measurements on fixed cells show that the microscope can easily operate within a volume of 30 µm x 40 µm x 2.5 µm (x, y, z) (see section 4.1.2). This is a fivefold increase as compared to state of the art isoSTED microscopy [15–18].

For live cell imaging, the oil-immersion objective lenses are replaced with water-immersion objective lenses. Due to the lower NA of the water-immersion objective lenses the size of the focal spots is increased and thus at the same STED laser power, the maximum STED intensity in the focus is decreased accordingly. Nonetheless, an isotropic resolution better than 56 nm is determined on recordings of 48 nm-diameter crimson fluorescent beads (see section 4.2.1) and on the vimentin network in fixed cells stained with antibodies (see section 4.2.2).

In the cell measurements (see fig. 4.6), it is apparent that extended regions within the sample, in which structures are arranged arbitrarily in three dimensions, pose a problem for isoSTED microscopy utilizing water-immersion objective lenses. Sig-

nals originating from structures above and below the focal plane are detected and deteriorate the image quality. These so called out-of-focus signals, or S_{OOFC}, are generated by low intensity out-of-focus contributions of the effective isoSTED PSF that lie within the detection volume (see section 4.2.3). Hence, a method to separately detect the S_{OOFC} and remove them from the recorded data sets is developed in section 4.2.3. This out-of-focus contribution removal method is based on detecting signals above and below the focal plane by laterally shifted offset detection channels. The lateral shift is chosen such that the overlap of the detection volumes of the offset detection channels and the main detection channel is substantial in the regions of the S_{OOFC} but neglible in the focal plane. Therefore, by scaling and subtracting the signals of the individual offset detection channels from the data recorded with the main detection channel, the image quality is substantially increased (see section 4.2.2 and section 5). Due to limitations of the data acquisition software used, only three offset detection channels can currently be implemented in addition to the main detection channel. However, we show that three offset detection channels are sufficient to reduce the S_{OOFC} in the corrected data set substantially. Nonetheless, increasing the amount of shifted detectors would also further increase the image quality, as each shifted detector rather measures the S_{OOFC} from the side it was shifted to (see fig. 4.14). Like in image scanning microscopy a pixelated area detector e.g. a camera chip could be used to measure the signals of the main and the offset detection channels simultaneously. In this case, however, it has to be ensured that the overlap of the detection volumes of the main and the offset detection channels are negligible in the focal plane.

A main advantage of the presented out-of-foucs contribution removal method is that neither a priori information about the sample nor the PSF of the imaging system is needed. In combination with other image reconstruction methods, e.g. deconvolution, it is a powerful tool to further increase the image quality, especially when only a small fraction of the sample is recorded. When the sample is not scanned by the entire PSF, standard deconvolution techniques fail since they are based on signal conservation and thus introduce artifacts in the deconvolved data set. New deconvolution methods that do not require signal conservation and therefore can handle signal contributions from structures outside the measured volume are currently being developed in the group of Thorsten Hohage at the Institute for Numerical and Applied Mathematics at the University of Göttingen as a cooperation within the SFB 755 - Nanoscale Photonic Imaging. Particularly, the signals detected by the offset detection channels can be utilized to decide which signal contributions should be kept and which could be discarded.

In order to determine the resolution of the isoSTED microscope in living cells, the microtubule network in HDFn cells is recorded and analyzed (see section 5.1). As

the outer diameter of the microtubules is known to be 25 nm [58], they are an ideal test structure and reveal that the resolution of the isoSTED microscope in living cells is comparable to the resolution measured on fluorescent beads (see fig. 5.3). The such determined resolution in the axial direction is sligthly better than in the lateral direction (see fig. 5.3). This could be due to a higher STED intensity in the axial direction, filament movements during the measurement, or could also originate from minor aberrations introduced by the refractive index difference between the measured cells and the embedding medium. Differences in the STED intensity in the lateral and axial direction can be excluded since measurements on fluorescent beads show an isotropic resolution (see fig. 4.5). In order to exclude filament movements as a reason for the better axial resolution, the data sets would have to be acquired faster, especially in the axial direction. This is not possible with the present setup and should therefore be checked once the improvements regarding an increase of the axial scanning speed have been implemented. In order to further minimize the occurrence of minor aberrations in future applications, the refractive index of the embedding and the immersion media could be slightly increased, which would allow to better reduce residual deviations [19, 79]. In the future, the use of adaptive optics should be considered as well, since this would allow to compensate aberrations caused by the sample and thus would improve the resolution and the detected signal [80–83]. This would also enable to apply isoSTED microscopy under physiological conditions in thick tissues.

IsoSTED microscopy utilizing water-immersion objective lenses is already a promising tool to better understand the 3D morphology of structures on the single cell level. Compared to the recently reported base acquisition time of 7 - 21 $s\mu m^{-3}$ [19], we achieved acquisition times of 0.8 - 1.7 $s\mu m^{-3}$ in the measurements on the microtubule network in living HDFn cells, which is an improvement by a factor of $\sim$ 9 - 13. Thus, isoSTED time lapse imaging gives insight into the reorganization of the microtubule (see section 5.2) and the actin network (see section 5.4).

Exemplary for the versatile usability of isoSTED microscopy for live cell imaging, the vimentin network in living U-2 OS cells is imaged and subsequently analyzed in section 5.3. For this purpose genetically modified cells that express SNAP-tagged vimentin are stained with a SiR-SNAP substrate and imaged (see section 5.3). Moreover, to show the suitability to image samples under more physiological conditions isoSTED imaging of samples on collagen-coated PAA layers is performed (see section 5.4). Such PAA layers are e.g. used to mimic the elasticity of different extracellular matrices in order to investigate the differentiation of stem cells in different environments. Analyzing isoSTED recordings of 48 nm-diameter beads on such gels reveals that under such imaging conditions the isotropic resolution is better than 63 nm (see section 5.4) and therefore only slightly lower than the resolution measured on

beads on cover glasses. In addition, the actin network in human stem cells seeded on collagen-coated PAA gels was measured. The organization and size of the actin filaments in a cell varies from thin mesh-like structures to thick stressfiber bundles and depends on its position and role within the cell. The lateral size of a thin actin filament was determined to be 60 nm (see figure 5.9) and is thus in the order of the resolution.

Even though isoSTED time lapse imaging is demonstrated in this thesis, photobleaching is still a problem, especially when the amount of time lapse steps is increased or the recorded volume is decreased. Therefore, additionally to the laser system with a lower repetition rate of 30 MHz, AOMs are implemented into all laser beam paths in the setup (see section 3.2). They are used to control the laser power entering the setup and allow on- and off-switching on a sub-pixel timescale and can therefore be used to control the light dose impinging on the sample. This enables sample preservation techniques such as RESCue-STED [50] or DyMin [84]. The latter is able to reduce the STED light dose by a factor of 20 under common biological conditions [84]. In RESCue-STED e.g. the sample is illuminated by the excitation and STED beams and in each pixel it is checked whether signal is emitted or not. If no signal is emitted or if a sufficient signal is detected within a fraction of the pixel dwell time, the lasers are switched off for this pixel in order to preserve the sample from photobleaching. Conventional implementations of RESCue-STED are not applicable to isoSTED microscopy utilizing water-immersion objective lenses, since the algorithm cannot distinguish between signal from the focal plane and S_{OOFC}. In a next step, the signal detected by the offset detection channels should be used additionally to the main channel to decide whether the lasers should be switched off or not. The RESCue principle could thus be applied to isoSTED microscopy utilizing water-immersion objective lenses which would allow to decrease the recorded volume or increase the number of time lapse steps. Furthermore, it might be possible to implement an algorithm that uses the measured S_{OOFC} in order to perform real time out-of-focus contribution removal, which would yield high quality images without post-processing.

Another future application could be the combination of fluorescence correlation spectroscopy (**FCS**) [85] and isoSTED microscopy. In FCS the fluctuation of the fluorescence emission from a distinct measurement volume is detected in order to extract information about molecular associations and reactions within this volume. The calculated correlation curves encode the average molecular transit time through the probed volume and the average number of fluorescing molecules. By combining STED microscopy and FSC the probed volume can be decreased which allows measurements at the single molecule level [86]. Standard STED-FCS microscopy is already used to investigate molecular dynamics at this level at the plasma membrane

of living cells [86–88]. However, by decreasing the probed volume a concomitant relative increase of unspecific background signal precludes accurate single-molecule measurement [86]. This unspecific background signal is exactly the S_{OOFC}. Hence, implementing the here presented method to measure and remove the S_{OOFC} into a standard STED-FCS microscope can be used to clean up the recorded signal and will enable STED-FCS microscopy within three-dimensional samples. Perspectively, in combination with FCS the here presented isoSTED microscope could be used to probe isotropic volumes in living cells in order to better understand biological processes.

Bibliography

[1] F. Stelluti and F. Cesi. *Apiarium*. 1625.

[2] R. Hooke. *Micrographia*. The Royal Society, 1665.

[3] E. Abbe. Beiträge zur Theorie des Mikroskops und der mikroskopischen Wahrnehmung. *Archiv für mikroskopische Anatomie*, 9:413–468, 1873.

[4] Lord Rayleigh. On the theory of optical images, with special reference to the microscope. *Philosophical Magazine Series 5*, 42(255):167–195, 1896.

[5] A. Egner, M. Schrader, and S. W. Hell. Refractive index mismatch induced intensity and phase variations in fluorescence confocal, multiphoton and 4pi-microscopy. *Optics Communications*, 153(4-6):211–217, 1998.

[6] A. Egner and S. W. Hell. Equivalence of the huygens-fresnel and debye approach for the calculation of high aperture point-spread functions in the presence of refractive index mismatch. *Journal of Microscopy*, 193(3):244–249, 1999.

[7] S. W. Hell and J. Wichmann. Breaking the diffraction resolution limit by stimulated emission: stimulated-emission-depletion fluorescence microscopy. *Optics Letters*, 19(11):780–782, 1994.

[8] T. A. Klar and S. W. Hell. Subdiffraction resolution in far-field fluorescence microscopy. *Optics Letters*, 24(14):954–956, 1999.

[9] M. Hofmann, C. Eggeling, S. Jakobs, and S. W. Hell. Breaking the diffraction barrier in fluorescence microscopy at low light intensities by using reversibly photoswitchable proteins. *Proceedings of the National Academy of Sciences*, 102(49):17565–17569, 2005.

[10] C. Eggeling, M. Hilbert, H. Bock, C. Ringemann, M. Hofmann, A. C. Stiel, M. Andresen, S. Jakobs, A. Egner, A. Schönle, and S. W. Hell. Reversible photoswitching enables single-molecule fluorescence fluctuation spectroscopy at high molecular concentration. *Microscoscopy Research and Technique*, 70(12):1003–1009, 2007.

[11] T. A. Klar, S. Jakobs, M. Dyba, A. Egner, and S. W. Hell. Fluorescence microscopy with diffraction resolution barrier broken by stimulated emission. *Proceedings of the National Academy of Sciences of the United States of America*, 97(15):8206–8210, 2000.

[12] B. Harke, J. Keller, C. K. Ullal, V. Westphal, A. Schönle, and S. W. Hell. Resolution scaling in STED microscopy. *Optics Express*, 16(6):4154–4162, 2008.

[13] S. W. Hell and E. H. K. Stelzer. Fundamental improvement of resolution with a 4Pi-confocal fluorescence microscope using two-photon excitation. *Optics Communications*, 93(5, 6):277 – 282, 1992.

[14] S. W. Hell and E. H. K. Stelzer. Properties of a 4Pi confocal fluorescence microscope. *Journal of the Optical Society of America A*, 9(12):2159, 1992.

[15] R. Schmidt, C. A. Wurm, S. Jakobs, J. Engelhardt, A. Egner, and S. W. Hell. Spherical nanosized focal spot unravels the interior of cells. *Nature Methods*, 5(6):539–544, 2008.

[16] R. Schmidt, C. A. Wurm, A. Punge, A. Egner, S. Jakobs, and S. W. Hell. Mitochondrial cristae revealed with focused light. *Nano Letters*, 9(6):2508–2510, 2009.

[17] C. K. Ullal, R. Schmidt, S. W. Hell, and A. Egner. Block copolymer nanostructures mapped by far-field optics. *Nano Letters*, 9(6):2497–2500, 2009.

[18] C. K. Ullal, S. Primpke, R. Schmidt, U. Böhm, A. Egner, P. Vana, and S. W. Hell. Flexible microdomain specific staining of block copolymers for 3D optical nanoscopy. *Macromolecules*, 44:7508–7510, 2011.

[19] U. Boehm, S. W. Hell, and R. Schmidt. 4Pi-RESOLFT nanoscopy. *Nature Communications*, 7:10504, 2016.

[20] M. Born and E. Wolf. *Principles of Optics*. Cambridge University Press, 7th edition, 1999.

[21] J.W. Goodman. *Introduction to Fourier Optics*. McGraw-Hill Science, 2nd edition, 1996.

[22] M. Minsky. Microscopy apparatus. US Patent No. 3,013,467, 1961.

[23] S. W. Hell. Far-field optical nanoscopy. *Science*, 316(5828):1153–1158, 2007.

[24] P. Török, P. Varga, Z. Laczik, and G. R. Booker. Electromagnetic diffraction of light focused through a planar interface between materials of mismatched refractive indices: an integral representation. *Journal of the Optical Society of America*, 12(2):325, 1995.

[25] P. E. Hänninen, S. W. Hell, J. Salo, E. Soini, and C. Cremer. Two-photon excitation 4Pi confocal microscope: Enhanced axial resolution microscope for biological research. *Applied Physics Letters*, 66(13):1698–1700, 1995.

[26] W. H. Richardson. Bayesian-based iterative method of image restoration. *Journal of the Optical Society of America*, 62(1):55, 1972.

[27] G. M. P. van Kempen, L.J. van Vliet, P.J Verveer, and H. T. M. van der Voort. A quantitative comparison of image restoration methods for confocal microscopy. *Journal of Microscopy*, 185(3):354–365, 1997.

[28] Lukas Novotny and Bert Hecht. *Principles of Nano-Optics*. Cambridge University Press, 2 edition, 2012.

[29] G. Donnert, J. Keller, R. Medda, M. A. Andrei, S. O. Rizzoli, R. Lührmann, R. Jahn, C. Eggeling, and S. W. Hell. Macromolecular-scale resolution in biological fluorescence microscopy. *Proc Natl Acad Sci U S A*, 103(31):11440–11445, 2006.

[30] M. J. Rust, M. Bates, and X. Zhuang. Sub-diffraction-limit imaging by stochastic optical reconstruction microscopy (storm). *Nature Methods*, 3(10):793–796, 2006.

[31] S. van de Linde, A. Löschberger, Klein T., Heidbreder M., Wolter S., Heilemann M., and Sauer M. Direct stochastic optical reconstruction microscopy with standard fluorescent probes. *Nature Protocols*, 6(7):991–1009, 2011.

[32] E. Betzig, G. H. Patterson, R. Sougrat, O. W. Lindwasser, S. Olenych, J. S. Bonifacino, M. W. Davidson, J. Lippincott-Schwartz, and H. F. Hess. Imaging intracellular fluorescent proteins at nanometer resolution. *Science*, 313(5793):1642–1645, 2006.

[33] S. T. Hess, T. P. K. Girirajan, and M. D. Mason. Ultra-high resolution imaging by fluorescence photoactivation localization microscopy. *Biophysical Journal*, 91(11):4258–4272, 2006.

[34] C. Geisler, A. Schönle, C. von Middendorff, H. Bock, C. Eggeling, A. Egner, and S. W. Hell. Resolution of $\lambda/10$ in fluorescence microscopy using fast single molecule photo-switching. *Applied Physics A*, 88(2):223–226, 2007.

[35] J. Foelling, M. Bossi, H. Bock, R. Medda, Ch. A. Wurm, B. Hein, S. Jakobs, Ch. Eggeling, and S. W. Hell. Fluorescence nanoscopy by ground-state depletion and single-molecule return. *Nat. Methods*, 5(11):943–945, 2008.

[36] S. W. Hell. Microscopy and its focal switch. *Nature Methods*, 6(1):24–32, 2009.

[37] S. W. Hell and M. Kroug. Ground-state-depletion fluorscence microscopy: A concept for breaking the diffraction resolution limit. *Applied Physics B*, 60(5):495–497, 1995.

[38] M. Dyba, J. Keller, and S. W. Hell. Phase filter enhanced STED-4Pi fluorescence microscopy: Theory and experiment. *New Journal of Physics*, 7:134, 2005.

[39] V. Westphal and S. W. Hell. Nanoscale resolution in the focal plane of an optical microscope. *Physical Review Letters*, 94(14):143903, 2005.

[40] S. W. Hell. Toward fluorescence nanoscopy. *Nature Biotechnology*, 21(11):1347–1355, 2003.

[41] E. Rittweger, K. Y. Han, S. E. Irvine, C. Eggeling, and S.W. Hell. STED microscopy reveals crystal colour centres with nanometric resolution. *Nature Photonics*, 3(3):144–147, 2009.

[42] D. Wildanger, B. R. Patton, H. Schill, L. Marseglia, J. P. Hadden, S. Knauer, A. Schönle, J. G. Rarity, J. L. O'Brien, S. W. Hell, and J. M. Smith. Solid immersion facilitates fluorescence microscopy with nanometer resolution and sub-angström emitter localization. *Advanced Optical Materials*, 2012.

[43] M. Dyba and S. W. Hell. Focal spots of size lambda/23open up far-field florescence microscopy at 33 nm axial resolution. *Physical Review Letters*, 88(16), 2002.

[44] M. Dyba, S. Jakobs, and S. W. Hell. Immunofluorescence stimulated emission depletion microscopy. *Nature Biotechnology*, 21(11):1303–1304, 2003.

[45] A. Egner, S. Jakobs, and S. W. Hell. Fast 100-nm resolution three-dimensional microscope reveals structural plasticity of mitochondria in live yeast. *Proceedings of the National Academy of Sciences of the United States of America*, 99(6):3370–3375, 2002.

[46] Roman Schmidt. 3D fluorescence microscopy with isotropic resolution on the nanoscale, 2008.

[47] A. Egner and S.W. Hell. Aberrations in confocal and multi-photon fluorescence microscopy induced by refractive index mismatch. In James B. Pawley, editor, *Handbook of Biological Confocal Microscopy*, chapter 20, pages 404–413. SpringerScience+Business Media, 3 edition, 2006.

[48] C. Eggeling, J. Widengren, R. Rigler, and C. A. M. Seidel. Photobleaching of fluorescent dyes under conditions used for single-molecule detection: evidence of two-step photolysis. *Analytical Chemistry*, 70(13):2651–2659, 1998.

[49] A. Hopt and E. Neher. Highly nonlinear photodamage in two-photon fluorescence microscopy. *Biophysical Journal*, 80(4):2029–2036, 2001.

[50] T. Staudt, A. Engler, E. Rittweger, N. Harke, J. Engelhardt, and S.W. Hell. Far-field optical nanoscopy with reduced number of state transition cycles. *Optics Express*, 19(6):5644, 2011.

[51] A. Egner, C. Geisler, C. von Middendorff, H. Bock, D. Wenzel, R. Medda, M. Andresen, A. C. Stiel, S. Jakobs, C. Eggeling, A. Schönle, and S. W. Hell. Fluorescence nanoscopy in whole cells by asynchronous localization of photoswitching emitters. *Biophys. J.*, 93(9):3285–3290, 2007.

[52] T. Staudt, M. C. Lang, R. Medda, J. Engelhardt, and S. W. Hell. 2,2'-thiodiethanol: A new water soluble mounting medium for high resolution optical microscopy. *Microscopy Research and Technique*, 70(1):1–9, 2006.

[53] A. J. Engler, S. Sen, H. L. Sweeney, and D. E. Discher. Matrix elasticity directs stem cell lineage specification. *Cell*, 126(4):677–689, 2006.

[54] A. Zemel, F. Rehfeldt, A. E. X. Brown, D. E. Discher, and S. A. Safran. Optimal matrix rigidity for stress-fibre polarization in stem cells. *Nature Physics*, 6(6):468–473, 2010.

[55] M. Bernhardt, M. Priebe, M. Osterhoff, C. Wollnik, A. Diaz, T. Salditt, and F. Rehfeldt. X-ray micro- and nanodiffraction imaging on human mesenchymal stem cells and differentiated cells. *Biophysical Journal*, 110(3):680–690, 2016.

[56] B. Eltzner, C. Wollnik, C. Gottschlich, S. Huckemann, and F. Rehfeldt. The filament sensor for near real-time detection of cytoskeletal fiber structures. *PLOS ONE*, 10(5):e0126346, 2015.

[57] C. A. Wurm, D. Neumann, R. Schmidt, A. Egner, and S. Jakobs. Sample preparation for STED Microscopy. *Methods in Molecular Biology*, 591:185–199, 2010.

[58] K. Weber, P. C. Rathke, and M. Osborn. Cytoplasmic microtubular images in glutaraldehyde-fixed tissue culture cells by electron microscopy and by immunofluorescence microscopy. *Proceedings of the National Academy of Sciences*, 75(4):1820–1824, 1978.

[59] D. Aquino, A. Schönle, C. Geisler, C. von Middendorf, C. A. Wurm, Y. Okamura, T. Lang, S. W. Hell, and A. Egner. Two-color nanoscopy of three-dimensional volumes by 4Pi detection of stochastically switched fluorophores. *Nature Methods*, 8:353–359, 2011.

[60] U. Schnell, F. Dijk, K. A. Sjollema, and B. N. G. Giepmans. Immunolabeling artifacts and the need for live-cell imaging. *Nature Methods*, 9(2):152–158, 2012.

[61] R. Arimoto and J.M. Murray. A common aberration with water-immersion objective lenses. *Journal of Microscopy*, 216(1):49–51, 2004.

[62] M. Schürmann, J. Scholze, P. Müller, J. Guck, and C. J. Chan. Cell nuclei have lower refractive index and mass density than cytoplasm. *Journal of Biophotonics*, 9(10):1068–1076, 2016.

[63] S. J. Sahl, S. W. Hell, and S. Jakobs. Fluorescence nanoscopy in cell biology. *Nature Reviews Molecular Cell Biology*, 18(11):685–701, 2017.

[64] H. Herrmann, M. Häner, M. Brettel, S. A. Müller, K. N. Goldie, B. Fedtke, A. Lustig, W. W. Franke, and U. Aebi. Structure and assembly properties of the intermediate filament protein vimentin: The role of its head, rod and tail domains. *Journal of Molecular Biology*, 264(5):933–953, 1996.

[65] N. Costigliola, L Ding, C. J. Burckhardt, S. J. Han, E. Gutierrez, A. Mota, A. Groisman, T. J. Mitchison, and G. Danuser. Vimentin fibers orient traction stress. *Proceedings of the National Academy of Sciences*, 114(20):5195–5200, 2017.

[66] G. Moneron, R. Medda, B. Hein, A. Giske, V. Westphal, and S.W. Hell. Fast sted microscopy with continuous wave fiber lasers. *Optics Express*, 18(2):1302, 2010.

[67] L. Lukinavičius, L. Reymond, K. Umezawa, O. Sallin, E. D'Este, F. Göttfert, H. Ta, S.W. Hell, Y. Urano, and K. Johnsson. Fluorogenic probes for multicolor imaging in living cells. *Journal of the American Chemical Society*, 138(30):9365–9368, 2016.

[68] G. Lukinavicius, K. Umezawa, N. Olivier, A. Honigmann, G. Yang, T. Plass, V. Mueller, L. Reymond, I. R. Correa, Z. G. Luo, C. Schultz, E. A. Lemke,

P. Heppenstall, C. Eggeling, S. Manley, and K. Johnsson. A near-infrared fluorophore for live-cell super-resolution microscopy of cellular proteins. *Nature Chemistry*, 5(2):132–139, 2013.

[69] L. Gražvydas, L. Reymond, E. D'Este, A. Masharina, F. Göttfert, H. Ta, A. Güther, M. Fournier, S. Rizzo, H. Waldmann, C. Blaukopf, C. Sommer, D. W. Gerlich, H.-D. Arndt, S. W. Hell, and K. Johnsson. Fluorogenic probes for live-cell imaging of the cytoskeleton. *Nature Methods*, 11(7):731–733, 2014.

[70] L. Gražvydas, C. Blaukopf, E. Pershagen, A. Schena, L. Reymond, E. Derivery, M. Gonzalez-Gaitan, E. D'Este, S. W. Hell, D. W. Gerlich, and K. Johnsson. SiR–hoechst is a far-red DNA stain for live-cell nanoscopy. *Nature Communications*, 6:8497, oct 2015.

[71] K. S. Morozova, K. D. Piatkevich, T. J. Gould, J. Zhang, J. Bewersdorf, and V. V. Verkhusha. Far-red fluorescent protein excitable with red lasers for flow cytometry and superresolution STED nanoscopy. *Biophysical Journal*, 99(2):L13–15, 2010.

[72] F. Bottanelli, E. B. Kromann, E. S. Allgeyer, R. S. Erdmann, S. Wood Baguley, G. Sirinakis, A. Schepartz, D. Baddeley, D. K. Toomre, J. E. Rothman, and J. Bewersdorf. Two-colour live-cell nanoscale imaging of intracellular targets. *Nature Communications*, 7(1), 2016.

[73] F. R. Winter, M. Loidolt, V. Westphal, A. N. Butkevich, C. Gregor, S. J. Sahl, and S. W. Hell. Multicolour nanoscopy of fixed and living cells with a single STED beam and hyperspectral detection. *Scientific Reports*, 7(1), 2017.

[74] A. N. Butkevich, H. Ta, M. Ratz, S. Stoldt, S. Jakobs, V. N. Belov, and S.W. Hell. Two-color 810 nm STED nanoscopy of living cells with endogenous SNAP-tagged fusion proteins. *ACS Chemical Biology*, 13(2):475–480, 2017.

[75] Ralph Weissleder. A clearer vision for in vivo imaging. *Nature Biotechnology*, 19(4):316–317, 2001.

[76] S. Wäldchen, J. Lehmann, T. Klein, S. van de Linde, and M. Sauer. Light-induced cell damage in live-cell super-resolution microscopy. *Scientific Reports*, 5(1), 2015.

[77] A. Desai and T. J. Mitchison. MICROTUBULE POLYMERIZATION DYNAMICS. *Annual Review of Cell and Developmental Biology*, 13(1):83–117, 1997.

[78] L. Blanchoin, R. Boujemaa-Paterski, C. Sykes, and J. Plastino. Actin dynamics, architecture, and mechanics in cell motility. *Physiological Reviews*, 94(1):235–263, 2014.

[79] D.-S. Wan, M. Rajadhyaksha, and R. H. Webb. Analysis of spherical aberration of a water immersion objective: application to specimens with refractive indices 1.33-1.40. *Journal of Microscopy*, 197(3):274–284, 2000.

[80] M. J. Booth, M. A. A. Neil, R. Juskaitis, and T. Wilson. Adaptive aberration correction in a confocal microscope. *Proceedings of the National Academy of Sciences of the United States of America*, 99(9):5788–5792, 2002.

[81] T. J. Gould, D. Burke, J. Bewersdorf, and M. J. Booth. Adaptive optics enables 3D STED microscopy in aberrating specimens. *Optics Express*, 20(19):20998, 2012.

[82] T. J. Gould, E. B. Kromann, D. Burke, M. J. Booth, and J. Bewersdorf. Auto-aligning stimulated emission depletion microscope using adaptive optics. *Optics Letters*, 38(11):1860, 2013.

[83] M. J Booth. Adaptive optical microscopy: the ongoing quest for a perfect image. *Light: Science & Applications*, 3(4):e165, 2014.

[84] J. Heine, M. Reuss, B. Harke, E. D'Este, S. J. Sahl, and S. W. Hell. Adaptive-illumination STED nanoscopy. *Proceedings of the National Academy of Sciences*, 114(37):9797–9802, 2017.

[85] E. L. Elson and D. Magde. Fluorescence correlation spectroscopy. i. conceptual basis and theory. *Biopolymers*, 13(1):1–27, 1974.

[86] C. Ringemann, C. Harke, C. von Middendorff, R. Medda, A. Honigmann, R. Wagner, M. Leutenegger, A. Schönle, S. W. Hell, and C. Eggeling. Exploring single-molecule dynamics with fluorescence nanoscopy. *New Journal of Physics*, 11(10):103054, 2009.

[87] C. Eggeling, C. Ringemann, R. Medda, G. Schwarzmann, K. Sandhoff, S. Polyakova, V. N. Belov, B. Hein, C. von Middendorff, A. Schonle, and S. W. Hell. Direct observation of the nanoscale dynamics of membrane lipids in a living cell. *Nature*, 457(7233):1159–1162, 2009.

[88] A. Honigmann, V. Mueller, H. Ta, A. Schönle, E. Sezgin, S. W. Hell, and C. Eggeling. Scanning STED-FCS reveals spatiotemporal heterogeneity of lipid interaction in the plasma membrane of living cells. *Nature Communications*, 5(1), 2014.

A. Protocols for sample preparation

Reagents

- Phosphate buffered saline (**PBS**, *P5493, Merck, Darmstadt, Germany*) diluted to 1x concentration in ultra pure water
- Blocking solution (**BS**): 2 % bovine serum albumin fraction V (**BSA**, *BSAV-RO, Merck, Darmstadt, Germany*) in PBS
- **PFA solution**: paraformaldehyde (*E15714, Science Services GmbH, München, Germany*) diluted to a concentration of 3.7 % in PBS
- **Cell culture medium**: 10 % fetal bovine serum (**FBS**, *S 0615, Biochrom, Berlin, Germany*), 1 % penicillin/streptomycin (*A 2212, Merck, Darmstadt, Germany*) and 1 % sodium pyruvate solution (*S8636, Merck, Darmstadt Germany*) in Dulbecco's modified eagle medium (**DMEM**, *61965059, Thermo Fisher Scientific, Waltham, MA, USA*)

Fluorescent beads

The stock solution of the fluorescent beads is diluted in ultra pure water. The dilution for the 25 nm-diameter beads (*F8782, Thermo Fisher Scientific, Waltham, MA, USA*) is 1:20.000, for the 48 nm-diameter beads (*customized, Thermo Fisher Scientific, Waltham, MA, USA*) 1:5.000 and for the 200 nm-diameter beads (*F8806, Thermo Fisher Scientific, Waltham, MA, USA*) 1:1.000. A drop of 100 µl Poly-L-lysine solution (*P8920, Merck, Darmstadt, Germany*) is placed on a cover glass and incubated for five minutes. Meanwhile the diluted beads are sonicated in an ultrasonic bath for five minutes. Afterwards, the Poly-L-lysine solution is removed from the cover glass and 100 µl of the sonicated bead solution is placed on the cover glass for 15 s. Subsequently the bead solution is removed, the embedding medium is added and a second cover glass is placed on top of the sample. Thereafter the sample is sealed using either nail polish or a two component silicon glue (*picodent twinsil® 22, Picodent, Wipperfürth, Germany*).

Fixed cell samples

Cells are seeded on clean cover glasses and incubated in cell culture medium at 37 °C and 5 % CO_2 until the desired confluency is reached.

Fixation

Methanol fixation The cover glasses are washed once with pre-warmed PBS and afterwards incubated in -20 °C cold Methanol for five minutes. Afterwards the Methanol is removed and the cells are washed in PBS.

PFA fixation The cover glasses are washed once with pre-warmed PBS and afterwards incubated in the PFA solution for ten minutes at room temperature. Afterwards the PFA solution is removed and the cells are washed in PBS.

Antibody staining

The cover glasses with fixed cells are washed in BS three times for five minutes. Afterwards the blocking solution is replaced by the primary antibody staining solution (primary antibody diluted in BS) and incubated for one hour at room temperature. Subsequently the cover glasses are washed in BS three times for five minutes and incubated in the secondary antibody staining solution (secondary antibody diluted in BS) for one hour at room temperature. Note, that the cover glasses should be shield from light when the secondary antibody is incubated. Thereafter, the cover glasses are washed three times in PBS for five minutes each time, the PBS is removed and the embedding medium is added. Then a second cover glass is placed on top of the sample and sealed either using nail polish or two component silicon glue (*picodent twinsil® 22, Picodent, Wipperfürth, Germany*).

List of publications

Parts of this thesis have been published as follows:

- R. Siegmund, C. Geisler, A. Egner: "isoSTED microscopy of living cells", submitted

Talks on conferences:

- *Focus on Microscopy*, Göttingen, Germany (2015)
- *SPIE Optics + Photonics*, San Diego, USA (2015)
- *International Symposium Biological Dynamics from Microscopic to Mesoscopic Scales*, Grimma, Germany (2016)

Acknowledgments

The work presented in this thesis would not have been possible without the guidance and help of several individuals who in one way or the other contributed in the preparation and completion of this study. I take this opportunity to express my sincere gratitude to all those who made this PhD thesis possible.

First and foremost, I would like to thank my supervisor **Prof. Dr. Alexander Egner** for his dedicated help, advice, inspiration, encouragement and continuous support throughout my PhD thesis. The discussions on physical problems were always enlightening. Thank you for the opportunity to pursue all ideas in a perfectly equipped laboratory. I would furthermore like to acknowledge for the opportunity to participate in conferences and international meetings to broaden my horizons. Thank you for your commitment in proofreading my thesis.

Many thanks to **Prof. Dr. Tim Salditt**, who is not only my second supervisor, but also maintained and thrived my interest in science and research by encouraging me during numerous meetings in the collaborative research center.

I would like to thank **Prof. Dr. Sarah Köster**, **Prof. Dr. Stefan Jakobs**, **Prof. Dr. Thorsten Hohage** and **Dr. Florian Rehfeldt** for being part of my thesis committee and for many enlightening discussions within various cooperations, either on cell culture and cell staining, on the interpretation of data or on mathematical problems.

Many thanks to **Dr. Claudia Geisler**, who was always ready to discuss interesting and horizon-opening topics in work-related as well as in private fields. Thank you for your constant interest and passion for science and group-related aspects.

I would furthermore like to thank **Dr. Frank Werner** without whom the solution of the mathematical problem of the out-of-focus correction method would have been considerably more difficult. Thank you for always being quick in response, interested and very motivated.

Many thanks to **Christian Wurm**, **Tanja Gilat**, **Ellen Rothermel** for many helpful hints, discussions and instructions without which my attempts to keep the cell cultures alive would have probably been in vain.

I would like to thank all my colleagues from the LLG for the warm-hearted welcome and for always being ready for discussions. A special appreciation goes to the administration and the purchasing department, who ensured that the daily laboratory business could be maintained without any problems.

A particular thank you goes to all current and former employees of the Optical Nanoscopy group. Thank you for many relaxing, energizing and refreshing

"tea" breaks.

Oskar, thank you for the great time. It was a pleasure to share an office with you. Due to your friendly and open personality, it was a great pleasure to work with you. It is an honor to know you and your small family.

Jennifer, thank you for great and music filled hours, not only in lab, but also in leisure time. It was and is always a pleasure to have you and your husband and now of course your "little one" around.

Francesco, the "biologist", thank you for many discussions, whether regarding work or private topics. Thank you for proofreading parts of this thesis and for the fact that I can always ask you for advice.

Britta, thank you for always being an open minded and pure hearted friend. Thanks a lot for all the numerous discussions not only on what I call "mathematics". Thank you for your patience and advice.

Many thanks to **Britta**, **Francesco** and **Julia** for many joint ventures in which I have learned to appreciate and love you not only as colleagues but also as friends. I'm looking forward to escape a deserted island, save polar bears and to hike adventure paths with you.

My deep and sincere gratitude goes to my family and friends for their continuous and unparalleled love, help and support. Thanks for always encouraging me to explore new directions in life, seek my own destiny and for your faith in me, even if you were not always aware or familiar with what I was doing.

My final sincere appreciation goes to you, **Anja**. Thank you for all the wonderful moments, for always being there for me and for all the comfort and safety you offer me.

Eidesstattliche Erklärung

Hiermit erkläre ich, dass ich die vorliegende Arbeit selbständig angefertigt, nicht anderweitig zu Prüfungszwecken vorgelegt und keine anderen als die angegebenen Hilfsmittel verwendet habe. Sämtliche wissentlich verwendeten Textausschnitte, Zitate oder Inhalte anderer Verfasser wurden ausdrücklich als solche gekennzeichnet.

Ort, Datum

René Siegmund